

# **Linear Synchronous Motor Based Propulsion for the Futuristic Hyperloop Transportation System**

by

Mohammad Abdul Bhuiya

A thesis submitted to the  
School of Graduate and Postdoctoral Studies in partial  
fulfillment of the requirements for the degree of

**Master of Applied Science**

Department of Electrical and Computer Engineering  
University of Ontario Institute of Technology (Ontario Tech University)

Oshawa, Ontario, Canada

February 2022

© Mohammad Abdul Bhuiya, 2022

## **Thesis Examination Information**

Submitted by: **Mohammad Abdul Bhuiya**

### **Master of Applied Science in Electrical and Computer Engineering**

Thesis title: Linear Synchronous Motor Based Propulsion for the Futuristic Hyperloop Transportation System

An oral defense of this thesis took place on February 27, 2022, in front of the following examining committee:

#### **Examining Committee:**

Chair of Examining Committee	Dr. Khalid Elgazzar
Research Supervisor	Dr. Mohamed Youssef
Examining Committee Member	Dr. Walid Morsi Ibrahim
Thesis Examiner	Dr. Yuping He

The above committee determined that the thesis is acceptable in form and content and that a satisfactory knowledge of the field covered by the thesis was demonstrated by the candidate during an oral examination. A signed copy of the Certificate of Approval is available from the School of Graduate and Postdoctoral Studies.

## **Abstract**

Current trends are leading towards an electrified future of transportation. Its popularity amongst the public is continuously increasing this trend. Today, the demands for an economical, carbon conscience and faster mode of transportation is imperative. Thus, the proposal for a new mode of transportation known as the Hyperloop has been popularized. Although, there are only some reports regarding its design. More specifically, reports regarding the propulsion system design methodology for the Hyperloop is lackluster. This thesis provides an initial steppingstone to a modeling and simulation study for the propulsion system in a Hyperloop. PSIM is used to develop the model and design the full power system and controller. To verify and validate the design, hardware in the loop technology is used. The controller implemented is tested through a Texas Instrument digital signal processor. The Typhoon real time verification shows matching results with the PSIM offline simulation model.

**Keywords:** Hyperloop; three – phase inverter; field - oriented control; propulsion system; linear synchronous motor; electrification; power electronics

## **Author's Declaration**

I hereby declare that this thesis consists of original work of which I have authored. This is a true copy of the thesis, including any required final revisions, as accepted by my examiners.

I authorize the University of Ontario Institute of Technology (Ontario Tech University) to lend this thesis to other institutions or individuals for the purpose of scholarly research. I further authorize University of Ontario Institute of Technology (Ontario Tech University) to reproduce this thesis by photocopying or by other means, in total or in part, at the request of other institutions or individuals for the purpose of scholarly research. I understand that my thesis will be made electronically available to the public.

Mohammad Abdul Bhuiya

---

## Statement of Contributions

The main contribution of this thesis is to study the novel concept of the Hyperloop system and its propulsion challenges. This includes studying the advantages and disadvantages of different power and control topologies. The thesis addresses various challenges of the sophisticated Hyperloop system. The propulsion system presented is based on electric vehicle and maglev traction systems. The contribution of the design pertains to the first-time integration of multiple components regarding the Hyperloop propulsion. Additionally, there is a research gap for the Hyperloop technology. Thus, the thesis provides an overview of the modeling and design of the propulsion system in the various top of the line software's (PSIM, Simulink & Typhoon HIL) for the first time.

- A portion of the study presented in chapter 3 & 4 has been published in the IEEE peer-reviewed journal , which can be found in [1].
- Some portions of the design of the inverter and DC-DC controller in chapter 4 was presented in [2], [3].
- Various portion of the design and methodology in chapter 4 and 5 are presented in [4].
- The design methodology in Chapter 5 has been published in IEEE Open Journal of Vehicular Technology [5].
- The overall content provided in this thesis has been published in an invited journal [6].

## **Acknowledgements**

Firstly, I would like to thank my supervisor, Dr. Mohamed Youssef. Through his continuous support, inspiration and guidance has led me to the completion of this thesis. I am truly grateful for everything Dr. Youssef has provided for me over the years throughout my undergraduate and graduate studies.

Secondly, I want to express my gratitude to the University of Ontario Institute of Technology for their financial support and the opportunity to pursue my passion and further progress towards my academic and career goals. I would also like to thank all the donors who have supported me financially through the Ontario Graduate Scholarship and Power Worker Union awards.

Finally, I would like to thank my parents, friends and family for their patience and motivation. Thank you mom and dad, I am truly grateful for the everlasting love and support to pursue my biggest dreams.

## Table of Contents

<b>Thesis Examination Information</b> .....	I
<b>Abstract</b> .....	II
<b>Author’s Declaration</b> .....	III
<b>Statement of Contributions</b> .....	IV
<b>Acknowledgements</b> .....	V
<b>Table of Contents</b> .....	VI
<b>List of Tables</b> .....	VIII
<b>List of Figures</b> .....	IX
<b>Nomenclature</b> .....	XI
<b>Chapter 1. Introduction</b> .....	12
<b>1.1 Background</b> .....	12
<b>1.2 Historical Development of Highspeed Railway Transportation and Maglev Systems</b> .....	13
<b>1.3 Problem Statement and Motivation</b> .....	16
<b>1.3 Scope and Objective of the Thesis</b> .....	16
<b>1.4 Thesis Organization</b> .....	17
<b>Chapter 2. Literature Review</b> .....	19
<b>2.1 Linear Synchronous Machines</b> .....	21
<b>2.2 Three Phase Inverter Design</b> .....	26
<b>2.3 Field Oriented Control</b> .....	30
<b>2.4 Advanced Nonlinear Control System Design</b> .....	34
<b>2.5 Regenerative Braking and Battery Storing Capabilities</b> .....	35
<b>2.6 PSIM and HIL Technology</b> .....	41
<b>2.7 Chapter Summary</b> .....	42
<b>Chapter 3. System Modeling and Engineering Design</b> .....	44
<b>3.1 Modeling and Design of the Linear Synchronous Motor</b> .....	45
<b>3.2 Modeling and Mathematical Analysis of the DC-AC Converter (The Three Phase Inverter)</b> .....	48
<b>3.3 Modeling of SPWM and SVPWM</b> .....	50
<b>3.4 Modeling of the Field Oriented Control</b> .....	52
<b>3.5 Modeling of the Regenerative System</b> .....	56

<b>Chapter 4. Design Simulation in PSIM .....</b>	<b>62</b>
<b>4.1 Simulation of the Three – Phase Inverter .....</b>	<b>62</b>
<b>4.2 Simulation of the Motor Control and Drive System .....</b>	<b>64</b>
<b>4.2.1 Open Loop Controller Design .....</b>	<b>64</b>
<b>4.2.2 Current Controller Design .....</b>	<b>65</b>
<b>4.2.3 Speed Controller Design .....</b>	<b>69</b>
<b>4.3 Simulation of the Battery and Regenerative System .....</b>	<b>72</b>
<b>4.3.1 Simulation of the Lithium-Ion Battery .....</b>	<b>72</b>
<b>4.3.2 Simulation of the DC-DC Converter .....</b>	<b>76</b>
<b>4.4 Full Integration and Results .....</b>	<b>84</b>
<b>4.5 Simulations with LSM .....</b>	<b>88</b>
<b>Chapter 5. Typhoon HIL Design and Simulation .....</b>	<b>90</b>
<b>5.1 Offline Drive Simulation in Typhoon HIL .....</b>	<b>90</b>
<b>5.2 Online Hardware in the Loop Experimental Setup and Results .....</b>	<b>91</b>
<b>Chapter 6. Conclusions .....</b>	<b>97</b>
<b>References .....</b>	<b>99</b>

## List of Tables

### Chapter 2

Table 2.0: LIM vs. LSM Initial Analysis.....	22
--	----

### Chapter 3

Table 3.0: General Design Parameter for the Hyperloop System.....	44
---	----

Table 3.1: Three Phase Inverter – Modes of Operation per Half Cycle.....	49
--	----

### Chapter 4

Table 4.1. AC sweep parameters.....	66
-------------------------------------	----

Table 4.2. Controller Parameters.....	69
---------------------------------------	----

Table 4.3. Specification of Battery Model in PSIM based on Panasonic - NCR18650B.....	73
---	----

Table 4.4. Specification of DC-DC Buck Converter.....	76
---	----

## List of Figures

Fig. 2.1: Electromagnetic excitation system of a LSM, adapted from [22].....	22
Fig. 2.2: Per-phase equivalent circuit of a synchronous motor, adapted from [23].....	23
Fig. 2.3: Torque – Speed Characteristics, adapted from [22] .....	24
Fig. 2.4: Typical three – phase inverter topology [32] .....	27
Fig. 2.5: Space vectors generated by three-phase VSI, adapted from [32].....	29
Fig. 2.6: Field oriented control block diagram, adapted from [32].....	32
Fig. 2.7: The 4 - quadrant operation of a rotary machine .....	36
Fig. 2.8: Basic topologies for DC-DC converters, adapted from [31].....	37
Fig. 2.9: Canonical switching cell and CSC based bidirectional power flow [32].....	38
Fig. 3.1: Calculated Speed – Time Profile.....	46
Fig. 3.2: Circuit Diagram of Three-Phase Inverter, adapted from [34] .....	48
Fig. 3.3: Inverter circuit equivalents at each mode, adapted from [34].....	49
Fig. 3.4: Three-phase VSI bipolar PWM implementation, adapted from [32].....	51
Fig. 3.5: Field - oriented control algorithm (Block Diagram) .....	52
Fig. 3.6: Proportional - Integral block diagram .....	53
Fig. 3.7: Multiplexer blocks diagram & truth table .....	54
Fig. 3.8: Buck-type bidirectional DC-DC converter.....	56
Fig. 3.9: Bidirectional DC-DC converter in (a) buck mode operation & (b) boost mode operation .....	56
Fig. 3.10: Bi-Directional DC-DC controller based on [51] .....	58
Fig. 3.11: Equivalent Circuit of a Battery.....	59
Fig. 3.12: Block diagram for lithium ion battery model, adapted from [54] .....	60
Fig. 4.1: Three Phase Inverter SPWM .....	62
Fig. 4.2: Three Phase Inverter Waveforms .....	63
Fig. 4.3: Three Phase Inverter SVPWM .....	63
Fig. 4.4: SPWM and SVPWM Modulation Scheme Waveforms.....	64
Fig. 4.5: Open loop PSIM setup of drive system.....	65
Fig. 4.6: Open loop Simulation Results .....	65
Fig. 4.7: Perturbation in $I_q$ at (a) 1 V, 10 Hz (b) 1 V, 100 Hz (c) 15 V, 3 kHz.....	66
Fig. 4.8: $I_q$ Frequency Response (AC Sweep).....	67
Fig. 4.9: Perturbation in $I_d$ at (a) 1 V, 10 Hz (b) 1 V, 100 Hz (c) 15 V, 3 kHz.....	67
Fig. 4.10: $I_d$ Frequency Response (AC Sweep).....	67
Fig. 4.11: PI designer in SmartCtrl for $I_q$ frequency response .....	68
Fig. 4.12: Inner PI controller schematic and generated waveforms .....	69
Fig. 4.13: Perturbation in $I_q$ at (a) 1 V, 100 Hz (b) 1 V, 1 kHz.....	70
Fig. 4.14: $\omega_m$ frequency response (AC Sweep) and PI designer in SmartCtrl for $\omega_m$ frequency response.....	70
Fig. 4.15: Waveforms after adding the speed controller (no load) .....	71
Fig. 4.16: Waveforms after adding the speed controller (full load).....	71
Fig. 4.17: Extracted curves from NCR18650B datasheet.....	72

Fig. 4.18: OCV and Rin vs. SOC discharge curves for the NCR18650B.....	73
Fig. 4.19: Rin vs. SOC charge circuit setup and output curve for the NCR18650B .....	74
Fig. 4.20: Charge Characteristics for the NCR18650B .....	74
Fig. 4.21: Discharge Test for NCR18650B Model.....	75
Fig. 4.22: Charge Test for NCR18650B Model.....	75
Fig. 4.23: Circuit Schematic of the Buck Converter.....	77
Fig. 4.24: (a) Open loop simulation of buck converter and (b) output ripple voltage and inductor ripple current.....	78
Fig. 4.25: Output response of buck converter under 10% of reference and 1 kHz perturbation .	78
Fig. 4.26: AC sweep frequency response of inner current loop of buck converter .....	79
Fig. 4.27: SmartCtrl PI – Tuner for the buck converter.....	80
Fig. 4.28: (a) Inner current control closed loop simulation setup and (b) simulation results .....	80
Fig. 4.29: (a) Vout and IL waveforms after adding voltage loop (b) Steady state waveforms....	80
Fig. 4.30: Open Loop Design of Boost Converter .....	81
Fig. 4.31: Closed Loop Design of Boost Converter.....	81
Fig. 4.32: Steady state waveforms for the boost converter.....	82
Fig. 4.33: PSIM Model for the Bi-Directional DC-DC Converter .....	83
Fig. 4.34: Charging and Discharge Control for the DC-DC Converter .....	84
Fig. 4.35: Complete setup for the Hyperloop LSM propulsion system (based on PMSM).....	84
Fig. 4.36: (a) Complete simulation results and (b) Steady state results – three phase currents, battery voltage, battery current, DC bus voltage after boost (c) Id, Iq and speed command compared to reference.....	86
Fig. 4.37: Motoring mode operation results.....	87
Fig. 4.38: Regenerative braking operation results .....	87
Fig. 4.39: Modelling of the Hyperloop propulsion system in Simulink .....	88
Fig. 4.40: Simulation results from Simulink Model showing (a) measured position over time, (b) speed reference, (c) phase currents, and the resulting (d) thrust curves .....	89
Fig. 5.1: Simulation setup of the Hyperloop drive system in Typhoon HIL .....	90
Fig. 5.2: Typhoon HIL offline simulation panel.....	91
Fig. 5.3: PSIM controller update to account for digital delay .....	92
Fig. 5.4: PSIM schematic for TI DSP .....	92
Fig. 5.5: Typhoon HIL – real time simulation (a) schematic and (b) SCADA setup.....	93
Fig. 5.6: Hardware in the loop setup.....	94
Fig. 5.7: Four pulse width modulation signals generated by TI DSP .....	95
Fig. 5.8: 3-Phase line to neutral voltage waveforms.....	95
Fig. 5.9: 3 - phase motor currents .....	96
Fig. 5.10: Line to neutral voltage waveform of a single phase.....	96

## Nomenclature

LIM	Linear Induction Motor
LSM	Linear Synchronous Motor
PMSM	Permanent Magnet Synchronous Motor
EMS	Electromagnetic Suspension
EDS	Electrodynamic Suspension
POD	Referring to Hyperloop Capsule/Vehicle
FOC	Field Oriented Control
SVPWM	Space Vector Pulse Width Modulation
$u_{abc}$	Stator a, b, c phase to neutral voltages
$R_{abc}$	Stator a, b, c phase resistances
$i_{abc}$	Stator a, b, c phase currents
$L_{abc}$	Matrix of stator phase self and mutual inductances
$L_{aa}, L_{bb}, L_{cc}$	Stator a, b, c phase self-inductances
$M_{ab}, M_{ac}, M_{ba}, M_{bc}, M_{ca}, M_{cb}$	Mutual inductances of stator a, b, c phases
$\theta_r$	Rotor angular position
$\omega_r$	Rotor angular velocity
$\Psi_{Mabc}$	Stator a, b, c phase flux linkages from PMSM
$T_e$	Electromagnetic Torque
$i_d$	Direct axis component of stator current
$i_q$	Quadrature axis component of stator current
SOC	State of Charge
$E_{rated}$	Rated voltage of battery cell
$Q_{rated}$	Rated capacity of battery cell
$E_{cut}$	Maximum capacity of battery cell
$R_{battery}$	Internal resistance of the battery cell
$N_p$	Number of cells in parallel of battery pack
$N_p$	Number of cells in parallel of battery pack
$P_m$	Mechanical Power
$M_f$	Mutual Inductance
$\gamma_o$	Power Angle
$W_m$	Mechanical Work

## **Chapter 1. Introduction**

### **1.1 Background**

Plans are in development for a faster, safer, and better mode of transportation. Today's society faces vast engineering challenges. These challenges are crucial for the growth of the world economy. The rise of the electric vehicle industry has greatly impacted other sectors and industries. Many companies are starting to follow the trend to a better and secure future. Moreover, energy security is a reoccurring issue that needs to be addressed. Industries are researching and developing environmental conscious solutions. Corporations such as Hyperloop One and Transpod are investing heavily on a new electric mode of transportation that can revolutionize the transportation industry. This proposed mode of transportation, known as the Hyperloop, will be key in solving many problems society faces today. Thus, furthering the goals for a better world. SpaceX presented the Hyperloop concept in a white paper. Goals for the proposed system requires a significant improvement in various methods of transportation compared to current systems. Considerations for improvement include safety, speed, cost, sustainability, convenience, etc. [7]. The proposed Hyperloop system requires complex engineering design concepts, combining various aspects of current technology and iterative improvements. There are various parts of the Hyperloop system that requires its own research and development for the system to work to its full potential. Some of these various parts include the design of the pod (e.g. compressor, suspension, onboard power, aerodynamics, etc.), vacuum tube design, propulsion, and levitation systems, etc. In this research, a few of these design challenges were studied, modeled, and integrated. The study addresses various design challenges in the power and control stages for the overall Hyperloop system. More specifically, the study dives into the propulsion system. The concepts of levitation and propulsion systems are

borrowed from existing maglev technology. However, this technology is still new and continuously developing. Further research to improve the maglev's drive system will be very beneficial for the propulsion system designed specifically for the Hyperloop.

## **1.2 Historical Development of Highspeed Railway Transportation and Maglev Systems**

Historically, the development of railway transportation has been observed in many countries around the world. Japan was the first to start the revolution of the high-speed railway. In 1964, they began operation of the first bullet train at speeds greater than 200 km/h [8], [9]. This started the trend in developing highspeed railway transportation. France was the second to build a successful high-speed rail. Other countries in Europe such as Germany also started developing highspeed railways. ICE -1 was their first version of highspeed trains in the country, operating in the early 1990s. The first generation of ICE achieved a maximum speed of 250 km/h [8]. China has also been big contender for high-speed railway development. In 2008, they developed a railway achieving a speed of 350 km/h. The transportation system mentioned here all have one thing in common, friction between the wheels and rails.

Although there are great developments, the railway industry using the conventional railway method is still limited. In recent times, countries like China have invested in maglev technologies. The Shanghai Maglev train has achieved speeds of 430 km/h. Germany's developments of their maglev technology in testing achieved a speed of 505 km/h [10]. Maglev technology works through electromagnets as a guideway facilitating the levitation force (support). The propulsion force is generated via the linear motor [11].

Regarding the levitation force, there are three types of technologies commonly studied. Electromagnetic suspension (EMS), electrodynamic suspension (EDS) and finally hybrid

electromagnetic suspension (HEMS) which uses permanent magnets with electromagnets to reduce the electric power consumption in the EMS method [11]. EMS is seen in transits such as the Korean UTM and Japanese HSST for an integrated levitation and guidance system. EMS is also seen in the German Transrapid; however, their levitation and guidance are separate. The EMS method works by using the magnetic attraction force between the guideway and electromagnets. Albeit the method is naturally unstable due to the characteristics of electromagnets/permanent magnets [11]. This requires a controller to maintain a precise and uniform airgap. However, the control system to maintain this airgap is another challenge on its own [11], [12]. EMS is easier than EDS to implement, the levitation force can be created by itself in zero or low speeds. However, for EDS, it is not possible to levitate in zero/low speeds [11]. As opposed to EMS, the electrodynamic suspension works by using repulsive force for levitation [11]. In this method of levitation, there are magnets attached below the pod. When it moves forward over the guideway (made up of inducing coils or conducting sheets), the induced current will flow through the coil/sheet creating a magnetic field. This creates a repulsive force between the magnetic fields and the permanent magnets onboard. EDS is stable enough magnetically to eliminate the need to control the air gap (around 100 mm). This will allow for variation in loads for cargo transportation and is suitable for high speeds [11]. For the EDS to work, the pod needs to generate speed before it can gain enough induced current to produce the levitation force. Therefore, at start up, the pod will need to travel on ground up to a speed of 100 km/h [11]. It is also important to note that there are two types of magnets that can be used for this method. Permanent magnet (PM) can be used since it will not require an electric power supply. It is also used for smaller systems due to the characteristics of PMs. A popular configuration for maglev trains using PM is known as the Halbach array [11]. Super conducting

magnet (SCM) structure and chemical properties adds a new layer of complexity. However, it has been seen that SCM type EDS systems allowed for world records for speeds of 581 km/h in Japan [11].

In terms of the propulsion force, the maglev trains use linear motors. Similar to a conventional rotary motor, it has stators, rotors and windings. It differs in the sense that the stator, rotor and windings are cut open and flattened out [11]. Two types of commonly used linear motors are the linear induction motor (LIM) and the linear synchronous motor (LSM). For the LIM, the primary part generates the magnetic fields. The secondary induces the electromotive force (EMF) which is the conducting sheet. The EMF generates the eddy currents that interacts with the flux in the air gap between the primary and secondary. This interaction creates the thrust force, which is also known as the Lorenz's force [11]. Either a short primary or a long primary type is used in these linear motors. The short primary type has stator coils on board and conducting sheets are on the guideway. Whereas, for the long primary type, the guideway has the stator coils and the conducting sheets are on board [11]. Each of these have their trade offs. The choice of design depends on the application and budget. The rule of thumb is to use short primary types for low speeds since they cannot exceed 300 km/h. The short primary type is seen used in the Japanese HSST and the Korean UTM. The long primary type is recommended for higher speeds [11]. The LSM has a magnetic source within itself and interaction between the magnetic field and armature currents produce the thrust force. The speed is controlled by the controller frequency. LSM also has two types, comparable to the LIM with the long and short primary types, but regarding the field locations. Additionally, there are two more types for the magnetic field. The first, as seen in the German Transrapid, uses electromagnets with the iron core. The second type, as seen in the Japanese MLX, uses super

conducting magnets with the air core. Due to the higher efficiency and power factor, high speed maglev trains are recommended to use LSM [11].

### **1.3 Problem Statement and Motivation**

To comply with the Paris climate change protocol, the big need to cut on the emissions is a hot topic, thus the next decade will be a Public Mass Transit Era. High speed trains are a key to cut down on the cost and fuel usage of airlines. Recent funding of the corridor of San Francisco to Las Vegas and a similar corridor from Houston to Dallas was a big step forward. Hence, there is a need for the development of a better, safer, and faster mode of transportation. Innovative solution like the Hyperloop concept promises a strong alternative to alleviate various issues with the current situation. Thus, research and development has gone to several aspects of the Hyperloop system. One key factor that differentiates the Hyperloop against any other mode of transport is its speed. To achieve this property, the design must revolve around a frictionless system. One way this is achieved is through the design of the loop itself. This will reduce the air resistance. Combining this with the concepts of magnetic levitation trains will reduce friction force further. Therefore, there is a need to develop a system that can facilitate the force required for vertical levitation and horizontal propulsion. The thesis will outline the design of a propulsion system with its successful integration in the lab at University of Ontario Institute of Technology. Modeling and analysis of the motor and inverter are given with its control methodology. The model is simulated in a PSIM environment with results presented. The power electronics system and the completed drive system will be verified and validated using hardware in the loop technology through Typhoon HIL.

### **1.3 Scope and Objective of the Thesis**

The main objective of this thesis is to research various control methods to produce the required output thrust for both levitation and propulsion. This thesis will provide detailed

modeling of linear synchronous motors and an intensive study on the signal processing and controls. However, it is important to note the levitation system only consumes a portion of the power as opposed to the propulsion system [13]. Thus, this study will focus strongly on the propulsion system.

#### **1.4 Thesis Organization**

The content for this thesis is divided into six chapters. The content of these chapters are summarized as follows:

Chapter 1 includes the problem statement and motivation. It talks in detail about the need for a study on the propulsion and levitation system in a Hyperloop application. The chapter goes over the background of the novel mode of transportation, historical developments of highspeed railway, maglevs, and their drive systems. Additionally, the scope and objectives of the thesis are discussed.

In Chapter 2, a study is made on existing approaches of linear synchronous motor (LSM) control and electric drive systems. This chapter is a literature review of different modelling methods that are needed for facilitating the power and control of the LSM.

Chapter 3 studies the mathematical models in details and provides the required equations for each method studied to further corroborate the model.

Chapter 4 uses the equations discussed in the previous chapter to create a simulation model in the PSIM software. This chapter will also provide the modeling design methodology for the battery and DC-DC converter. Finally, the chapter overviews a Simulink design implementing a permanent magnet linear synchronous motor.

Chapter 5 presents a Typhoon HIL simulation experiment. Analysis is made upon the simulation results, comparing the PSIM design with the HIL results. Verification via real-time results is made. Performance of the simulation model in HIL are observed and detailed. With the use of HIL technology, the proposed model is improved through iterative design, thus achieving the goals of this thesis.

Finally, in chapter 6, the conclusions and areas for future works are discussed. This chapter goes briefly into the challenges of this thesis and the achievements that can be adopted into a real Hyperloop system.

## Chapter 2. Literature Review

This chapter is to provide the reader with context and an in-depth review of existing analysis and techniques studied regarding Hyperloop/maglev drive systems. The chapter will reference various reputable sources to help the reader further understand the theory and concepts. The goal of this chapter is to provide the reader with thorough background knowledge, looking into various techniques. This will also allow a study of the advantages and disadvantages regarding each topic covered in this chapter.

The topic of Hyperloop has been reported in various literature works such as [14], [15]. The work in [14] critiques the achievability by discussing the technical issues in building such an infrastructure. Based on their calculations, they estimate for a Hyperloop pod traveling at 1200 km/h for an estimated weight of 26 000 kg would require 689 kW of power. Additionally, they estimate that the cost for building the Hyperloop infrastructure in Poland (including design, construction, land, etc.) for distances between 3000 – 30 000 km would cost over \$50 billion. In [15], the authors discuss the electric power requirements for a full scale Hyperloop. They estimate for a large freight, a capacity of 58 000 lb would be required for the pod. The paper also estimates a cruise speed of 1012 km/h with 80 % regenerative braking efficiency. The resulting power usage is estimated to be in the megawatt range (820 – 1980 MW). The grid assessment for an integrated Hyperloop system showed high pulsating load profiles. Which could result in high excess of voltage fluctuation, flickering, and large disturbances. A solution the authors provide is using compensation devices (static compensators and static var compensators). Another viable solution they provide is the use of energy storage devices in unison with the grid.

As mentioned above, two types of linear motors are commonly studied regarding propulsion of maglev trains. Linear induction motors are attractive due to their relatively low cost and

complexity. However, compared to the LSM, their power factor is low and because it is not a synchronous machine, the design must include slip. Therefore, the LIM has a lower energy efficiency [13], [16]. Despite the cost and complexity, the linear synchronous motor has various properties that makes it a desirable choice for a maglev motor. The LSM has been reported in various papers such as [17], to be viable solutions for a Hyperloop propulsion system. LSM allows the vehicle to avoid carrying heavy traction motor on board. This is because LSM supplies the traction power by supplying it through the ground coils on the guideway [18]. Moreover, this allows transformers and inverter systems to be on ground rather than on board. Accordingly, the pod system will be significantly lighter allowing for faster speeds. Another outcome would be that the pantograph - catenary can be avoided, reducing concerns regarding mechanical contact problems at high speeds [18]. The study in [19] found that coreless, permanent magnet linear synchronous motor (PM- LSM) can achieve promising results for a relatively low cost. Comparing the LIM and the PM-LSM, the LSM had an efficiency of 95.17% compared to the LIM, which had an efficiency of 17.18%. The power factor of the LSM achieved unity, whereas the LIM had a low value of 0.814 [19]. Although the LSM has greater efficiencies and power factor, the LIM is still a popular choice for many linear motor propulsion systems. This is mainly chosen of the LSM because of the significant infrastructure costs. The study in [20] presents various LIM and LSM data regarding costs, efficiencies, and speed capabilities. They conclude similar findings like the other reports that LIM is a significantly better economical choice at low speeds. Table 2.0 summarizes some of the metrics for deciding on the propulsion motor. Although this is a very simplistic cost analysis, it is still presented for an initial design choice. At first glance, the obvious choice would be the linear induction motor. The cost difference vs the efficiency is significantly siding towards the LIM. However, the LIM's natural limitation of its speed is huge drawback for

Hyperloop applications. To obtain ultra-high speeds, the LSM is clearly the only viable choice currently. The cost versus the speed tradeoff is heavily weighted towards the speed. Moreover, the increase in efficiencies with the LSM may present a case for a reasonable return on investment (ROI).

*Table 2.0. LIM vs. LSM Initial Analysis*

Propulsion	Costs	Efficiency at maximum speeds	Operational Speed
LIM	\$23 million/km	77%	100 km/h or less
LSM	\$50 million/km	87%	200 km/h or more

## 2.1 Linear Synchronous Machines

To simulate the proposed Hyperloop propulsion system, an accurate mathematical model for the LSM is required. This will allow us to study the dynamic behaviour of the physical LSM system. The mathematical model will be composed of a set of equations. Fig. 2.1. shows the electromagnetic excitation system for a linear synchronous motor. The symbol ' $\tau$ ' represents the pole pitch. Before modeling, it is important to understand the rotary synchronous machine and its properties to correctly form mathematical equations describing the motor characteristics. In terms of rotary machines, characteristics such as torque, angular velocity and number of pole pairs can be defined. The linear machine can be defined with similar characteristics, however, in respect to the rotary machine, the terms are defined as thrust, linear speed and pole pitch. It is also important to consider both steady state and transient models. The steady state model study will be beneficial for general understanding. Steady state conditions have constant speed, terminal voltages, currents, amplitudes and frequency [21]. However, this thesis will focus more on the transient model for

robust modeling. The variables mentioned previously (speed, voltages, current, frequency, etc.) vary in transient cases [21]. This thesis will provide steady state equations following the phase coordinate model. The orthogonal (dq) axes and space vector (complex variable) will be used for transient modeling.

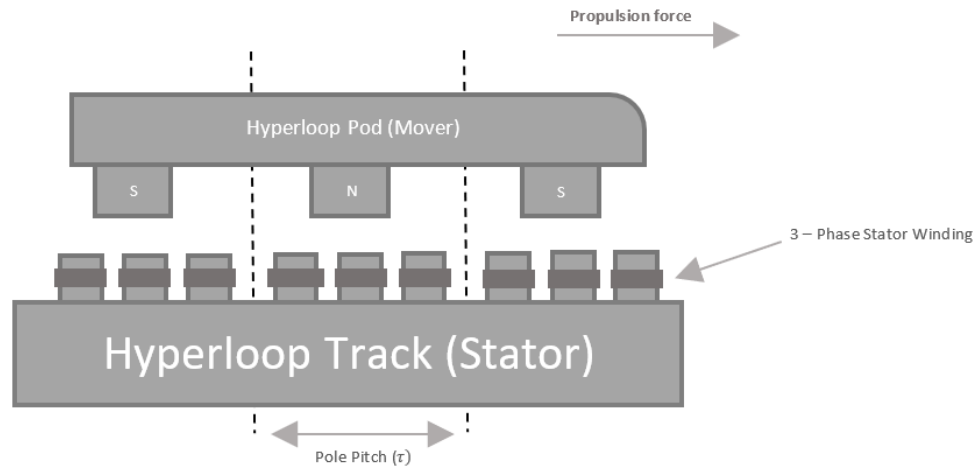


Fig. 2.1: Electromagnetic excitation system of a LSM, adapted from [22]

Literature of rotary synchronous machines are found in various texts such as [22], [21] and [23]. The characteristics of synchronous motors is defined as having a three – phase set of stator currents. These currents produces a rotating magnetic field, causing the rotor of the magnetic field to align with the stator [22]. More specifically, the stator is characterized by an AC multiphase winding currents in the stator. The rotor is characterized by DC (i.e., permanent magnet) excitation. The synchronous motor has both stator and rotor fields which are rotating at a synchronous speed [21]. Fig. 2.2 illustrates the equivalent circuit of the synchronous motor per phase.

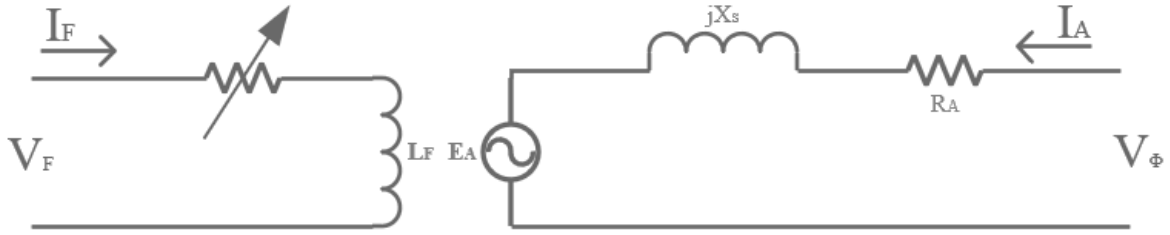


Fig. 2.2: Per-phase equivalent circuit of a synchronous motor, adapted from [23]

Via Kirchoff's voltage law, the equation for the equivalent circuit can be determined. The equations for a rotary synchronous motor are given in Equation 2.1. Where  $V_\phi$  is the output voltage,  $E_a$  is the internal voltage,  $X_s$  is the synchronous reactance of the machine,  $I_a$  is the armature current, and finally  $R_a$  is the armature resistance (i.e., stator resistance).

$$V_\phi = E_a + jX_s I_a + R_a I_a \quad (2.1)$$

$$E_a = V_\phi - jX_s I_a - R_a I_a$$

The speed of the motor is given in Equation 2.2. The speed is determined by the applied electrical frequency  $f_e$ . From this equation, speed of the motor is constant regardless of the load [22]. The torque – speed characteristic of a synchronous motor is illustrated in Fig. 2.3. The torque equation is given in equation 2.3.

$$f_e = \frac{n_m P}{120} \quad (2.2)$$

$$\tau_{ind} = \frac{3V_\phi E_a \sin\delta}{\omega_m X_s} \quad (2.3)$$

The steady-state speed of the motor is constant, independent of the load. The pullout torque, given in Equation 2.4, is the maximum torque the motor can supply. The equation states that the field current (and  $E_a$ ) is directly proportional to the maximum torque of the motor.

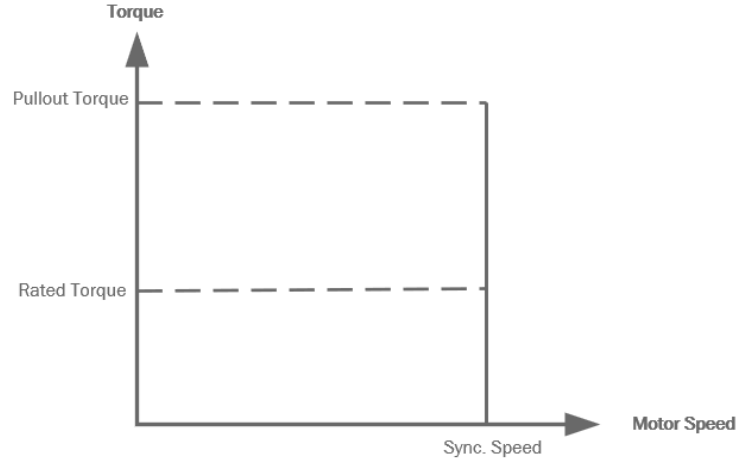


Fig. 2.3: Torque – Speed Characteristics, adapted from [22]

The maximum or pullout torque occurs at  $\delta = 90^\circ$ . Substituting this value into Equation 2.3 will give us the equation to calculate the pullout torque.

$$\tau_{max} = \frac{3V_\phi E_a}{\omega_m X_s} \quad (2.4)$$

Transient models studied in [21] discuss methods of deriving through physical orthogonal model and space vector models. Reference frame theory can reduce the complexity of electric machines and provide a tool for digital implementation for advanced control schemes [24]. The physical model has two windings on the stator. This is denoted as the d and q windings (orthogonal axes). The rotor has three windings. The d-axis holds the  $d_r$  and F and along the q-axis we have  $q_r$ .

$$V_d = R_s I_d + \frac{\partial \psi_d}{\partial t} - \omega_r \psi_q \quad \frac{\partial \psi_d}{\partial \theta_{er}} = -\psi_q \quad \frac{\partial \theta_{er}}{\partial t} = \omega_r \quad (2.5)$$

$$V_q = R_s I_q + \frac{\partial \psi_q}{\partial t} + \omega_r \psi_d \quad \frac{\partial \psi_q}{\partial \theta_{er}} = \psi_d \quad (2.6)$$

$$V_F = R_F I_F + \frac{\partial \psi_F}{\partial t} \quad (2.7)$$

$$0 = R_{dr}I_{dr} + \frac{\partial \psi_{dr}}{\partial t} \quad (2.8)$$

$$0 = R_{qr}I_{qr} + \frac{\partial \psi_{qr}}{\partial t} \quad (2.9)$$

With some manipulations of Equations 2.5 and 2.6, we can obtain Equation 2.10. The left-hand side of the equation is the input power. On the right-hand side, we have copper losses as the first term, magnetic energy variation for the third and fourth terms, and finally for the last term, we have electromagnetic power. The electromagnetic power can be seen in Equation 2.10. Motion equations are derived in Equation 2.12.

$$V_d I_d + V_q I_q = R_s (I_d^2 + I_q^2) + I_d \frac{\partial \psi_d}{\partial t} + I_q \frac{\partial \psi_q}{\partial t} + \omega_r (\psi_d I_q - \psi_q I_d) \quad (2.10)$$

$$P_e = T_e \frac{\omega_1}{p_1} \quad T_e = p_1 (\psi_d I_q - \psi_q I_d) \quad (2.11)$$

$$\frac{J}{p_1} \frac{\partial \omega_r}{\partial t} = T_e - T_{load} \quad \frac{\partial \theta_{er}}{\partial t} = \omega_r \quad (2.12)$$

Flux linkage current relationships are shown in Equation 2.13-2.15.

$$\psi_d = L_{s1} I_d + \psi_{dm} \quad \psi_{dr} = L_{dr1} I_{dr} + \psi_{dm} + L_{drF} (I_{dr} + I_F) \quad (2.13)$$

$$\psi_F = L_{F1} I_F + \psi_{dm} + L_{drF} (I_{dr} + I_F) \quad \psi_{dm} = L_{dm} (I_d + I_{dr} + I_F) = L_{dm} I_{dm} \quad (2.14)$$

$$\psi_q = L_{s1} I_q + \psi_{qm} \quad \psi_{qr} = L_{qr1} I_{qr} + \psi_{qm} \quad \psi_{qm} = L_{qm} (I_q + I_{qr}) = L_{dm} I_{dm} \quad (2.15)$$

Various papers such as [25], study the control algorithms of AC motors using the d-q axes model. A dynamic model of an ironless Halbach permanent magnet linear synchronous motor (PMLSM) is presented in [26]. The model is derived using synchronous reference frame (d-q). The paper in [27] presents a mathematical model for a long stator linear synchronous motor (LLSM) in d-q reference frame and converts it into two phase stationary coordinate system (alpha

– beta). In [28], [29] modeling of PMLSM was developed in MATLAB using the d-q reference frame. The research in [30] develops a LLSM in MATLAB for hardware in the loop integration. The linear synchronous model developed for this thesis is presented in chapter 3.

## **2.2 Three Phase Inverter Design**

As mentioned previously, the three-phase inverter is crucial for the power and control of the linear synchronous motor which provides the propulsion force. The inverter facilitates the conversion of a DC voltage to a controllable (frequency) AC voltage. Inverter circuits use gate-driven semiconductor devices. For high powered applications MOSFETs, IGBTs, and SiC/GaN based devices are used [31]. Control methods of pulse width modulations (PWM) is the basis for creating the switching pattern required for the conversion. Due to the nature of switches, higher – order harmonics are present and require further filtering and other harmonic reduction techniques. The most common DC-AC three phase inverter topology is shown in Fig. 2.4. Each switch is paired with a body diode (antiparallel diode). The topology has three legs, each providing a single-phase voltage to the load. Line to ground voltages are denoted with the

following subscript -  $a_g$ ,  $b_g$ , and  $c_g$ . The load current is the stator current (e.g., stator of the linear synchronous motor).

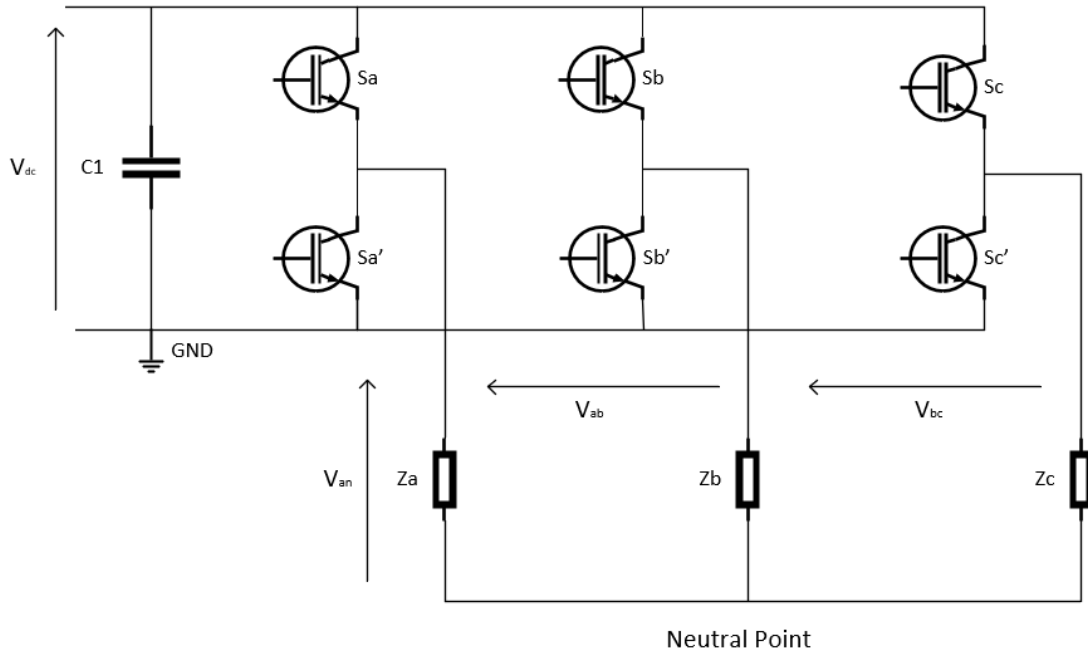


Fig. 2.4: Typical three – phase inverter topology [32]

The inverter is supplied with a DC source. The semiconductor switches are operating in the saturated region or in the cut-off region of the  $i$ - $v$  characteristics. This will theoretically remove power losses (as both voltage and current will not be present) [23]. The semiconductor switches on and off periodically following a certain switching pattern. Generally, either the top leg switch is “on” and the bottom leg switch is “off”, or the bottom leg switch is “on” and the top leg switch is “off”. The semiconductor turns on with a delay of  $T_{on}$  and turns off with a delay of  $T_{off}$ . One undesirable condition that can occur is known as shoot-through. This is when both top leg and bottom leg switches are turned on causing a short circuit. This mean it is crucial to include an extra delay to avoid this condition [23]. The transistors/switches can take either 180-degree conduction or 120-degree conduction. The former is a more popular method, this is due to the properties of

180-degree conduction such as better utilization of switches and higher output voltage production [33]. In 180-degree conduction, the transistors conduct three at a time. The gating signal for this mode of conduction is 1-2-3, 2-3-4, 3-4-5, 4-5-6, 5-6-1, and 6-1-2 [34].

The switching patterns used for the transistors is controlled via modulation techniques. Popular methods include sinusoidal pulse width modulation (SPWM) and space vector modulation (SVPWM). SPWM works by comparing a sinusoidal reference signal (modulation) with a triangle waveform (carrier signal) [35]. SPWM allows the pulse width to be modulated in a sinusoidal fashion. The width of the pulses are proportional to the instantaneous value of the reference sinusoidal wave [31]. This SPWM technique is a sub-branch of the technique known as the unipolar PWM. This is where the output voltage of the inverter switches between zero and the positive output voltage or zero and the negative output voltage. The other SPWM technique is known as the bipolar PWM, which is used in Three – phase inverters. This is where the output voltage of the inverter switches between the negative and positive output values [32]. The bipolar technique can be implemented for three – phase inverters.  $V_{ref}(t)$  is the sinusoidal reference signal and  $V_{tri}(t)$  is the triangular waveform (carrier signal). In modulation, the voltage reference for the carrier wave should be within the modulation range. Otherwise, over-modulation (a state where linearity of the modulation is affected creating saturation) can occur [32]. Overmodulation occurs when the amplitude of the reference is higher than the amplitude of the carrier wave.

Using equation 2.16, we can determine the inverter phase output voltage.

$$v_{xN} = S_x V_{dc}, \quad S_x \in \{0,1\}, \quad x = a, b, c \quad (2.16)$$

$S_x$  represents the binary control signal of each leg [32]. For example, if  $S_a$  is equal to 1, the switch is in the “on” state. Therefore, the phase ‘a’ output node is connected to the positive bar. For this

state we have  $v_{aN} = V_{dc}$ . In the case of  $S_a = 0$ , we have the output node connected to the negative bar. This means for a 3-phase inverter we have  $2^3 = 8$  different switching states. The other modulation technique that is commonly employed is the space vector modulation. The SVPWM switching times are computed using three phase space vector representation of the reference signals and the inverter's switching states [32]. This type of modulation drives the inverter to eight different states. Once again, this allows for  $2^3 = 8$  switching states. It is important to note that there are 7 unique vectors, since  $V_0$  and  $V_7$  (i.e. the inactive vectors) are both equal to zero [32]. These vectors are plotted in the alpha-beta complex plane. All active space vectors are equal in magnitude (i.e.  $|V_k| = 2/3 V_{dc}$ , where  $k = 1, \dots, 6$ ) and each shifted by  $\pi/3$  (i.e.  $\angle\{V_k\} = (k-1)\pi/3$ , where  $k = 1, \dots, 6$ ) [32]. In the proceeding chapters, the formula to calculate the space vectors will be presented.

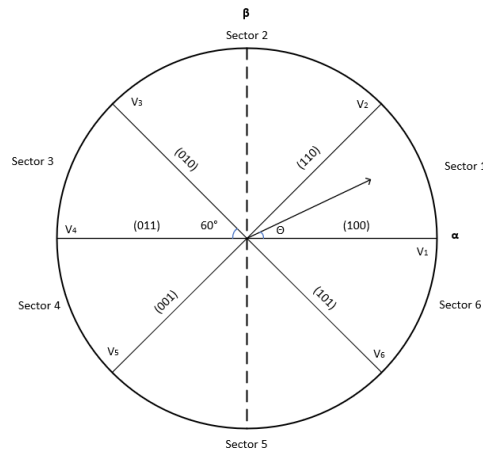


Fig. 2.5: Space vectors generated by three-phase VSI, adapted from [32]

The adjacent pairs of the active vectors correlate to an area in the alpha beta plane. Each area is defined as a sector  $k$  (where  $k = 1, \dots, 6$ ). A generic sector is shown in Fig. 2.5.  $V_s^*$  is the

reference voltage of the space vector. This vector is a fixed amplitude rotating space vector. The amplitude and the angular speed are the same as the sinusoidal references [32]. SVPWM works by generating the PWM over a modulation period  $T_m$  (time average equal to sampled values – i.e., reference vector's amplitude and angular position). The goal is to find the duty cycles of the zero vector and the two active vectors defining the sector in which the reference is located [32]. The research in [36] studies a multiple series structure (single-phase three-level topology) of an inverter system. The topology allows for meeting requirements for voltage and capacity of high-speed maglev systems. Moreover, this topology is used to help with dynamic and static voltage balancing. The modulation method of this study uses SPWM (based on third harmonic injection - THIPWM) over the space vector PWM (SVPWM). This is because SVPWM adds a complexity to implement for multiple topologies. The study achieved a good speed curve as the speed followed the reference well, with a maximum overshoot of 0.6%. Stability was achieved less than 100 seconds, meeting a speed of greater than 540 km/h. The tracking performance of the current loop based on the d and q currents and the three-phase stator current waveforms were adequate.

### **2.3 Field Oriented Control**

A popular control scheme for high dynamic drive systems is known as the field-oriented control (FOC). This method of control is a form of vector control used in electrical drives [37],[24]. As mentioned before, reference frame theory is used to implement digital control schemes for motor drives. The reference frame can be converted using the reference frame transformation given in Equation 2.17. The reverse (dq to abc) transformation is given in Equation 2.18. These transformations are only valid for a balanced system ( $x_a + x_b + x_c = 0$ ) The equation is used to transform three phase abc-axis to the equivalent d-q axis.

$$\begin{bmatrix} x_d \\ x_q \end{bmatrix} = \frac{2}{3} \begin{bmatrix} \cos\theta & \cos(\theta - 120^\circ) & \cos(\theta + 120^\circ) \\ -\sin\theta & -\sin(\theta - 120^\circ) & -\sin(\theta + 120^\circ) \end{bmatrix} \begin{bmatrix} x_a \\ x_b \\ x_c \end{bmatrix} \quad (2.17)$$

$$\begin{bmatrix} x_a \\ x_b \\ x_c \end{bmatrix} = \begin{bmatrix} \cos\theta & -\sin\theta \\ \cos(\theta - 120^\circ) & -\sin(\theta + 120^\circ) \\ \cos(\theta + 120^\circ) & -\sin(\theta + 120^\circ) \end{bmatrix} \begin{bmatrix} x_d \\ x_q \end{bmatrix} \quad (2.18)$$

The abc axis' are in the stationary reference frame, and the d-q (direct – quadrature) are in synchronous reference frame. The stationary reference frame does not rotate and the dq axis does rotate at a synchronous speed (angular electrical speed -  $\omega_e$ ). The angle  $\theta$  can be calculated using equation 2.19.

$$\theta(t) = \int_0^t \omega_e(t) dt \quad \omega_e = 2\pi f_s \quad (2.19)$$

Another important transformation is conversion of three-phase variables to two-phase variables [24]. This is known as the abc to alpha-beta transformation. When the rotating speed of the two-phase reference frame is set to a value of  $\omega_e = 0$ , then it is considered that both two phase and three phase frames are stationary in space. The two-phase stationary frame is known as the alpha beta axis frame of reference. The transformation between three-phase to two-phase, theta is set to zero. The transformation is given in Equation 2.20 – 2.21.

$$\begin{bmatrix} x_\alpha \\ x_\beta \end{bmatrix} = \frac{2}{3} \begin{bmatrix} 1 & -1/2 & -1/2 \\ 0 & \sqrt{3}/2 & -\sqrt{3}/2 \end{bmatrix} \begin{bmatrix} x_a \\ x_b \\ x_c \end{bmatrix} \quad (2.20)$$

$$\begin{bmatrix} x_a \\ x_b \\ x_c \end{bmatrix} = \begin{bmatrix} 1 & 0 \\ -1/2 & \sqrt{3}/2 \\ -1/2 & -\sqrt{3}/2 \end{bmatrix} \begin{bmatrix} x_\alpha \\ x_\beta \end{bmatrix} \quad (2.21)$$

FOC requires both d-q constants as input reference. The torque component is aligned with the q co-ordinate and the flux component is aligned with the d co-ordinate. The torque can be

controlled by controlling the torque component of the stator current. This is because there is a linear relationship between torque and torque component,  $i_{sq}$ , when the rotor flux is maintained at a constant value ( $m \propto \phi_r i_{sq}$ ) [38]. Fig. 2.6 illustrates the basic scheme for FOC for an AC-motor.

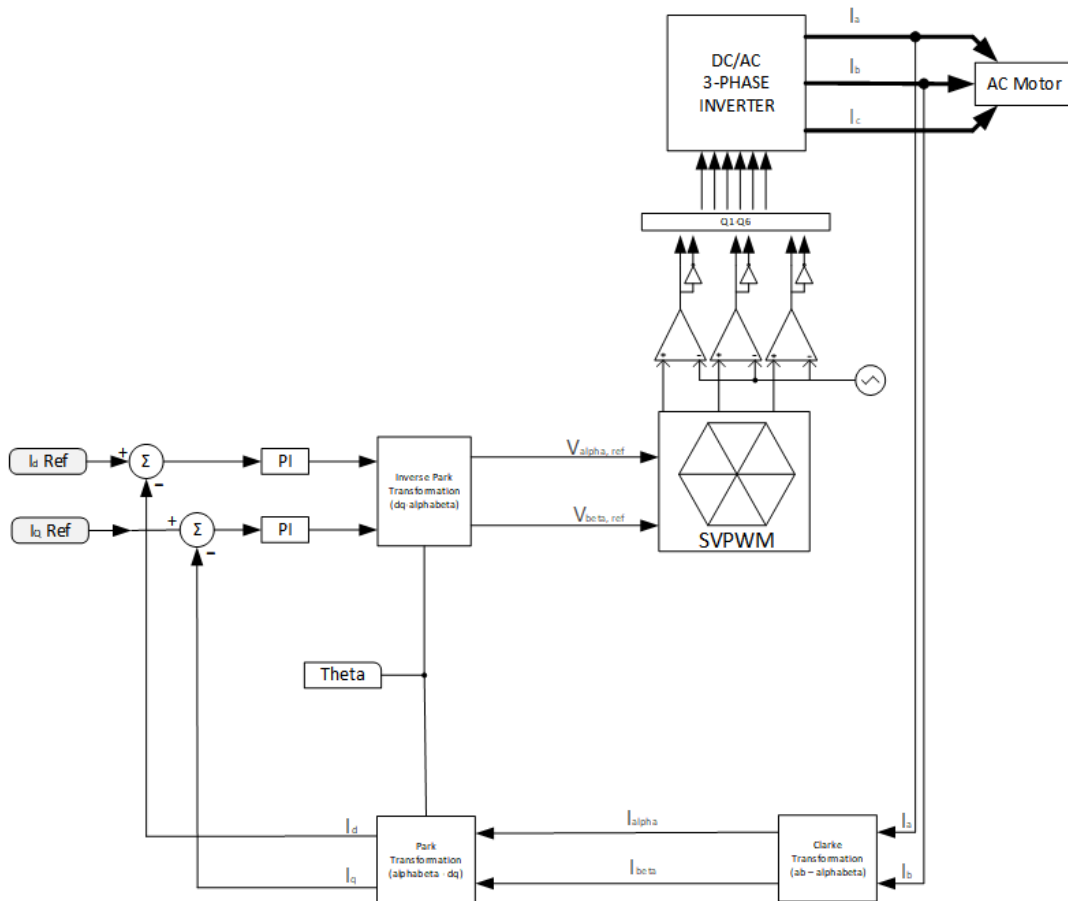


Fig. 2.6: Field oriented control block diagram, adapted from [32]

The scheme of FOC works by measuring two phases (a & b) currents from the motor. The ab currents are converted using the transformation in Equation 2.22 (Clarke Transformation). The output alpha-beta currents are then transformed using Equation 2.23 (Park Transformation).

$$\begin{cases} i_{s\alpha} = i_{\alpha} \\ i_{s\beta} = \frac{1}{\sqrt{3}}i_{\alpha} + \frac{2}{\sqrt{3}}i_{\beta} \end{cases} \quad (2.22)$$

$$\begin{cases} i_{sd} = i_{s\alpha}\cos\theta + i_{s\beta}\sin\theta \\ i_{sq} = -i_{s\alpha}\sin\theta + i_{s\beta}\cos\theta \end{cases} \quad (2.23)$$

The d-q current outputs are then compared to the flux ( $i_{sdref}$ ) and the torque references ( $i_{sqref}$ ). Therefore, the motor can be controlled by varying the flux reference and obtaining the rotor flux position [38]. For a PMSM, the rotor flux is constant (set by the PMs), thus the flux reference should be set to zero. The torque reference can be set via a speed regulator. After comparing, the value is inputted to proportional integral regulators (current regulators). The current regulators calculate the dq voltage references which are then converted to alpha beta using the transformation given in Equation 2.24. These transformed values are used to generate the switching patterns following the SVPWM method. The output from the SVPWM block are used to drive the inverter.

$$\begin{cases} v_{saref} = v_{sdref}\cos\theta - v_{sqref}\sin\theta \\ v_{sbref} = v_{sdref}\sin\theta + v_{sqref}\cos\theta \end{cases} \quad (2.24)$$

The study in [39] develops electromagnetic thrust and levitation force using two – phase rotating reference frame for a PMLSM. The maglev PMLSM has two independent stator windings (one for thrust and the other for suspension). The pod acts as rotor with permanent magnets arranged in the Halbach array. The study simulates the RFOC (rotor field-oriented control) of PMLSM in PSIM. The proposed FOC scheme uses two closed loops. It includes an outer PI speed controller and an inner PI current controller. The FOC system requires three sensor values (current, position and speed). Additionally, the study dives into minimum switching loss SVPWM method. The motivation for this was because conventional SVPWM cannot effectively reduce losses and harmonics.

Sensor-less control has been an emerging area of research for maglev systems. The paper in [40] states the drawbacks from using magnetic encoders (to obtain position and speed values). It mentions that the cost of encoders will be high as they will be required to be installed across the long stator. This brings in issues regarding maintenance. And lastly, encoders are restricted by environmental factors (e.g. temperature, humidity, vibrations). The paper presents a disturbance observer based senseless control system for linear permanent magnet motors. The basis of the system uses back EMF observers and a phase locked loop to estimate the position. The performance of the sensor-less control system was on par with the actual encoder.

The study in [30] also dives into sensor-less control method using a similar electromotive force based algorithm (extended electromotive force – EEMF). Using the EEMF algorithm, the mover's position can be obtained. The angle deviation can be corrected using phase-lock loop (PLL). The simulation results achieved a fast convergence.

## **2.4 Advanced Nonlinear Control System Design**

As mentioned previously, sensor less control of PMLSM can be very beneficial. An emerging topic of utilizing sliding mode control theory has been studied in various research. Sliding mode control is a robust mode of control for non-linear systems. This advanced mode of control also provides a practical control strategy for FOC [41]. In FOC, measured variables include the mover position, stator currents and DC field currents. In addition, for suspension control, air gap is also measured. Sliding mode control (SMC) can be used to provide a robust vertical speed observer [42].

The paper in [43] studies a method of observing the variables (sensor-less control) required in the feedback loop (as mentioned above). The study implements a sliding mode observer based

on back-EMF method. The process works by first observing the terminal current and voltage from the motor. Next, estimate the motor speed and position signals from the back-EMF. The sigmoid function is used as the basis of the sliding mode switching function (to reduce the chattering effect caused by SMC), improving efficiency and estimation accuracy. The sigmoid function is given in equation 2.25. Where  $a$  and  $b$  are control mutation amplitudes of the output,  $c$  is the control value of its mutation time,  $d$  manipulates the slope of the sigmoid function, and finally,  $m$  is the jump range value.

$$f(t) = \frac{1}{a + be^{c-dt}} - m \quad (2.25)$$

The sigmoid function can be adjusted to provide an approximate switch function by setting parameters to values mentioned in the study.

The simulation results show that the chattering effect was eliminated. Regarding the estimation, the error for speed estimate was 1.2% at transient. At steady state, the error reduced to 0.08%. These values were comparable to the estimates with a mechanical sensor. The study achieved a sliding mode observer with high-speed response and robustness to estimate the motor speed and position for a PMLSM.

## **2.5 Regenerative Braking and Battery Storing Capabilities**

With the rise of the electric vehicle industry, regenerative braking and sophisticated battery storing capabilities have been a popular interest in the research of these topics. Regenerative braking will allow some energy to be recovered as opposed to dissipating the excess into a braking resistor [44]. The excess generated energy through a regenerative braking system can be directed from the motor to the source battery. In terms of rotary machine, a typical speed torque chart is given in Fig. 2.7. When the direction of the torque and speed are same, we have motoring mode

of operation (either forward or reverse). When the direction of torque and speed are in the opposite direction, we have braking mode of operation (either forward or reverse) [45]. Thus, there are two cases where the motor is in a motoring mode of operation and two cases where the motor is in the generation mode of operation. In terms of power ( $P = \tau \omega$ ), a negative value indicates generation mode, and a positive value indicates motoring mode. With the use of FOC, regenerative braking for LSM can be achieved [42].

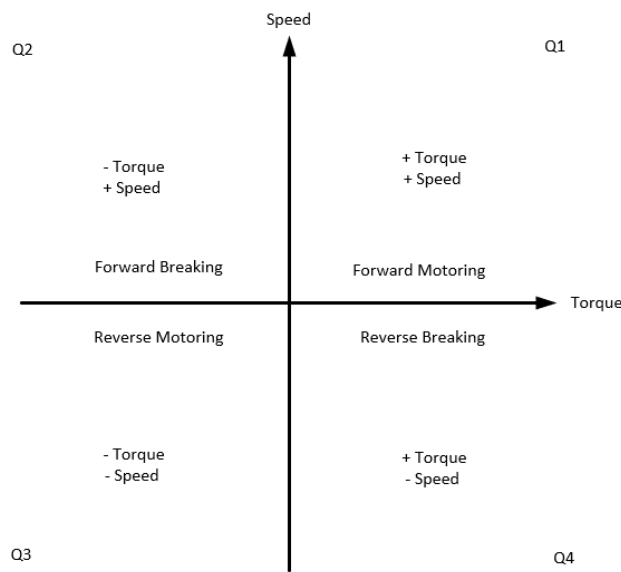


Fig. 2.7: The 4 - quadrant operation of a rotary machine

To implement regenerative braking, the converter should be able to receive the generated energy [42], [45]. This can be achieved with a DC-DC bidirectional voltage source converter. In general, there are various topologies for the DC-DC converter, each suited for its application. Converters of this class are either unidirectional (power flowing in one direction) or bidirectional (power flowing in both direction) [32]. The three basic topologies for a DC-DC converter is known as the buck, boost, and the buck-boost converter [31]. These topologies are illustrated in Fig. 2.8. The buck converter steps down the voltage based on the duty cycle ( $V_{out} = V_{in} * D$ ). The boost

converter on the other hand is a step-up converter. Thus, the output voltage of a boost converter is given by  $V_{out} = V_{in}/(1-D)$ . The last topology is known as the buck-boost converter. This converter can either work in buck mode or boost mode and the voltage is given by  $V_{out} = V_{in} D/(1-D)$ . The inductor value can be calculated by solving for the critical inductance. This value determines the minimum inductor value before the converter operates in the discontinuous conduction mode (DCM) [31]. Furthermore, the capacitor value can be determined by evaluating the output voltage ripple. This is because the capacitor filters the switching frequency ripple and thus, a larger capacitor value attributes to a smaller ripple. The equation used to evaluate this will be presented in chapter 3.

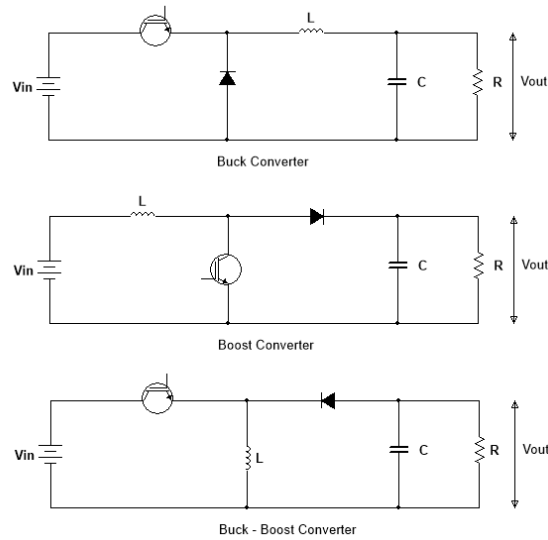


Fig. 2.8: Basic topologies for DC-DC converters, adapted from [31]

To implement a bidirectional converter, we can use the canonical switching cell model (CSC).

As shown in Fig. 2.9., this was used to implement a bidirectional power flow model in [32].

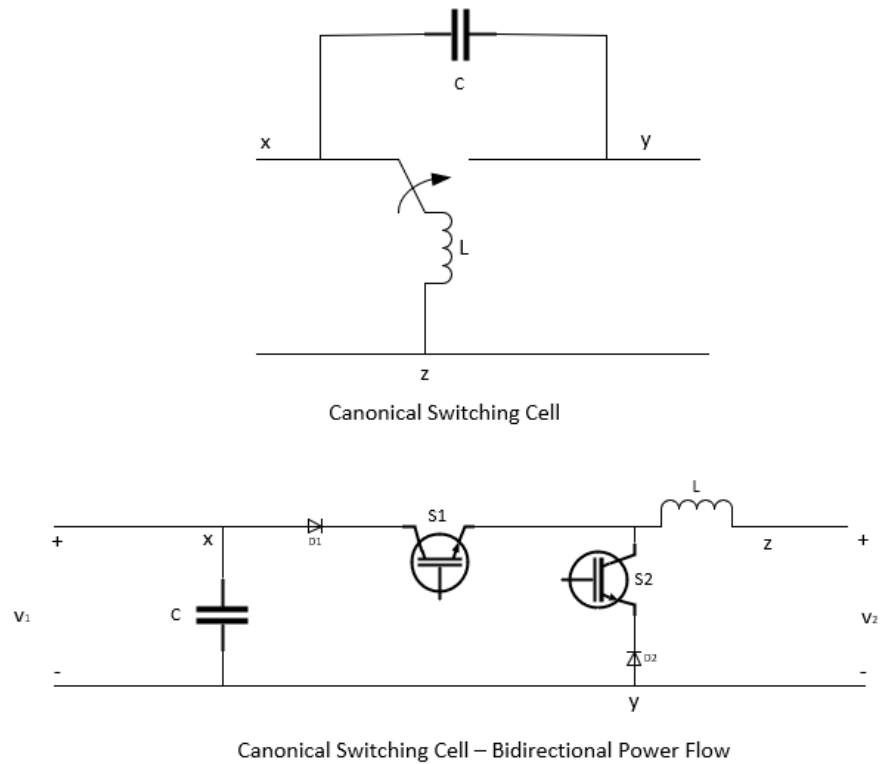


Fig. 2.9: Canonical switching cell and CSC based bidirectional power flow [32]

The topology in Fig. 2.9 works under the condition that the polarity of the external voltages  $V_1$ , and  $V_2$  can change, and the current polarity does not. If  $V_1$  and  $V_2$  are positive, then the transistor  $S_2$  can be turned on continuously. If both voltages are negative, transistor  $S_1$  can be turned on continuously. To control the power flow direction, one of the transistors will be switching and the other will be in a constant ON state (leaving just the diode). For example, the topology works in buck mode when  $S_1$  is switching and  $S_2$  is at an ON state. In this example the power flows from left to right. On the other hand, the topology works in boost mode if  $S_2$  is switching and  $S_1$  is in a constant ON state. Here, the power flows from right to left. There are various research studies established for bidirectional DC-DC converters. A topology similar to the one in Fig. 2.9(b) is studied in [46]. The study in [47] looks into bidirectional DC-DC converters for low voltage energy

storage from a high voltage DC bus of a traction motor. For non-isolated DC-DC bidirectional converters we have buck, boost, and buck-boost type converters. The boost type bidirectional DC-DC converter has a low voltage battery before the converter and high voltage DC link after it (high DC bus voltage > low input source voltage). The buck type bidirectional converter has the battery on the high voltage side. This can be used in hybrid electric vehicle or fuel cell vehicle traction motors [47]. The battery should be rated higher than the DC bus voltage. Lastly, if the input voltage is the same as the bus voltage, then a buck-boost type is appropriate. However, using this type of converter will be costly and is less efficient than the buck and boost types. All in all, this type has been used for high power electric vehicle application where the battery voltage is the same level as the DC bus voltage [47]. The paper also studies isolated converters where a transformer is used to isolate the high and low voltages. However, this introduces additional cost and losses. Since the main objective is an overall integration and modeling simulation, this thesis will opt for a simple non-isolated converter.

To store the excess energy, battery storage capabilities of the system will be required. Battery packs are widely used in electric vehicles. They are made of multiple battery cells connected series and parallel to provide the required power and capacity to meet the demands for propulsion/traction system [32]. Connecting battery cells in series will increase the voltage rating and connecting the battery cells in parallel will increase the capacity of the pack. The research in [48] studies a propulsion system design of a Hyperloop capsule, focusing on the sizing of energy and power needs. The study proposes a method to obtain the values by using weight of the payload and predetermined trajectories. This method optimizes the number of battery cells required. The battery pack is modeled as a BESS pack. Their basic parameter assumption for the capsule includes a combined payload and capsule mass of 8000 kg. The total expected velocity was assumed as

1200 km/h and traveling 226 km – 1000 km. The BESS system is composed of lithium nickel manganese cobalt oxide (NMC) batteries. The authors observed for distances of 500 km to 1000 km it has similar maximum instantaneous power (5.5 MW and 2 MW respectively) to their simulated trajectory. For the shorter distance of 226 km, they found the maximum power of the propulsion system to be larger (6.25 MW) since the cruising speed is shorter. To control the charging and discharging, a battery management system can be implemented. The nature of electric vehicles and their varying load profile (constant acceleration and deceleration) calls for a sophisticated system that can monitor the battery (e.g. charging, discharging, temperature, etc.) [32]. However, for this thesis of the Hyperloop battery system, we will focus mainly on the state of charge (SOC) of the battery. This includes a simulation model to maintain the SOC and avoid overcharging the battery.

## 2.6 PSIM and HIL Technology

To develop accurate simulation results for this thesis, Powersim (PSIM) is intensively used. PSIM provides a solution to simulation and design tools for advanced topics in electrical engineering. The tool is extensively used for developing power electronic converters, motor drives and controllers. The PSIM library consists of various motor models, high power switches, control algorithms (e.g., SVPWM, torque controller, DC-DC charging/discharging operations), lithium-ion battery models and many more. The software provides many model examples and templates as a starting point in many designs that can save time and hassle in designing complex electronic systems and controllers. This also includes their HEV design suite, a complex power train simulation solution for various applications in the electric vehicle realm. Moreover, PSIM provides a solution to automatic code generation for control schematic designed in the simulation software. SimCoder can take a controller schematic designed in PSIM and convert it into c – code. The generated code can then be uploaded to target hardware such as the vast line up of Texas instrument DSP/MCUs. Lastly, PSIM has SmartCtrl integrated with their software. SmartCtrl allows for a rapid controller design for power electronic applications. This will greatly reduce the complexity and time costs for designing controllers. SmartCtrl provides solutions to design digital controllers, verify control loop stability, define digital delay, etc. This will also allow for easy controller implementation on DSPs/MCUs.

In addition to PSIM, Typhoon HIL (hardware in the loop), a novel platform for mathematically modeling of the drive system of the proposed Hyperloop track (LSM), is used. HIL provides real time simulations for design, testing, and validation of power electronic control systems. The HIL technology allows a unique way to develop prototypes without the need to build

a physical system; saving both costs and time, (i.e. the technology promotes the use of quick iterative designs in an affordable matter).

The paper in [49] validates experimental results for their proposed power train model for electric vehicles. Typhoon HIL is used to prototype and create a test bed for their power circuits. Real time simulations for PMSM and other power electronic hardware components are made. This allowed parameters to be changed in simulation run time. Both PSIM and Typhoon was used in their study. The authors developed the control loop in PSIM and the powertrain loop in HIL. The control circuit was generated in PSIM, converted to c – code, and finally downloaded on a Texas instrument controller. The controller was the link to the two software. The HIL results matches those of the PSIM platform.

## **2.7 Chapter Summary**

This chapter referenced the various literature topics required for the development of a drive system for Hyperloop propulsion and levitation design. A review of synchronous motors was made. The modeling of the synchronous motor was studied and referenced. This will be referenced in the model of the LSM in chapter 3. As reviewed, the drive system for the LSM contains a power stage and a control stage. A review of the power stage (inverter) was made. The three – phase inverter is required for a typical drive to convert uncontrollable DC into controllable AC. The control stage was then studied. Field oriented control is a popular method in maglev and other electric vehicle drive design. The basic concepts and advanced modeling were studied from the referenced literature. An advanced method of sensor less FOC was then reviewed. Sliding mode observers were used in the referenced literature for sensor less control. A brief introduction to regenerative braking and battery storage was made. Finally, a look into a novel platform that will

be used in the following chapter was mentioned. Typhoon HIL provides real time simulation of proposed design. This technology will be used in the following chapters to validate the proposed models. The following chapters will provide experimental results.

All in all, the literature review is meant to help the reader get a background of the detailed system. Advanced and novel area of research regarding the topics were reviewed. Due to the scope and overall goals of this thesis, not everything mentioned in this chapter will be implemented. This chapter highlighted the most recent activities in this topic, but the thesis will handle this in a different and unique way. It will highlight the modeling of the overall propulsion system in PSIM. Results obtained by Typhoon will confirm the validity of the PSIM model through comparison of the results. In addition, the manufacturing of the power converters and the integration of the motor will be highlighted. Videos and experimental results of the successful integration and operation of the bidirectional operation in motoring and braking modes; will be given and presented as well for the first time.

### Chapter 3. System Modeling and Engineering Design

The following chapter will go through the dynamic modeling for the various systems of interest in the Hyperloop concept. The models that are described in this chapter will be used in chapter 4 for simulation purposes. First, we will go in detail into the modeling of a linear synchronous motor. Second, we will present the conventional 3-phase inverter model used to convert the DC voltages. Third, pulse width modulation techniques (SPWM and SVPWM), design equations and modeling will be presented. Forth, a detailed look into field-oriented control will be made. This subchapter will present the modeling equations and control theory to achieve the controller design required FOC. Lastly, we will investigate a bidirectional converter for our application. This will include modeling of the battery used to store the generated power. The models discussed in this chapter will be implemented in pair with PSIM and Typhoon HIL to validate and verify the integration of the models. Assumptions and reference design from various sources were made to determine design parameters such as mass, speed, acceleration, etc. These parameters are later used to model the system and study the simulated results. The basic design parameters for the proposed Hyperloop modeling are given in table 3.0.

*Table 3.0. General Design Parameter for the Hyperloop System*

Parameter	Value	Notes
Total Pod Mass ( $m_p$ )	$m_p = 15000$ [kg]	Based on [7]
Steady state velocity ( $v_{const}$ )	$v_{const} = 300$ [m/s]	Based on proposed pod velocity of Virgin Hyperloop One
Acceleration (a)	$a = 1.96$ [m/s <sup>2</sup> ] (i.e. 0.2G)	Based on proposed pod velocity of Virgin Hyperloop One
Deceleration (d)	$d = 1.96$ [m/s <sup>2</sup> ] (i.e. 0.2G)	Based on proposed pod velocity of Virgin Hyperloop One
Distance (s)	$s = 615$ [km]	Based on Virgin Hyperloop One (Los Angeles to San Francisco)

### 3.1 Modeling and Design of the Linear Synchronous Motor

In an LSM based Hyperloop system, we have the track (stationary part) and the pod (moving part). The speed of the moving part can be calculated using equation 3.0a. Where,  $v_s$  is the synchronous speed,  $\omega$  is the angular input frequency and  $\tau$  is the pole pitch (in mm). The thrust force (output power divided by the synchronous speed) can be calculated using equation

$$v = v_s = 2f\tau = \frac{\omega}{\pi}\tau \quad (3.0a)$$

$$F_x = \frac{P_{out}}{v_s} \quad (3.0b)$$

The previous equations are used for basic motion calculation. Additionally, speed-time and thrust-time curves can be created for the linear motion as shown in Fig. 3.1. To solve for the linear motion waveforms, equations 3.0c and 3.0d can be used. The acceleration time is denoted as  $t_1$  (steady-state speed over acceleration). The deceleration time is given as  $t_3$ , where  $d$  is the deceleration. Lastly, the  $t_2$  is the constant speed time which can be calculated by subtracting the total time ( $t_{total} = t_1+t_2+t_3$ ) with the acceleration and deceleration times. The total distance of the run is denoted as 's'.

$$t_1 = \frac{v_{const}}{a} \quad t_2 = t - t_1 - t_3 = t - v_{const}\left(\frac{1}{a} + \frac{1}{d}\right) \quad t_3 = \frac{v_{const}}{d} \quad (3.0c)$$

$$s = tv_{const} - kv_{const}^2 \quad k = \frac{1}{2}\left(\frac{1}{a} + \frac{1}{d}\right) \quad v_{const} = \frac{t}{2k} - \sqrt{\left(\frac{t}{2k}\right)^2 - \frac{s}{k}} \quad (3.0d)$$

The equation in 3.0e can be used to solve for the thrust profile.  $F_{x_{rms}}$  represents the rms thrust force in the x-direction based on the duty cycle [50].

$$F_{xrms}^2 \sum t_i = \sum F_{xi}^2 t_i \quad F_{xrms} = \sqrt{\frac{F_{x1}^2 t_1 + F_{x2}^2 t_2 + F_{x3}^2 t_3 + \dots + F_{xn}^2 t_n}{t_1 + t_2 + t_3 + \dots + t_n}} \quad (3.0e)$$

Based on the parameters in table 3.0, we can model the speed-time curve given in Fig. 3.1.

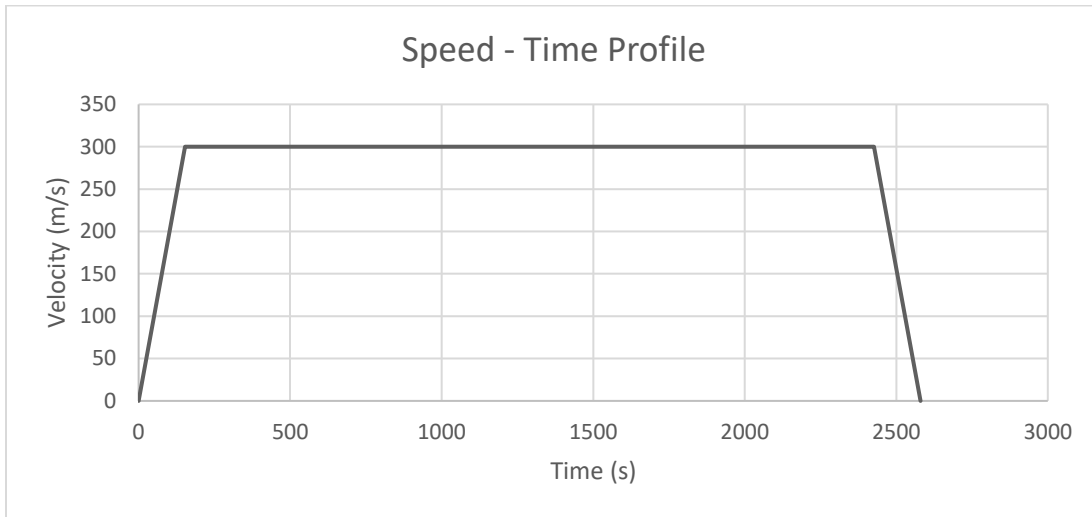


Fig. 3.1: Calculated Speed – Time Profile

The circuit model for the linear synchronous motor can be derived based on the rotary synchronous motor equations as presented in the previous chapter (Equations 2.4 – 2.11). The circuit model for the linear synchronous motor is presented in equations 3.1 – 3.3.

$$V_d = R_1 i_d + \frac{\partial \psi_d}{\partial t} - \omega_r \psi_q \quad \psi_d = L_{a1} i_d + L_{dm} (i'_F + i_d) \quad (3.1)$$

$$V_q = R_1 i_q + \frac{\partial \psi_q}{\partial t} + \omega_r \psi_d \quad \psi_q = L_q i_q \quad (3.2)$$

$$V'_F = R'_F i'_F + \frac{\partial \psi'_F}{\partial t} \quad \psi'_F = L_{F1} i'_F + L_{dm} (i'_F + i_d) \quad (3.3)$$

$$\frac{i'_F}{i_F} = \frac{M_{aF}}{L_{dm}} = K_F \quad V'_F = \frac{1}{K_F} V_F \quad \omega_r = \frac{\pi}{\tau} U \quad (3.4)$$

$$F_x = \frac{2\pi}{3\tau} (L_{dm} i'_F + (L_{dm} - L_{qm}) i_d) i_q \quad (3.5)$$

$$\frac{M}{2} \frac{dU}{dt} = F_x - F_{load} \quad (3.6)$$

$V_d, V_q$  are the stator voltages in the d and q axis, respectively.  $i_d$  and  $i_q$  are the stator currents.  $R_1$  is the armature winding resistance.  $\psi_d, \psi_q$  are the flux components. The inductive windings are represented by  $L_d$  and  $L_q$ . Additionally, these inductances can be calculated as shown in equation 3.7. Where  $L_{dm}$  and  $L_{qm}$  are the magnetizing inductance.  $L_{a1}$  is the leakage inductance. The angular frequency of armature current is represented by  $\omega_r$  (i.e., angular rotor velocity), where  $U$  is the linear synchronous velocity and  $\tau$  is the pole pitch. In the case of electromagnetic excitation, there exists field winding resistance,  $R'_f$  [50]. The variable  $i'_f$  is the field excited current.  $\psi_f$  is the excitation linkage flux.  $L_{F1}$  represents the field leakage inductance.

$$L_d = L_{dm} + L_{a1} \quad L_q = L_{qm} + L_{a1} \quad (3.7)$$

The propulsion force can be calculated using Equation 3.5. Equation 3.6 relates the mass ( $\mathbf{M}$ ), acceleration ( $a = dU/dt$ ) and movement resistance force ( $\mathbf{F}_{load}$ ).  $M/2$  represents the mass of one side of the vehicle powered by one inverter for one active stator section [42].

### 3.2 Modeling and Mathematical Analysis of the DC-AC Converter (The Three Phase Inverter)

Through Fourier analysis, the line-to-line voltage  $v_{ab}$ ,  $v_{bc}$ , and  $v_{ca}$  is given in Equation 3.8.

$$v_{ab}(t) = \sum_{n=1,3,5,\dots}^{\infty} \frac{4V_{dc}}{n\pi} \cos \frac{n\pi}{6} \sin n \left( \omega t + \frac{\pi}{6} \right) \quad (3.8a)$$

$$v_{bc}(t) = \sum_{n=1,3,5,\dots}^{\infty} \frac{4V_{dc}}{n\pi} \cos \frac{n\pi}{6} \sin n \left( \omega t - \frac{\pi}{2} \right) \quad (3.8b)$$

$$v_{ca}(t) = \sum_{n=1,3,5,\dots}^{\infty} \frac{4V_{dc}}{n\pi} \cos \frac{n\pi}{6} \sin n \left( \omega t - \frac{7\pi}{6} \right) \quad (3.8c)$$

Three – phase inverters for a Y – connected load works in three modes of operation per half cycle. Table 3.1 summarizes the pulse voltages and line to line voltages for its respective mode.

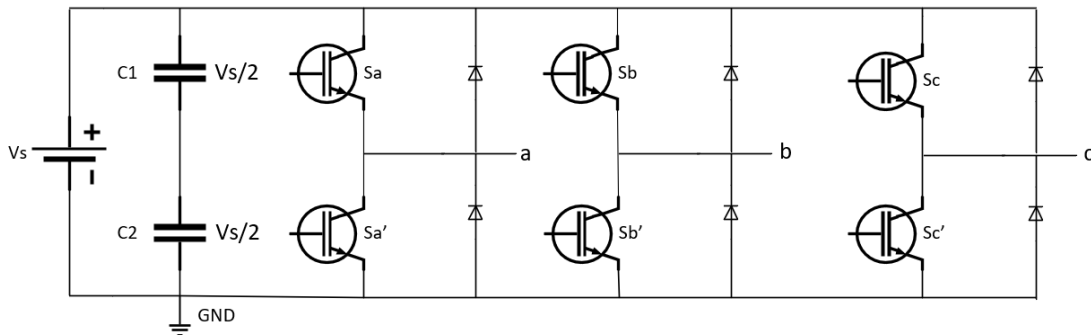


Fig. 3.2: Circuit Diagram of Three-Phase Inverter, adapted from [34]

The line to ground voltages can be found by basic circuit analysis of Fig. 3.2. As mentioned in the previous chapter, at various instants only three switches are conducting. At each instant, the line to neutral voltages can be calculated through circuit analysis. The equivalent circuit for each mode is shown in Fig. 3.3. The line-to-line voltages can be calculated using Equation 3.9.

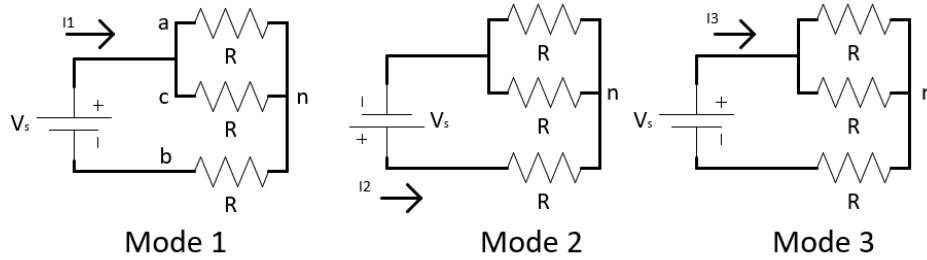


Fig. 3.3: Inverter circuit equivalents at each mode, adapted from [34]

Table 3.1. Three Phase Inverter – Modes of Operation per Half Cycle

Mode	ON	Line to load neutral			Line to line		
$0 \leq \omega t \leq \frac{\pi}{3}$	$Q_1, Q_5,$ $Q_6$	$v_{an} = \frac{1}{3}V_{dc}$	$v_{bn} = -\frac{2}{3}V_{dc}$	$v_{cn} = \frac{1}{3}V_{dc}$	$v_{ab} = V_{dc}$	$v_{bc} = -V_{dc}$	$v_{ca} = 0$
$\frac{\pi}{3} \leq \omega t \leq \frac{2\pi}{3}$	$Q_1, Q_2,$ $Q_6$	$v_{an} = \frac{2}{3}V_{dc}$	$v_{bn} = -\frac{V_{dc}}{3}$	$v_{cn} = \frac{-V_{dc}}{3}$	$v_{ab} = V_{dc}$	$v_{bc} = 0$	$v_{ca} = -V_{dc}$
$\frac{2\pi}{3} \leq \omega t \leq \pi$	$Q_1, Q_2,$ $Q_3$	$v_{an} = \frac{1}{3}V_{dc}$	$v_{bn} = \frac{1}{3}V_{dc}$	$v_{cn} = -\frac{2}{3}V_{dc}$	$v_{ab} = 0$	$v_{bc} = V_{dc}$	$v_{ca} = -V_{dc}$

Equation 3.10 provides the line-to-line rms voltage. The rms nth component of the line voltage is given in equation 3.11. Lastly, the rms value of the line to neutral voltage can be found using 3.12.

$$V_L = \left[ \frac{2}{2\pi} \int_0^{\frac{2\pi}{3}} V_s^2 d(\omega t) \right]^{1/2} = \sqrt{\frac{2}{3}} V_s = 0.8165 V_s \quad (3.10)$$

$$V_{Ln} = \frac{4V_s}{\sqrt{2}n\pi} \sin \frac{n\pi}{3} \quad (3.11)$$

$$V_p = \frac{V_L}{\sqrt{3}} = \frac{\sqrt{2}V_s}{3} = 0.4714 V_s \quad (3.12)$$

### 3.3 Modeling of SPWM and SVPWM

To generate the pulse width modulation, SPWM and SVPWM methods are employed in this thesis. As mentioned previously, SPWM works by comparing a modulating signal (sinusoid) and a carrier wave (triangular). The amplitude and frequency modulation index are calculated using equations 3.13 and 3.14, respectively.

$$m_a = \frac{V_{p,ref}}{V_{p,tri}} \quad (3.13)$$

$$m_f = \frac{f_s}{f_o} \quad (3.14)$$

$V_{p,ref}$  is the peak value of the reference signal.  $V_{p,tri}$  is the peak value of the triangular waveform. To stay in the linear region of modulation,  $m_a$  should be equal to or less than 1 [32]. Otherwise, the inverter may experience overmodulation effects.  $f_s$  is the frequency of the triangular carrier wave.  $f_o$  is the desired output frequency, this is set by frequency of the reference sinusoid. The voltage equations 3.13-3.14 are the line to line and line to load neutral, respectively.  $V_{xN}$  are the inverter phase output voltages. Implementing the bipolar PWM can be done through a comparator as shown in Fig. 3.4. The complement of these signals can be created with a NOT gate.  $V_{cr}$  is the triangular carrier wave input to the negative terminals of the comparator.  $V_a^*$ ,  $V_b^*$  and  $V_c^*$  are the reference sinusoidal signals shifted by  $120^\circ$ .

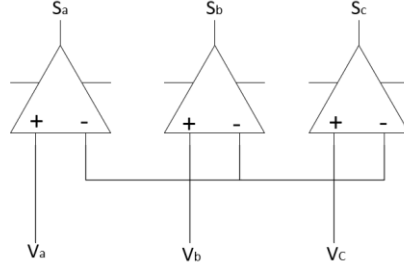


Fig. 3.4: Three-phase VSI bipolar PWM implementation, adapted from [32]

$$v_{ab} = v_{aN} - v_{bN} \quad v_{bc} = v_{bN} - v_{cN} \quad v_{ca} = v_{cN} - v_{aN} \quad (3.13)$$

$$v_{an} = \frac{(2v_{ab} + v_{bc})}{3} \quad v_{bn} = \frac{(2v_{bc} + v_{ca})}{3} \quad v_{cn} = \frac{(2v_{ca} + v_{ab})}{3} \quad (3.14)$$

Another modulation technique that is commonly employed in three phase inverters is the space vector modulation. The voltage of the SVPWM can be defined in the alpha-beta complex plane as seen in equation 3.15. The space vector voltages can also be defined using the switching signal. This is given in equation 3.16. As mentioned in the previous chapter,  $S_a$ ,  $S_b$  and  $S_c$  are the binary switching states where  $S_x \in \{0,1\}$ .

$$v_s = \frac{2}{3} [v_{aN} + av_{bN} + a^2v_{cN}] \quad a = -\frac{1}{2} + j\frac{\sqrt{3}}{2} \quad (3.15)$$

$$v_s = \frac{2}{3} V_{dc} [S_a + aS_b + a^2S_c] \quad (3.16)$$

The goal is to solve for the duty cycle. The following sets of equations in 3.17 - 3.19 can be used to obtain this value.

$$t_k = \frac{3T_m |V_s^*|}{2V_{dc}} \left\{ \cos(\theta - \theta_k) - \sin \frac{(\theta - \theta_k)}{\sqrt{3}} \right\} \quad (3.17)$$

$$t_{k+1} = \frac{3T_m |V_s^*| \sin(\theta - \theta_k)}{V_{dc} \sqrt{3}} \quad (3.18)$$

$$t_0 = T_m - t_k - t_{k+1} \quad (3.19)$$

### 3.4 Modeling of the Field Oriented Control

In chapter 2, we briefly went through the theory of vector / field-oriented control method for motor drives. In this sub-topic we further elaborate on the modeling of this control method. Fig. 3.5 illustrates the main components of the field-oriented control that will be implemented in the simulation.

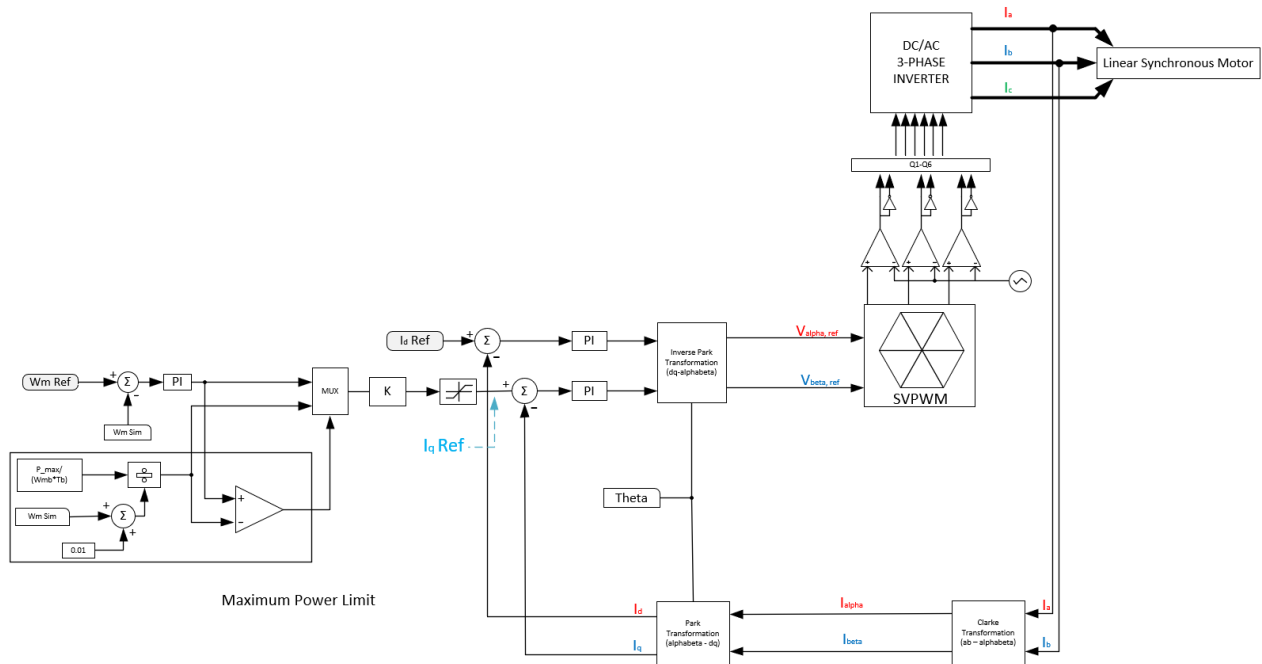


Fig. 3.5: Field - oriented control algorithm (Block Diagram)

As we have mentioned, the d-q reference frame theory is a major aspect to this method of control. Therefore, the measured phase values must be converted into the two-phase d-q axis. To achieve this, we first take two phase currents ( $I_a$  and  $I_b$ ). We convert the signals through Clarke transformation to alpha-beta. Next, we perform park's transformation, which converts the alpha-beta currents to the desired dq currents. The transformed direct current  $I_d$  is compared with a reference  $I_d$  (flux reference). The  $I_d$  is set to a constant value. The transformed quadrature current

$I_q$  is compared with the  $I_q$  reference (torque reference). The torque reference can be calculated by a speed controller. There are two components (speed regulator and the maximum power limiter) as shown in Fig. 3.5. The first is the speed regulator. The velocity (angular in the case of rotary PMSM) of the machine is measured and compared with the reference. The reference velocity is a commanded user input. The output of the summer (compared value) is the error signal for the speed. The error signal goes through a PI regulator/controller as shown in Fig. 3.6. This regulator is popularly used in FOC as it regulates the torque and flux feedback well. The PI constants ( $K_{pi}$  and  $K_i$ ) should be chosen correctly to reach steady state [37]. The mathematical expression (control law) for the PI controller is given in equation 3.20, where ‘e’ is the error signal ( $e = \text{reference} - \text{feedback}$ ).

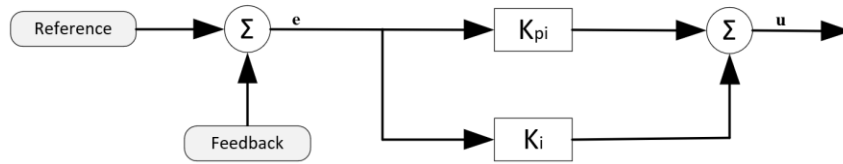


Fig. 3.6: Proportional - Integral block diagram

$$u = K_{pi} \cdot e + K_i \cdot e \quad (3.20)$$

The output of the PI block is then used in two blocks, the multiplexer, and the maximum power limiter. The error signal at the speed controller gets converted to a torque value, which is limited to the maximum torque ( $+T_{max}/T_b$  &  $-T_{max}/T_b$ ). This value is used to compare (through the comparator) with the maximum power. The maximum power is divided by the measured velocity to obtain the electromagnetic torque. The relationship for this is given in equation 3.21. The compared value is sent to the multiplexer.

$$P_{max} = T_{em} \cdot \omega_m \quad (3.21)$$

The multiplexer determines the correct output depending on the selector's signal. The truth table and block diagram are given in Fig. 3.7. There are two cases that is possible with this circuit as follows:

**Case 1:** The comparator will output a high signal if the output of the PI regulator is greater than the maximum power limiter. This means the output of the multiplexer would be the output of the power limiter.

**Case 2:** The comparator will output a low signal if the output of the PI regulator is smaller than the maximum power limiter. In this case the output of the multiplexer would be the output of the PI regulator. Otherwise, the torque value calculated at the maximum power limiter will be used. This in turn lets the lowest torque value to be passed through.

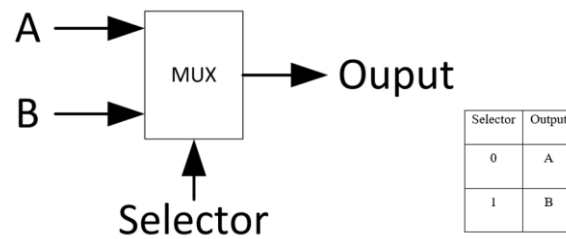


Fig. 3.7: Multiplexer blocks diagram & truth table

After the multiplexer, the signal goes through a gain block to transform the torque value into a current value. The mathematical relationship of  $K$  ( $1 / (K_{TA} * i_b / T_{pu})$ ) is given in equation 3.22. Here,  $I_s$  represents space vector stator current and  $k_T$  represents the torque constant. Finally, this current value is limited by  $\pm I_{qmax}$  which is given by equation 3.23. The output of the limiter is our  $I_q$  value.

$$I_s = \frac{T_{em}}{k_T} \tag{3.22}$$

$$I_q^* = \sqrt{\hat{I}_s^2 - |I_d|^2} \quad (3.23)$$

The next process of the field-oriented control method is the current control. The calculated reference  $I_q$  and the measured  $I_q$  values are compared through a summer. The difference is taken, and this value is the error signal of the quadrature current. The error signal is again placed into a PI block. This process is repeated for the direct current  $I_d$ . The output of the current regulators are the dq reference voltages. These voltages are transformed using inverse parks transformation to obtain the alpha beta reference voltages of the stator vector. The alpha beta voltages are in the stationary orthogonal reference frame, thus can be used in generation of pulse with modulation via the space vector PWM block. As mentioned in previous chapters, the switching pattern is generated by comparing the sinusoidal reference signal with the carrier wave.

### 3.5 Modeling of the Regenerative System

To model the regenerative system, we opted with a half bridge DC-DC bidirectional converter for a proof-of-concept model. This topology was studied in [47]. The buck-type bidirectional DC-DC converter is illustrated in Fig. 3.8. It consists of a lithium-ion battery, two IGBTs, an inductor and a capacitor. The bidirectional converter has two modes of operation buck mode and boost mode. The buck mode operates when the motor is in the regeneration mode. Boost mode operates when the motor is in generation mode. The bidirectional converter shown can be operated in buck mode by turning off the lower leg IGBT, this will leave just the diode D2. The upper leg IGBT will be switched via PWM. The new converter can then be modeled as shown in Fig. 3.9(a). For boost mode of operation, the upper leg IGBT is turned off (leaving diode D1) and the lower leg IGBT is switched via PWM.

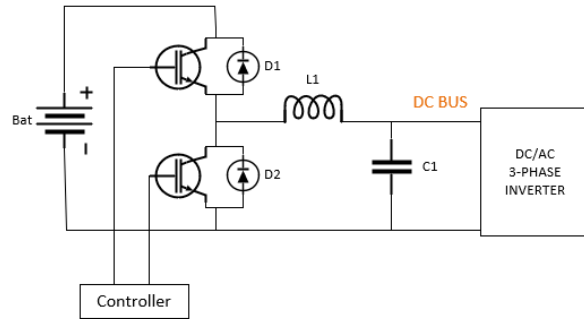


Fig. 3.8: Buck-type bidirectional DC-DC converter

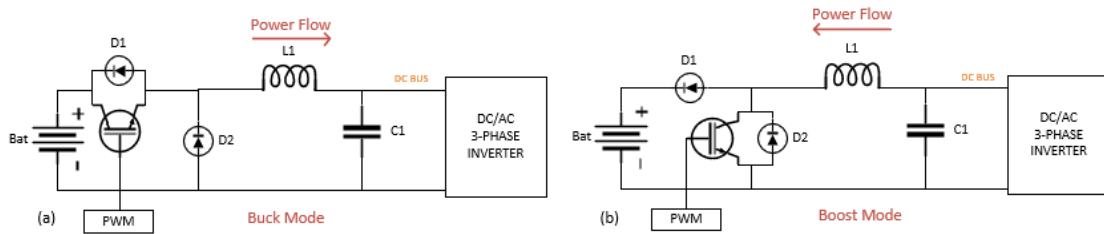


Fig. 3.9: Bidirectional DC-DC converter in (a) buck mode operation & (b) boost mode operation

Design equations for the buck converter are presented in equations 3.22 – 3.24. The duty cycle given in equation 3.22, can be determined by taking the ratio of the output voltage over the input voltage, or the input current over the output current. The inductor value can be calculated by using equation 3.23. The critical inductor value determines the point at which the converter works in continuous conduction mode (CCM). Depending on desired cost, size, and performance of the converter, the inductor value is equal to a multiple of the critical inductance. Finally, the capacitor value can be determined using equation 3.24 for a certain voltage ripple.

$$D = \frac{V_{out}}{V_{in}} = \frac{I_{in}}{I_{out}} \quad (3.22)$$

$$L_{crit} = \frac{(1 - D)}{2} TR \quad (3.23)$$

$$\frac{\Delta V_c}{V_{out}} = \frac{(1 - D)}{8LCf^2} \quad (3.24)$$

The equations used to design a boost converter is given in equation 3.25 - 3.27.

$$\frac{V_{out}}{V_{in}} = \frac{I_{in}}{I_{out}} = \frac{1}{1 - D} \quad (3.25)$$

$$L_{crit} = \frac{RT}{2} (1 - D)^2 D \quad (3.26)$$

$$\frac{\Delta V_{out}}{V_{out}} = \frac{D}{RCf} \quad (3.27)$$

Using digital logic, the function of the bidirectional converter can be controlled. In [51], the author presents a method to simulate a bidirectional DC-DC converter using charging, discharging and regenerative control blocks developed in PSIM. The block diagram shown in Fig. 3.10 represents the modeling of the controller for the Bi-Directional DC-DC system. The model works by first determining the state of the motor. As mentioned in chapter 2, if the LSM has a positive power (in terms of thrust and speed) then it is in motoring mode of operation, otherwise a

negative power indicates braking mode. Therefore, by determining the speed and thrust force of the motor the controller can determine if the converter should be in buck or boost mode of operation. An additional state the controller looks at, before determining the course of action for the converter, is the state of the battery. Thus, the charging mode of operation occurs when  $V_{\text{batt}} < V_{\text{float}}$  and the motor is in regenerative braking mode. This solution will be employed in chapter 4 of the thesis.

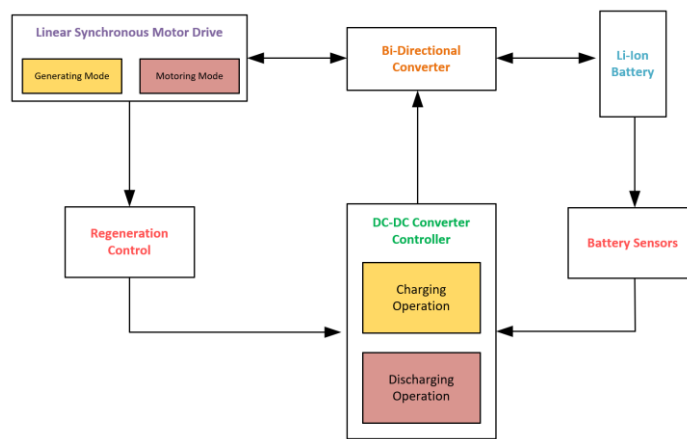


Fig. 3.10: Bi-Directional DC-DC controller based on [51]

The battery can be modeled in either an electrochemical, mathematical, or electrical model. Each has its advantages. However, to reduce complexity, the thesis implements equivalent circuit model (ECM) for the battery. The advantages of ECM also includes its robustness and simplicity to use with BMS systems [52], [53]. Fig. 3.11 illustrates the battery ECM, it includes the open circuit voltage source, which is the unloaded, equilibrium voltage of the battery cell. Additionally, the circuit model also includes an equivalent series resistance. The voltage source is represented by a dependant voltage-controlled voltage source (VCVS). This is because a completely charged battery cell will have a higher voltage, and as the battery discharges, the voltage decreases. The state of charge (SOC) of a battery cell is represented by a percentage between 0% - 100% [53].

The equivalent series resistance (ESR)  $R_{batt}$  is added to describe the dynamic behavior of the cells. More specifically, the battery cell's voltage drop is determined by the resistance. Thus,  $V_{batt}$  goes through a voltage drop when a load is present (i.e.  $V_{oc} > V_{batt}$  in loaded conditions).

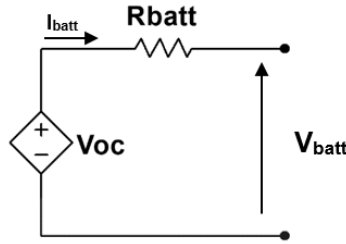


Fig. 3.11: Equivalent Circuit of a Battery

Equation 3.24 shows the ordinary differential equation of the state of charge. The total capacity is denoted as  $Q$  and  $i(t)$  is the load current measure in amperes. The charge efficiency is denoted as  $\eta$ , which is the charge out over the charge in ( $\eta = Q_{discharge}/Q_{charge}$ ).

$$SOC'(t) = -\eta(t) \frac{i(t)}{Q} \quad (3.24)$$

Furthermore, the equation describing the terminal voltage drop is given in equation 3.25.

$$v(t) = V_{oc}(Soc(t)) - i(t)R_{batt} \quad (3.25)$$

When working in the digital domain we can do some integration and manipulation to convert it to the discrete – time model as opposed to the continuous model previously presented [53]. The discrete time equations for the battery model is given in equation 3.26 and 3.27. Based on the first equation, the open circuit voltage is a function of the SOC. The second equation says that the terminal voltage is greater than the open circuit voltage when the current is less than zero, this is when the battery is charging. In discharging mode, the current is greater than zero, thus, the terminal voltage  $V_{batt}$  is less than the open circuit voltage.

$$SOC[k + 1] = SOC(k) - \frac{\Delta t}{Q} \eta[k] i[k] \quad (3.26)$$

$$v[k] = V_{oc}(SOC[k]) - i[k]R_0 \quad (3.27)$$

In chapter 4 a simulation model for the battery system will be presented using PSIM's library for simulating the lithium-ion battery. The block diagram for this model can be seen in Fig. 3.12., which revolves around the model presented.

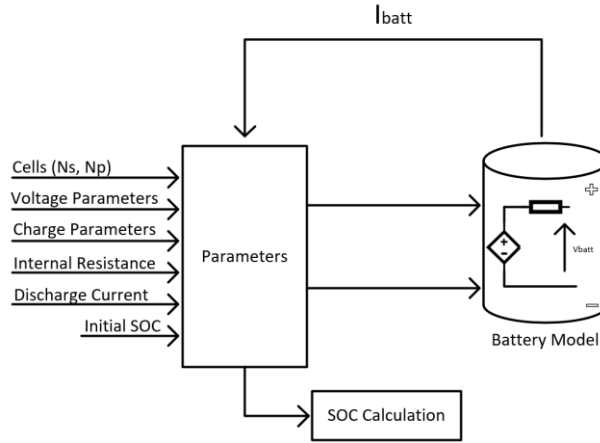


Fig. 3.12: Block diagram for lithium ion battery model, adapted from [54]

Parameters of the battery model can be calculated using equation 3.24 – 3.26.  $K_s$  and  $K_p$  are the voltage and capacity derating factors, respectively.  $N_s$  and  $N_p$  are the number of cells in series and number of cells in parallel for the battery pack.

$$E_{rated\_total} = N_s \cdot K_s \cdot E_{rated} \quad (3.24)$$

$$Q_{rated\_total} = N_p \cdot K_p \cdot Q_{rated} \quad (3.25)$$

$$R_{battery\_total} = \frac{N_s}{N_p} \cdot R_{battery} \quad (3.26)$$

For initial simulation parameters it can be assumed that the DC bus voltage is 500 V and a charge of 65 Ah. A starting point can be made for modeling the battery using these initial simulation estimates for the battery pack. By referencing the datasheet of the chosen battery cell, the rated

specifications can be obtained. For example, from Panasonic's 18650 lithium-Ion battery cell (NCR18650GA) datasheet the rated voltage of a cell is 3.6V with a capacity of 3300mAh. Therefore, using equation 3.24 and 3.25, an estimate of the number of cells can be made. The number of series cell to meet the initial simulation conditions would be  $N_s = 139$  cells and for the parallel connections,  $N_p = 20$  cells. However, the number of series cell can be reduced by reducing the output voltage and using a boost converter to obtain the desired output. Therefore, using an arbitrary voltage of 250 V, we can redesign the battery pack. This would give us  $N_s = 70$  cells and  $N_p = 20$  cells (since the capacity is not changing).

## Chapter 4. Design Simulation in PSIM

To implement the propulsion system, PSIM software was used. The design was first implemented using a template provided by PSIM for electric vehicles traction motors. This template was used as a starting point and edited to suit the appropriate application.

### 4.1 Simulation of the Three – Phase Inverter

The three-phase inverter is one of the main components for the drive system. Therefore, the first aspect to designing the traction motor is the inverter. Using IGBT blocks from the PSIM library, the two-level topology can be realized. The topology created in PSIM can be seen in Fig. 4.1. The switching signals are generated based on sinusoidal pulse width modulation theory. Three AC voltage sources were used each with 0.8 peak amplitude shifted by 120 degrees. The frequency for the reference AC signals were set to 60 Hz. These signals are compared with a triangular wave voltage source. The switching frequency was set to 10 kHz with approximately double the amplitude of the reference source. The resulting waveforms are shown in Fig. 4.2.

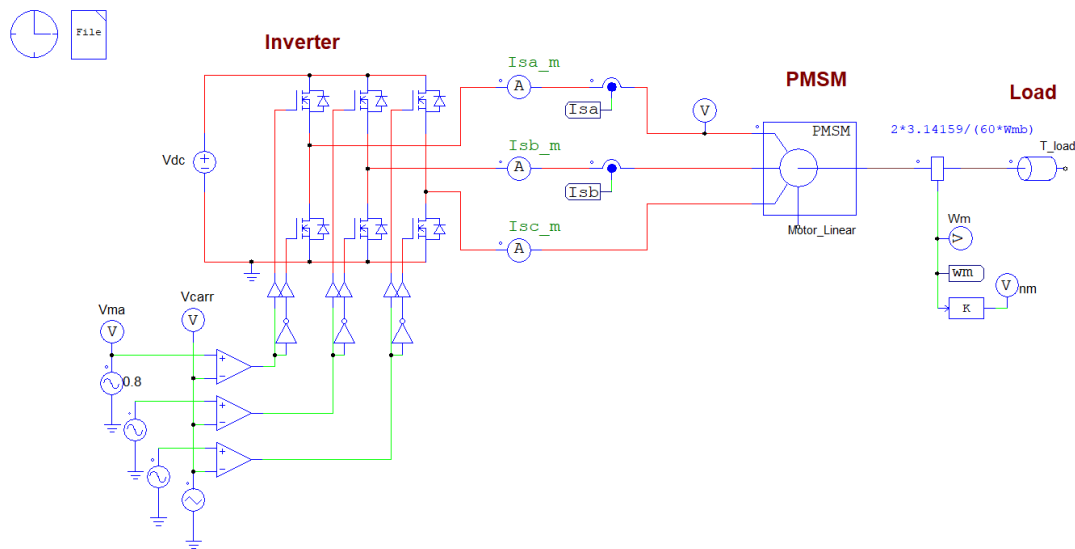


Fig. 4.1: Three Phase Inverter SPWM

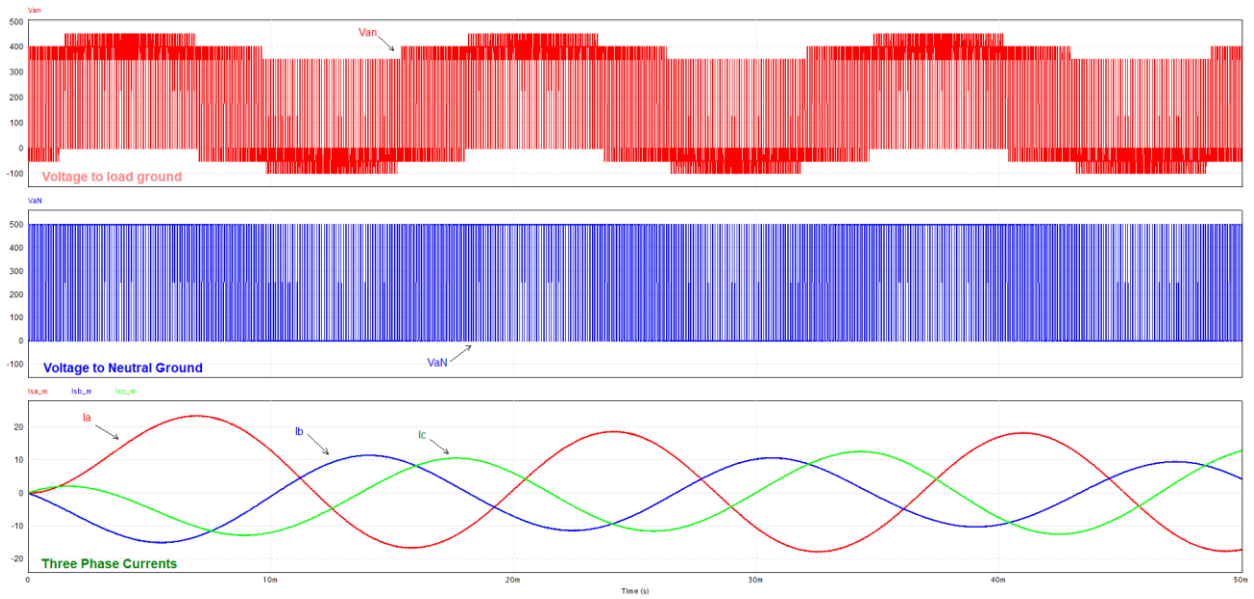


Fig. 4.2: Three Phase Inverter Waveforms

Using PSIM's SVPWM implementation, the simulated schematic was updated as shown in Fig. 4.3. The modulation schemes have different reference waveforms which is illustrated in Fig. 4.4.

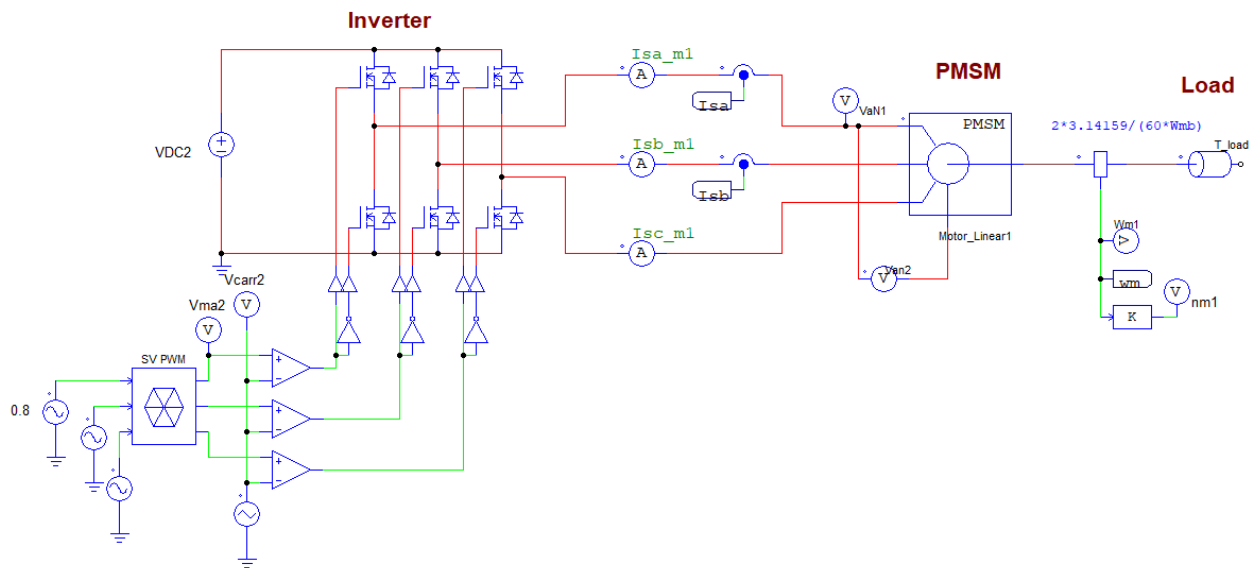


Fig. 4.3: Three Phase Inverter SVPWM

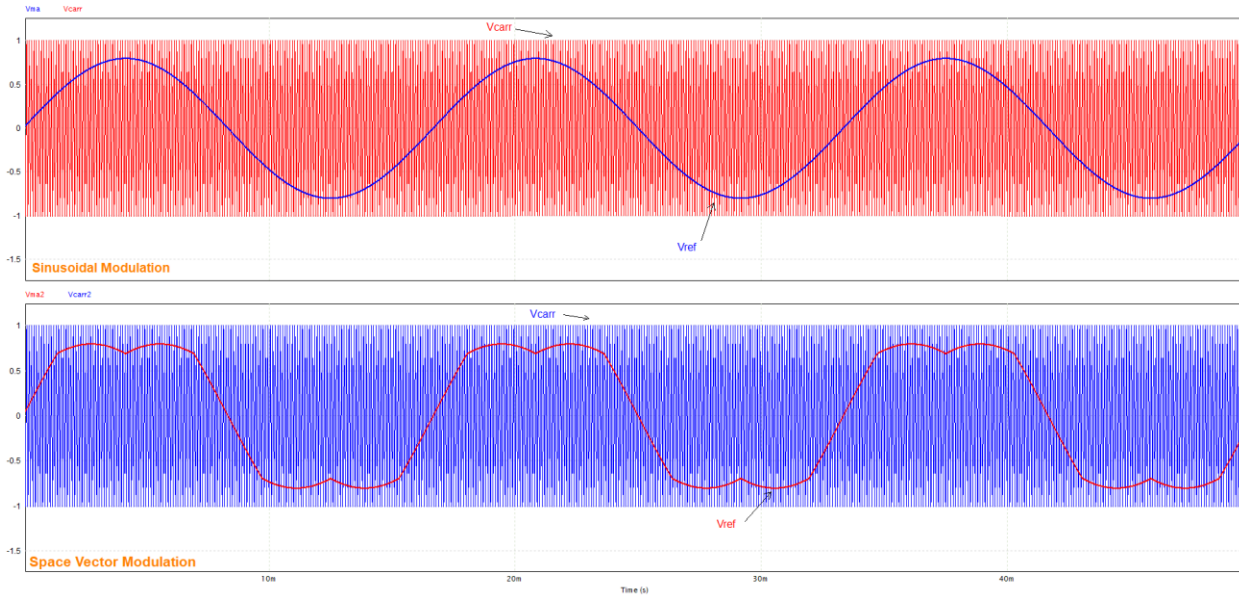


Fig. 4.4: SPWM and SVPWM Modulation Scheme Waveforms

## 4.2 Simulation of the Motor Control and Drive System

### 4.2.1 Open Loop Controller Design

The first step of implementing the drive system for the motor is simulating the proposed field-oriented control model from chapter 3.4 in open loop conditions. This portion follows steps provided in [55]. Fig. 4.4 shows the setup done in PSIM. The motor and load parameters were given arbitrary values to first implement a working proof of concept controller. It includes a DC bus voltage, 6 IGBTs, a PM synchronous motor and the commanded control signals  $I_d$  and  $I_q$ . The waveforms for this circuit setup are given in Fig. 4.5. The three phase currents are shown in the first graph.  $I_d$  and  $I_q$  currents are shown in the second graph, the waveforms show that it reaches steady state. This can also be seen in the last graph for the velocity  $\omega_m$ .

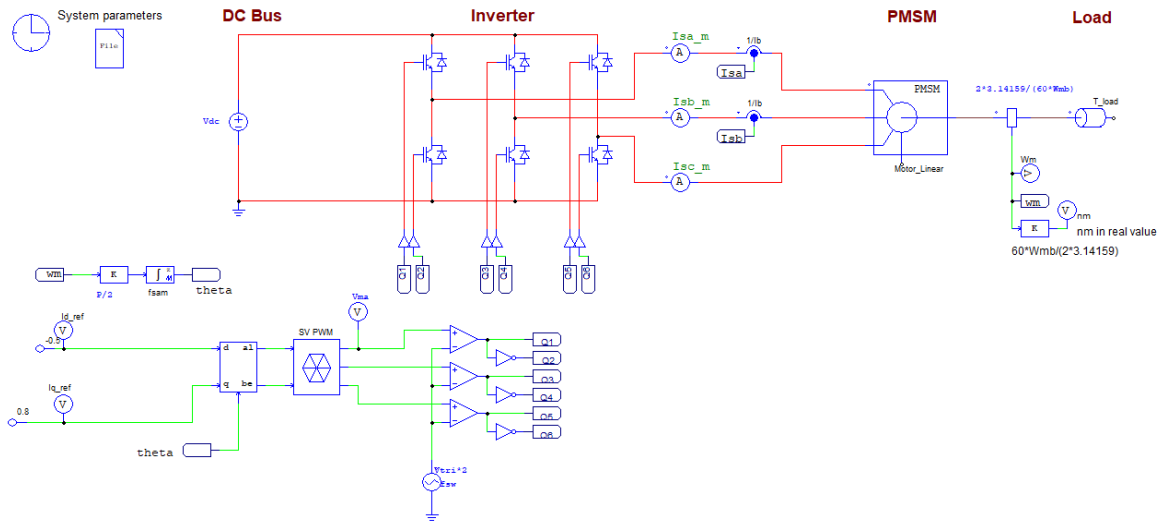


Fig. 4.5: Open loop PSIM setup of drive system

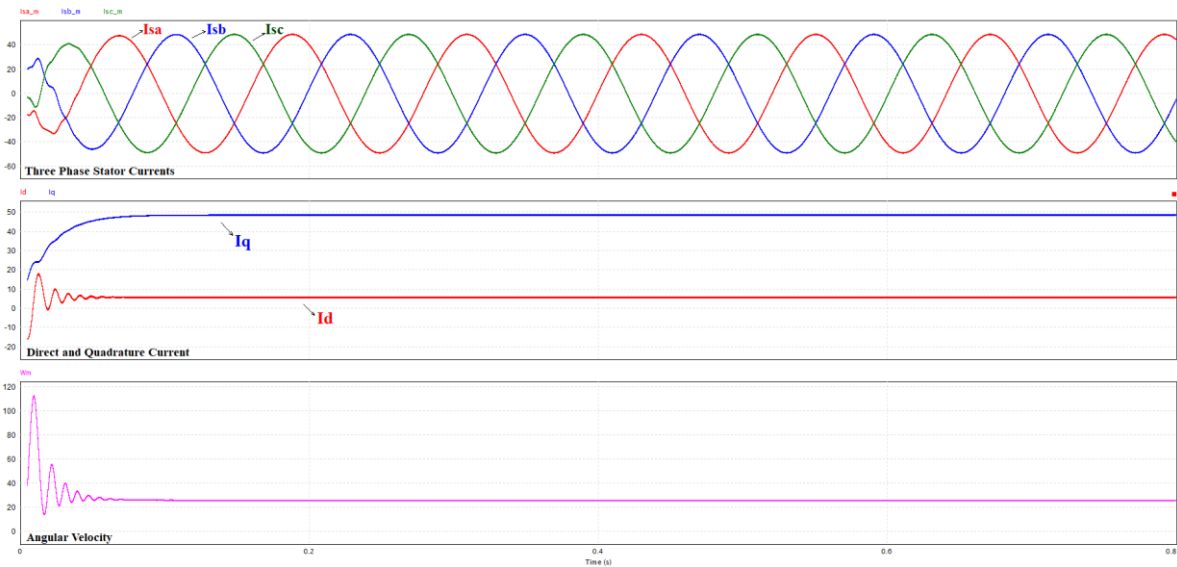


Fig. 4.6: Open loop Simulation Results

#### 4.2.2 Current Controller Design

To design the controllers for the closed loop system for the inner current controllers, we can obtain the PI parameters by analyzing the frequency response of perturbed  $I_d$  and  $I_q$ . Fig. 4.6 shows the waveforms generated after perturbing  $I_q$  at incremented frequencies.

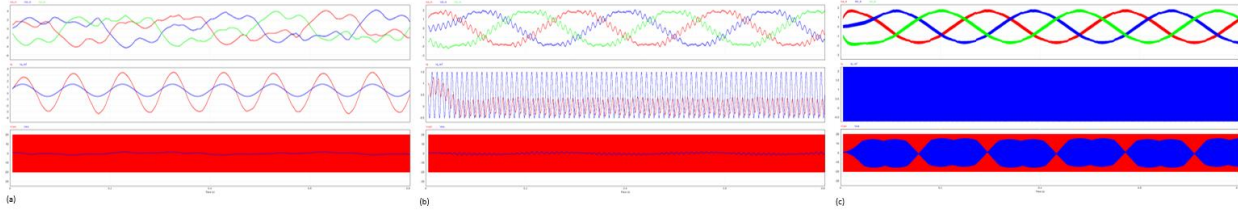


Fig. 4.7: Perturbation in  $I_q$  at (a) 1 V, 10 Hz (b) 1 V, 100 Hz (c) 15 V, 3 kHz

The results of this perturbation look as expected. Fig. 4.7 (a) had  $I_q$  perturbed at 1 V, 10 Hz. The current waveforms are distorted. We can see that the quadrature current follows the oscillation well. Additionally, we can see that our modulation index is staying in the envelop of the carrier wave. As the frequency increases, we can see that the response of the  $I_q$  lowers. At 3kHz the perturbation is harder to observe as we are increasing the frequency. This required a change in the amplitude to 15 volts to obtain observable data.

Now that the parameters are set and we can observe that the waveform during perturbation is as expected, we can perform the AC sweep. Table 4.1 shows the parameters for the AC sweep block in PSIM. The frequency response of the AC sweep is given in Fig. 4.8.

Table 4.1. AC sweep parameters

Parameters	Value
Start Frequency	10 Hz
End Frequency	3 kHz
No. of Points	51 Points
Start Amplitude	1 V
End Amplitude	15 V

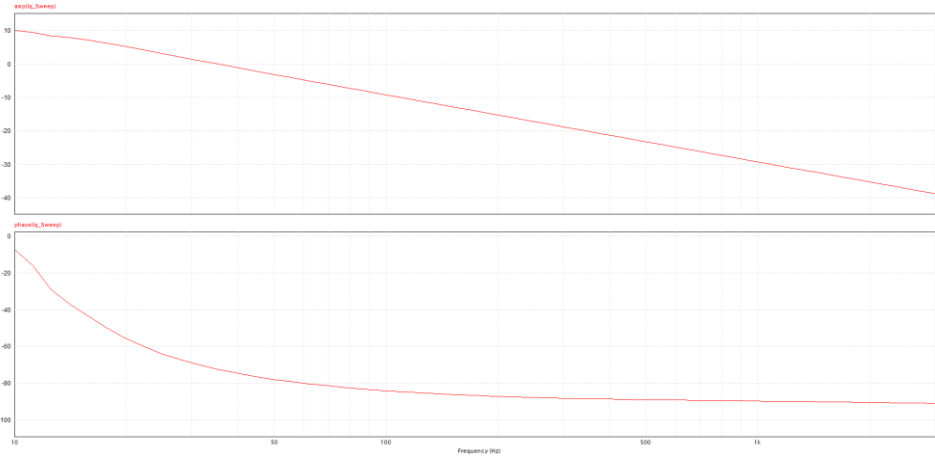


Fig. 4.8:  $I_q$  Frequency Response (AC Sweep)

A similar process in observing the perturbed waveforms for  $I_d$  was performed. The results were as expected, this can be seen in Fig. 4.9. Proceeding to the AC sweep of the direct current  $I_d$ , the resulting waveforms are given in Fig. 4.10.

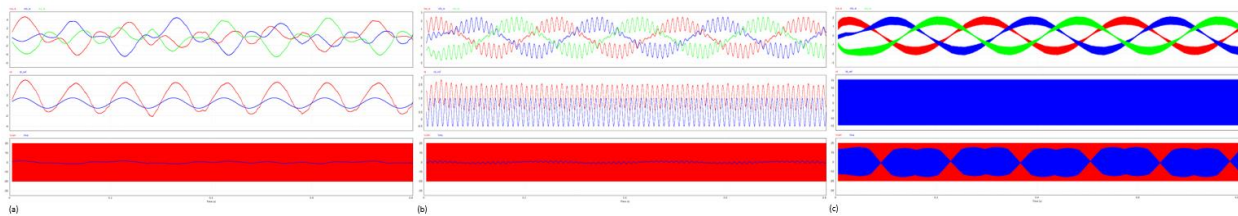


Fig. 4.9: Perturbation in  $I_d$  at (a) 1 V, 10 Hz (b) 1 V, 100 Hz (c) 15 V, 3 kHz

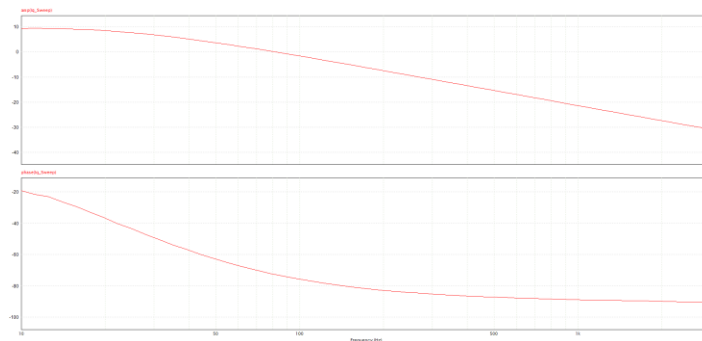


Fig. 4.10:  $I_d$  Frequency Response (AC Sweep)

Using the frequency responses generated by the AC sweep, we can input it into SmartCtrl and obtain the PI values. This can be done easily with SmartCtrl's stable solution space/map. The solution space is generated based on the plant, sensor, and type of regulator the user sets. SmartCtrl then provides a map of stable region in a phase margin vs crossover frequency chart. Fig. 4.11 shows the controller designer in SmartCtrl. It includes the bode plots, polar plot, and the step response. The bode plots have two lines, the pink one is the control to output response and the green line is the open loop response. Using the Solution map control, we can pick between the phase margin and the cross frequency that provides a minimal overshoot and settles at an acceptable rate in the step response. After tuning the point in the solution map control to the desired step response, we can take the values of  $K_p$  and  $T_i(s)$  for the PI controller for  $I_q$ . This process was repeated for  $I_d$ .

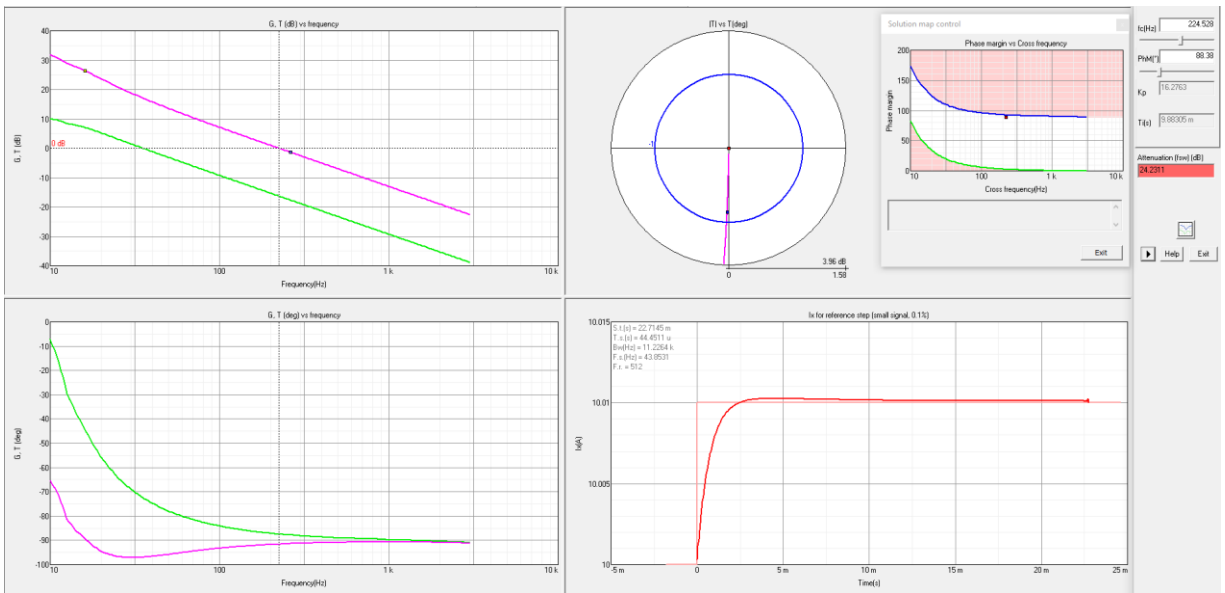


Fig. 4.11: PI designer in SmartCtrl for  $I_q$  frequency response

Table 4.2. Controller Parameters

Current Loop	Parameter	Value
$I_q$	$K_i$	16.2763
	$T_i(s)$	9.88305 [ms]
$I_d$	$K_i$	6.6574
	$T_i(s)$	4.6395 [ms]

These parameters were placed into the PI controllers for the inner control loops. The control algorithm is shown in Fig. 4.12. The control circuit in Fig. 4.8 shows the newly added PI controllers for the  $I_q$  and  $I_d$ . A perturbation was added into the  $I_q$  reference signal. The generated waveforms are also shown in Fig. 4.12.

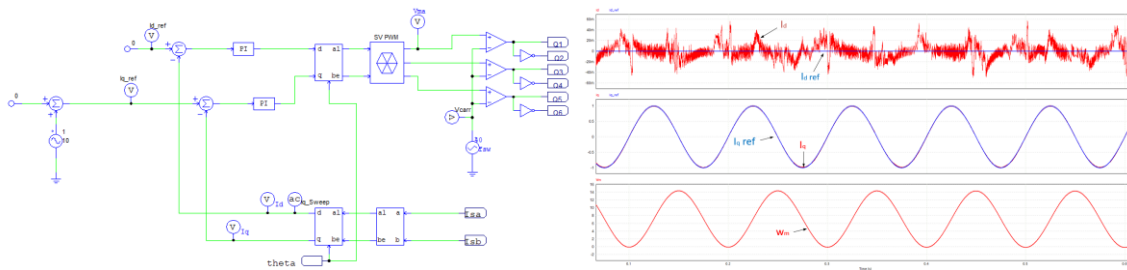


Fig. 4.12: Inner PI controller schematic and generated waveforms

We can see from the first graph that the  $I_d$  reference is having a hard time to stabilize to zero. However, the peak-to-peak amplitudes are minimal. The next graph shows the  $I_q$  and  $I_q$  reference signals. We can see the  $I_q$  oscillating due to the perturbation and is following the reference well. The last graph shows the speed which is also oscillating as expected.

#### 4.2.3 Speed Controller Design

The next part of field-oriented control design is implementing the speed control. As mentioned in the earlier chapters we can control the speed by varying the reference  $I_q$  signal. Therefore, to

implement the speed controller we can perform an AC sweep on  $I_q$ . Additional waveforms to verify performance at higher perturbed frequencies are given in Fig. 4.13.

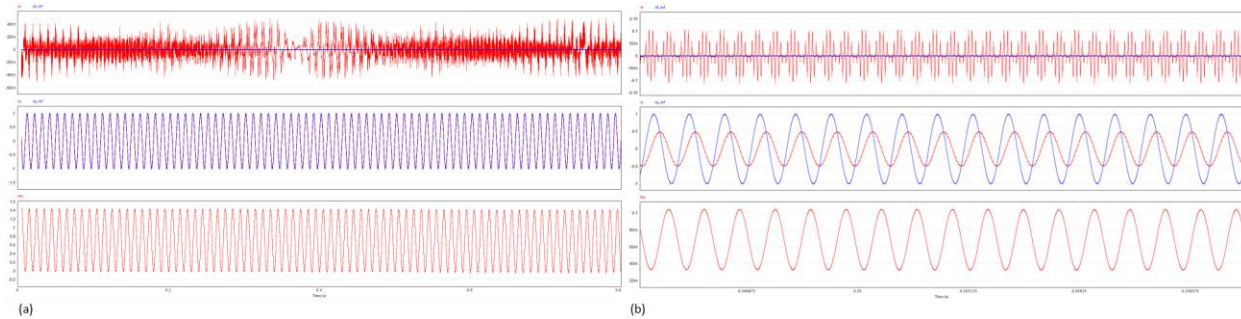


Fig. 4.13: Perturbation in  $I_q$  at (a) 1 V, 100 Hz (b) 1 V, 1 kHz

We can observe slight phase shifting in the second graph between the reference and actual  $I_q$  values as the perturbation frequency increases. The waveforms are as expected, and we can move on to the AC sweep. The AC sweep waveforms are imported in SmartCtrl shown in Fig. 4.14. After adjusting the phase margin and cross frequency we choose a point that will give a good gain. The value for the proportional gain was 1.50362, and a time constant of 846.761 ms.

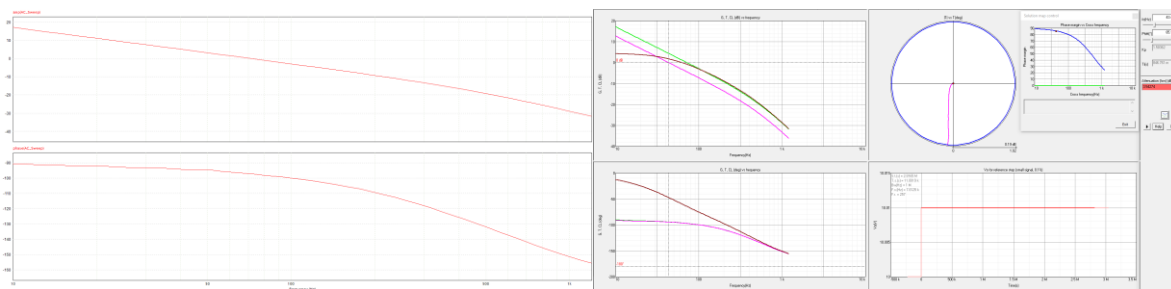


Fig. 4.14:  $\omega_m$  frequency response (AC Sweep) and PI designer in SmartCtrl for  $\omega_m$  frequency response

The waveforms were then generated after implementing a speed controller using the PI values from SmartCtrl. Fig. 4.15 shows the waveforms for the three phase currents, direct current, quadrature current and finally the measured velocity in RPM. It is important to note that the

simulation ran in unloaded conditions. The first waveform shows the three phase currents and as we can see at transient, we have a peak current of 10 amps AC. The next waveform shows the measured  $I_d$  and the reference  $I_d$  (which was set to zero). The third waveform shows the reference  $I_q$  (set by the speed controller). We can see that the  $I_q$  follows the reference well. The velocity is given in the fourth waveform. We can see it reaches steady state in less than 0.2 seconds. Finally, a torque of 5 Nm was added to observe the waveforms in full load conditions as shown in Fig. 4.16.

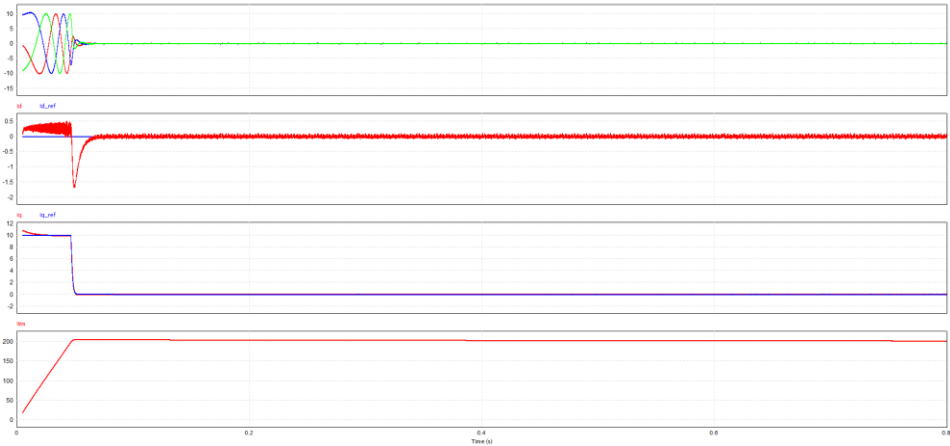


Fig. 4.15: Waveforms after adding the speed controller (no load)

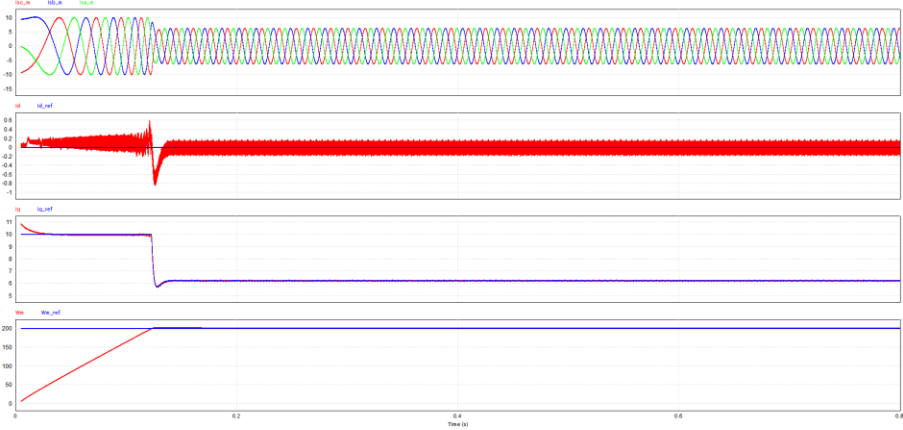


Fig. 4.16: Waveforms after adding the speed controller (full load)

### 4.3 Simulation of the Battery and Regenerative System

#### 4.3.1 Simulation of the Lithium-Ion Battery

To simulate the lithium-ion battery model, PSIM's implementation is used. The model follows similar equations presented in chapter 3 of this thesis. To model the battery, the simulation uses Panasonic's line of 18650 lithium-ion battery cell (NCR18650B). The specifications are filled out in table 4-2. These specifications were obtained through the datasheet, estimations based on other batteries with similar properties and obtaining values from the discharge curve of the battery. PSIM's curve capture functionality was used to extract key points from the discharge curve provided in the manufacturer datasheet. Fig. 4.17 shows two extracted C - rates that will be used in the model and the charge curves.

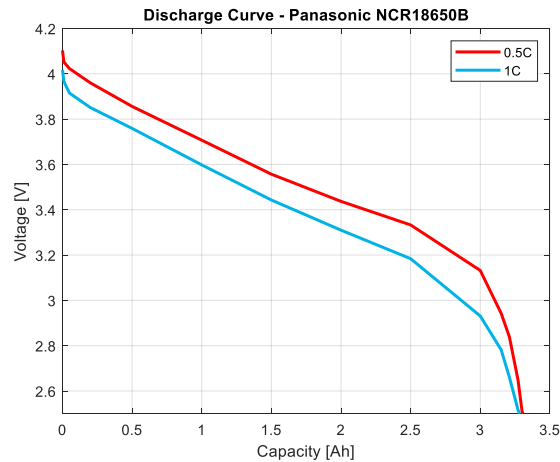


Fig. 4.17: Extracted curves from NCR18650B datasheet

The number of cells in series and parallel were calculated using equations presented in chapter 3.5. A 70s60p cell configuration will output 50 kW at 252 V. The gathered information from the datasheet can now be used to generate the lookup table for the battery model. The lookup table battery model requires three inputs. The open circuit voltage vs. state of charge and the two internal resistances vs. the state of charge curves for both charging and discharging.

Table 4.3. Specification of Battery Model in PSIM based on Panasonic - NCR18650B

Parameters	Value	Units
$N_s$ - No. of cells in series	70	cells
$N_p$ - No. of cells in parallel	60	cells
$E_{rated}$ - Rated voltage	3.6	V
$E_{cut}$ - Discharge cut-off voltage	2.5	V
$Q_{rated}$ - Rated capacity	3.35	Ah

To generate the lookup tables, first, the PSIM provided example schematic in Fig. 4.18 was used. This schematic generates the open circuit voltage with respect to the state of charge. Additionally, the same circuit is used to obtain the internal resistance curves for discharging case.

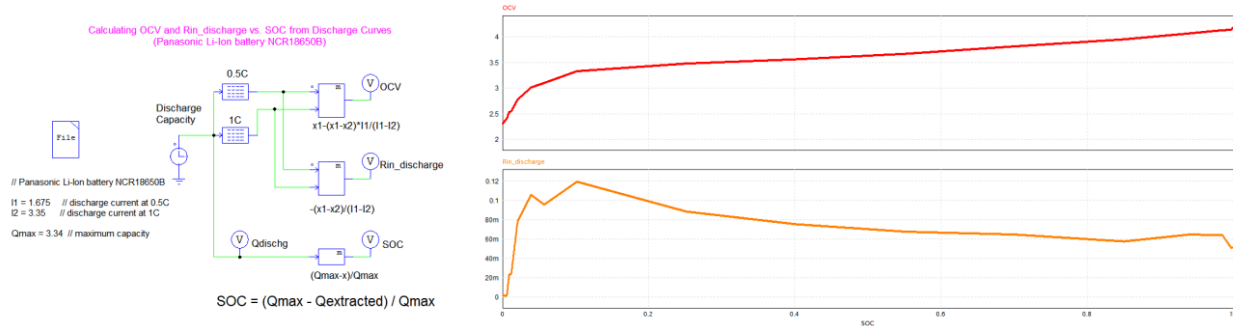


Fig. 4.18: OCV and Rin vs. SOC discharge curves for the NCR18650B

To generate the charging resistance vs. SOC table, the schematic in Fig. 4.19, provided by PSIM was used. The extracted datasheet curves are provided in Fig. 4.20.

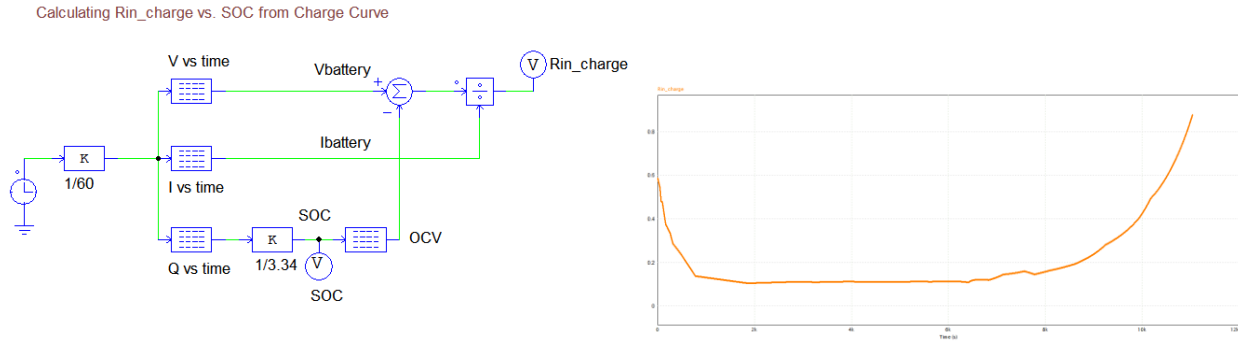


Fig. 4.19: Rin vs. SOC charge circuit setup and output curve for the NCR18650B

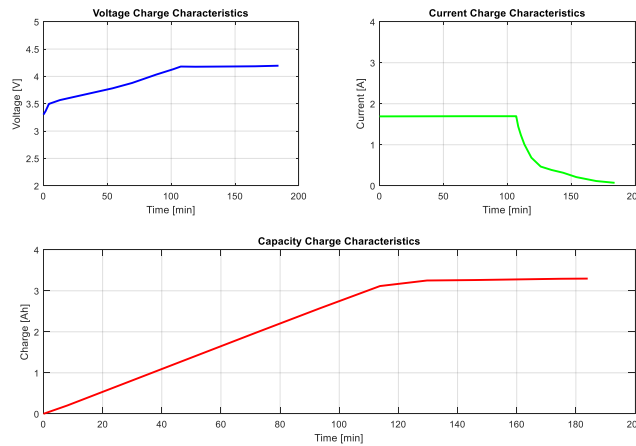


Fig. 4.20: Charge Characteristics for the NCR18650B

After setting the initial settings, the battery parameters were fine tuned using charging and discharging tests described in [54] and observing the characteristics. Fig. 4.21 shows the discharging test bed of the battery model. The setup includes the battery, which is modeled using the parameters in table 4-2 (for one cell), probes to measure the state of charge, battery voltage, battery current and the capacity amp-hour (which is simulated using  $Q = I_{\text{discharge}} \cdot t_{\text{hours}}$ ). The simulation results for the discharging test are also given in Fig. 4.21. Lastly, the testing for the charging circuit was simulated as in Fig. 4.22. In conclusion, the model is working as intended. The discharge and charge curves match closely to the one described in the datasheet. Additionally,

the charge test simulation in Fig. 4.14d shows that at 0.5C it takes around 3 hours to reach 100% state of charge. Moreover, the constant current and constant voltage charging region can be easily seen. This model can now be used in the overall simulation for the Hyperloop.

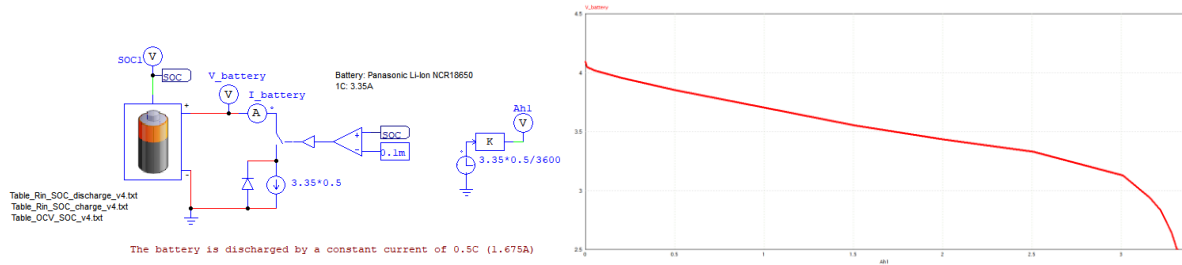


Fig. 4.21: Discharge Test for NCR18650B Model

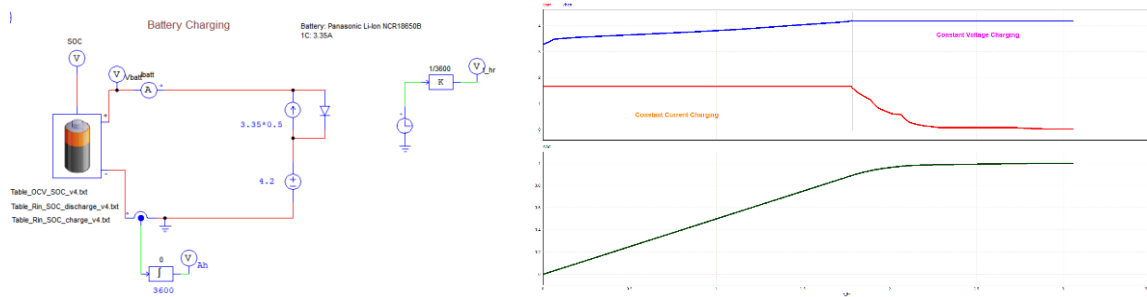


Fig. 4.22: Charge Test for NCR18650B Model

### 4.3.2 Simulation of the DC-DC Converter

The design of the initial DC-DC converter can be first separated by mode of operation. First the buck converter specification can be realized from table 4.3. These are the initial values that will be used for proof of concept before using larger ratings. A value of 3% for the output voltage ripple was chosen to meet the ripple specification as per IEEE 1662-2016 standard [56].

Table 4.4. Specification of DC-DC Buck Converter

Parameters	Value	Units
Input Voltage ( $V_{batt}$ )	500	V
Output Voltage ( $V_{DC}$ )	252	V
Switching Frequency ( $f_s$ )	50	kHz
Voltage Ripple ( $\Delta V_c / V_o$ )	3	%
Inductor Current Ripple ( $\Delta I_l / I_o$ )	5	%
Maximum Power ( $P_{max}$ )	40	kW

Using the parameters in table 4.3, the duty cycle, inductor value and the capacitor value can be determined.

### 4.3.2.1 Buck Converter Design

Fig. 4.23 shows the circuit configuration of the buck converter in PSIM. The controller is working in open loop by taking the reference duty cycle and carrier wave as the input to the comparator. This generates the switching pattern for the IGBT of the converter.

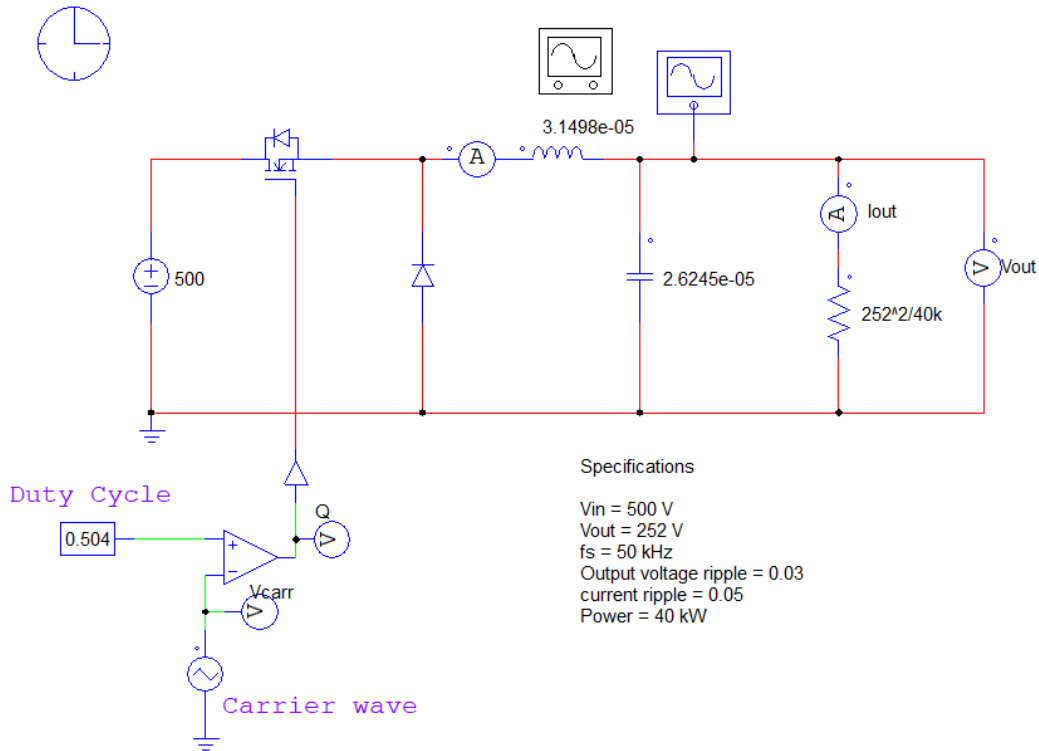


Fig. 4.23: Circuit Schematic of the Buck Converter

The waveforms generated by the buck converter is given in Fig. 4.24(a). The output voltage at steady state is approximately 250 V. The ripple effects for the inductor current and the output voltage can be seen in Fig. 4.24(b). It can be observed that the values are as specified of 3% for the voltage and 5% for the current.

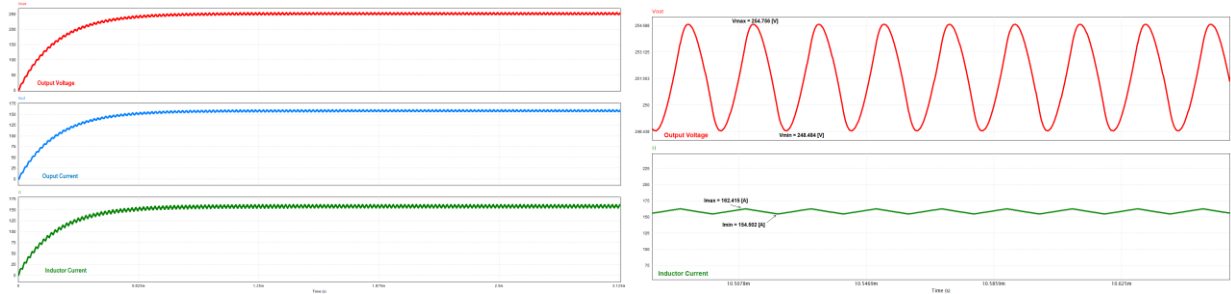


Fig. 4.24: (a) Open loop simulation of buck converter and (b) output ripple voltage and inductor ripple current

To implement a closed loop control scheme for the buck converter we will follow a similar process to the one in chapter 4.2. The first step is to design the inner controller loop. Once again, we begin by introducing a perturbation to our reference signal. The response of the converter due to an arbitrary perturbation is shown in Fig. 4.25. An AC sweep can be performed to obtain the response at a range of frequency. The output response is given in Fig. 4.26.

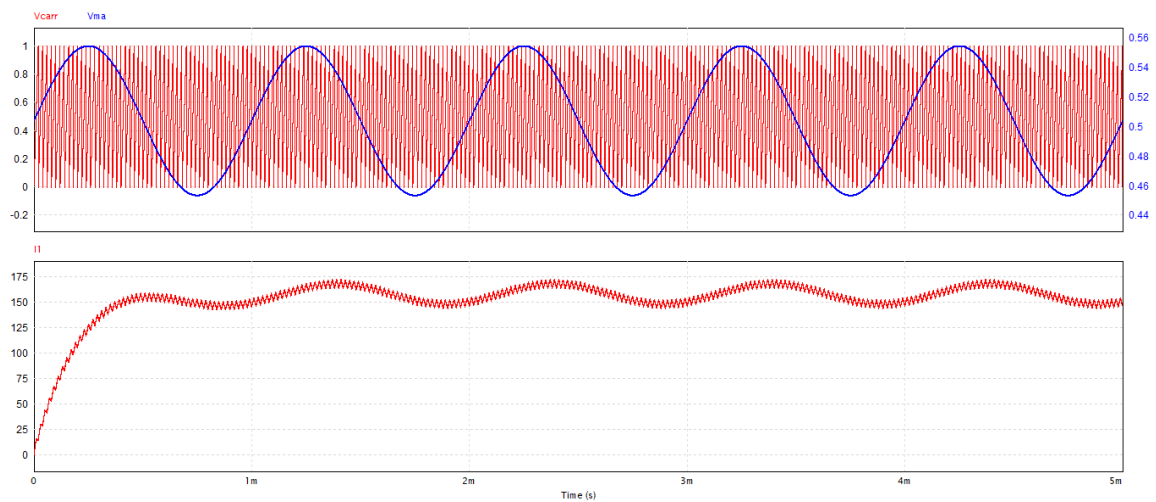


Fig. 4.25: Output response of buck converter under 10% of reference and 1 kHz perturbation

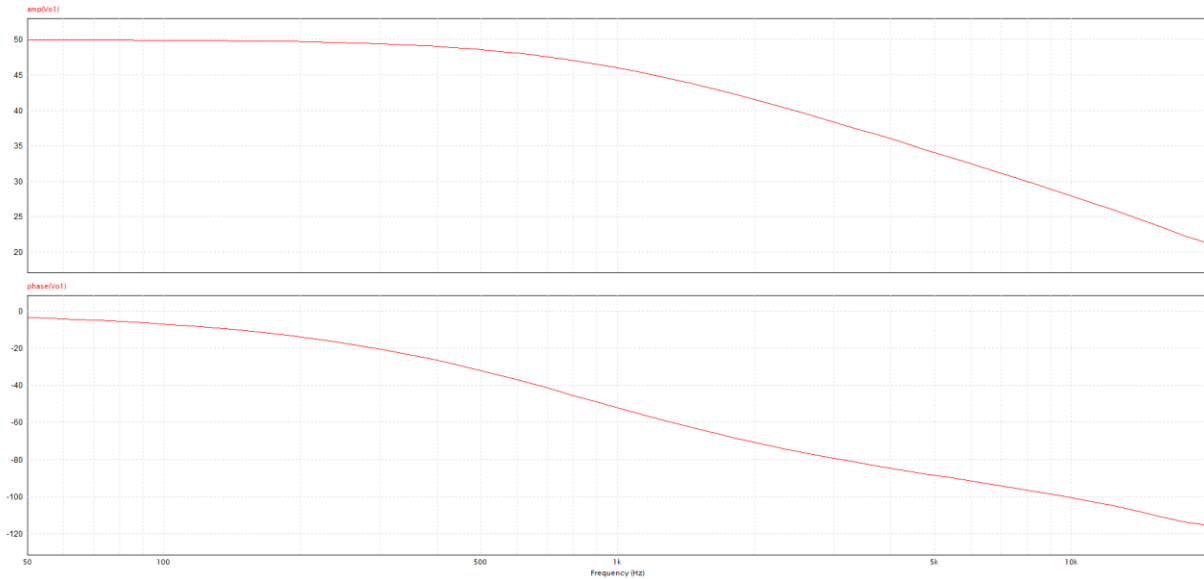


Fig. 4.26: AC sweep frequency response of inner current loop of buck converter

The frequency response can then be imported into SmartCtrl. A set point of 158 A (average inductor current) was chosen for the current set point and a switching frequency of 50 kHz. The results of the PI tuning in SmartCtrl are shown in Fig. 4.27. The new circuit with the inner PI controller is illustrated in Fig. 4.28(a). The reference is set as 1 with a gain of  $1/158$ , where 158 A is the desired average current across the inductor. The simulation results in Fig. 4.28(b) shows that the average current reaches the desired value at steady state. This process was then repeated for the outer voltage loop. Fig. 4.29 shows the resulting waveforms. The design goals are now met through the closed loop voltage and current control.

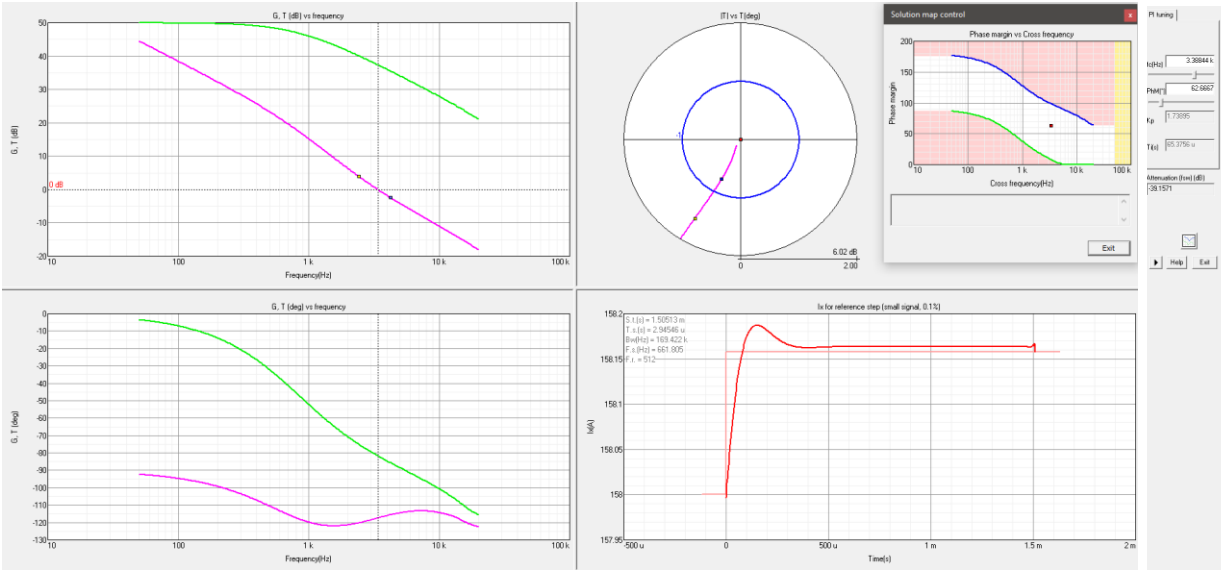


Fig. 4.27: SmartCtrl PI – Tuner for the buck converter

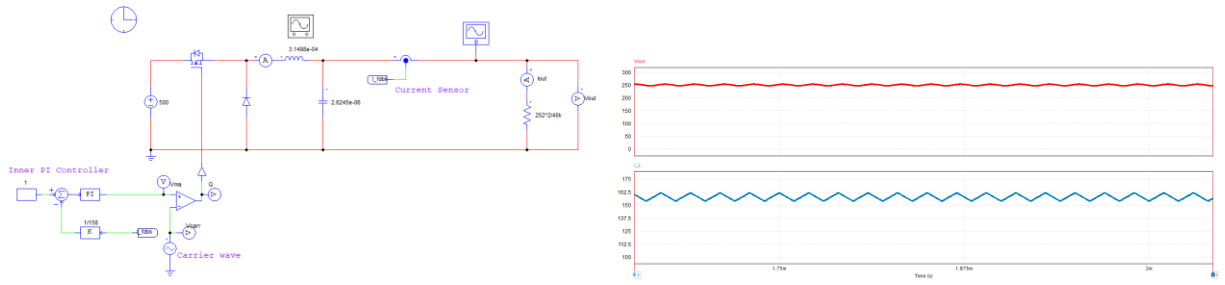


Fig. 4.28: (a) Inner current control closed loop simulation setup and (b) simulation results

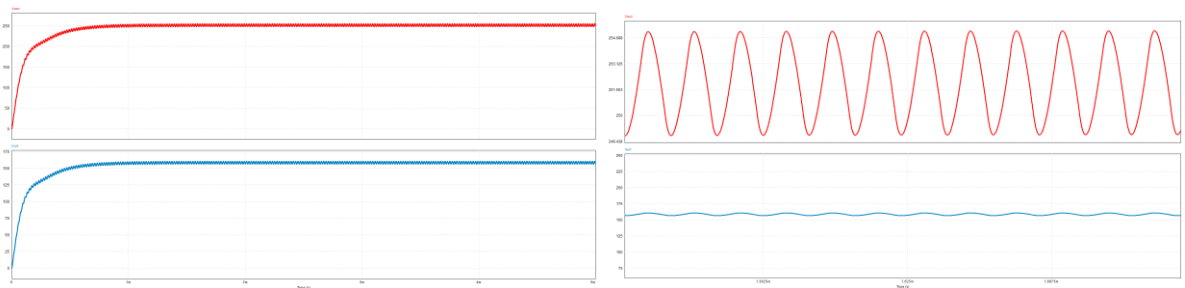


Fig. 4.29: (a) Vout and IL waveforms after adding voltage loop (b) Steady state waveforms

### 4.3.2.2 Boost Converter Design

The steady state parameters of the boost converter can be designed in a similar fashion to the buck converter. The open loop simulation is shown in Fig. 4.30. Here the calculated parameter for the duty cycle is 0.496. An inductance of 315  $\mu\text{H}$  and a capacitance of 53  $\mu\text{F}$  was chosen by design.

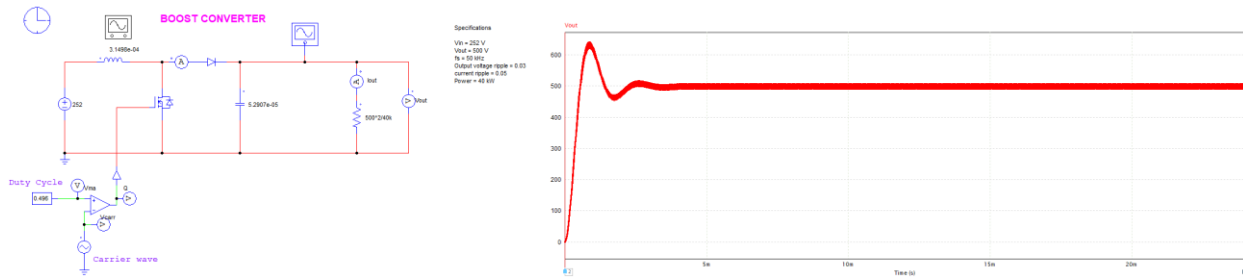


Fig. 4.30: Open Loop Design of Boost Converter

Once again, current mode control was used to close the loop. The regulator values were calculated by observing the response in SmartCtrl using the solution map tool. The circuit setup and simulation are provided in Fig. 4.31. The voltage shown in the red graph is reaching the desired 500 V at 80 A. The last graph in green shows the inductor current.

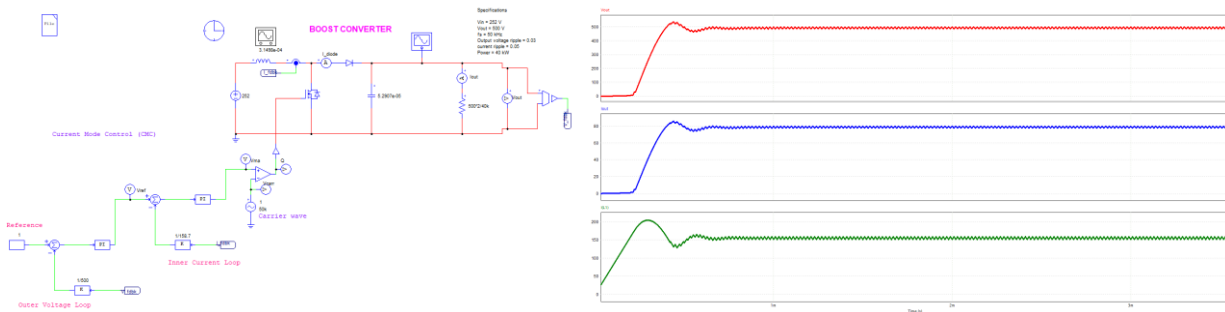


Fig. 4.31: Closed Loop Design of Boost Converter

A closer look into the steady state response is given in Fig. 4.32. Additionally, the diode current is shown in orange. The converter is meeting the the designed ripple specification of 5% and 3% for the inductor current and output voltage, respectively.

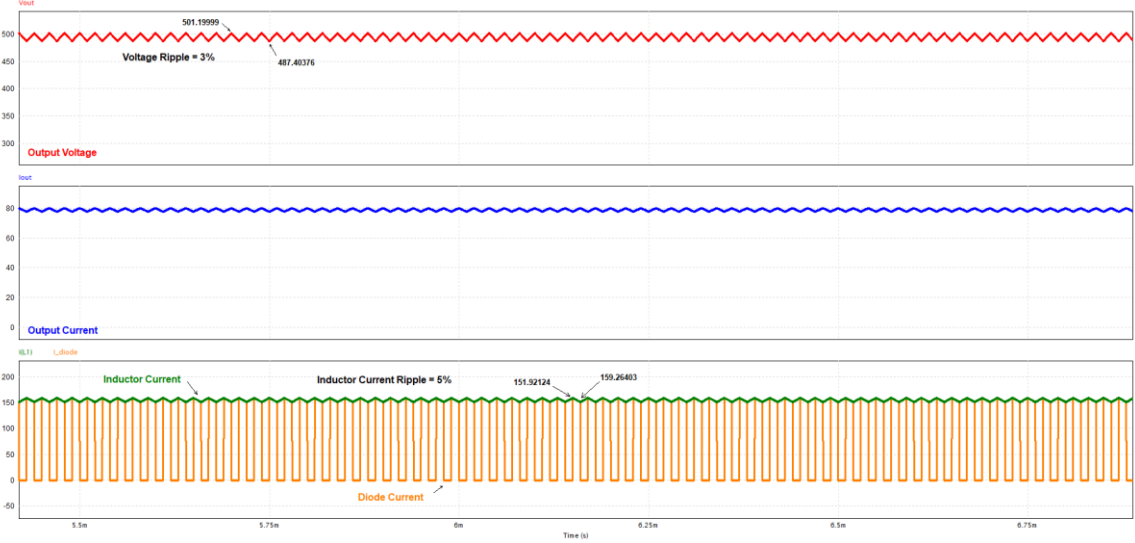


Fig. 4.32: Steady state waveforms for the boost converter

### 4.3.2.3 Bi-directional Converter Design

The bi-directional converter is designed using PSIM's permanent magnet motor charging and discharging control blocks. The control parameters are set to values obtained in the previous sub-chapter. Fig. 4.33 in the PSIM model for the bi-directional DC-DC converter.

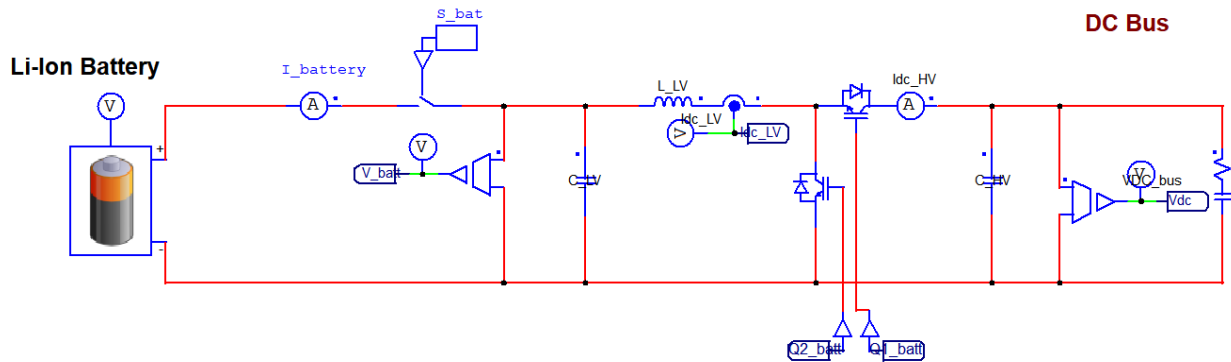


Fig. 4.33: PSIM Model for the Bi-Directional DC-DC Converter

The switches here are ideal IGBT switches which are driven by the signals Q1 and Q2. The control algorithm is implemented using the voltage and current control loops designed in the previous sub section. Additionally, the PSIM charging block works by using constant current - constant voltage charging. The discharge block works through either constant voltage or constant current. In the constant voltage mode, the voltage loop generates the reference for the current loop. Here, the voltage in the DC bus is constant. In current mode the block keeps the current flowing such that the maximum current can be produced for the DC bus. The blocks from PSIM library are shown in Fig. 4.34.

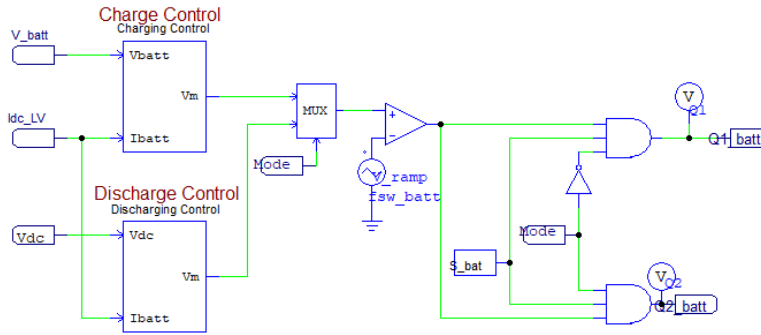


Fig. 4.34: Charging and Discharge Control for the DC-DC Converter

#### 4.4 Full Integration and Results

The full integration of all the components used is shown in Fig. 4.35. As shown, the power side consists of the lithium-ion battery module, bi-directional DC-DC converter, three phase inverter and the permanent magnet synchronous motor. The control side includes the field-oriented control blocks along with PSIM's charge/discharge algorithms for the DC/DC converter.

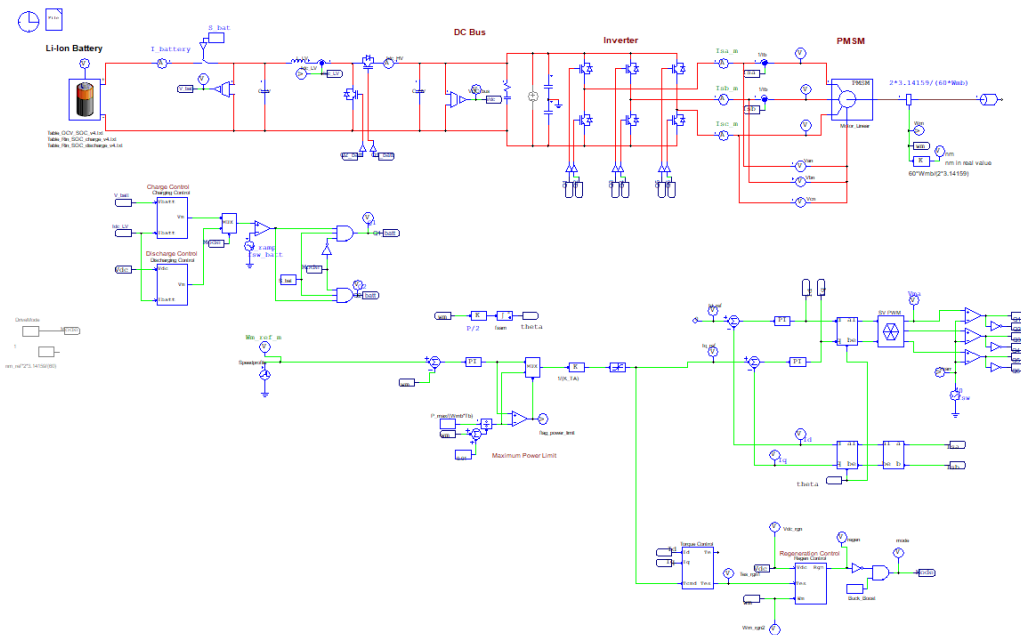
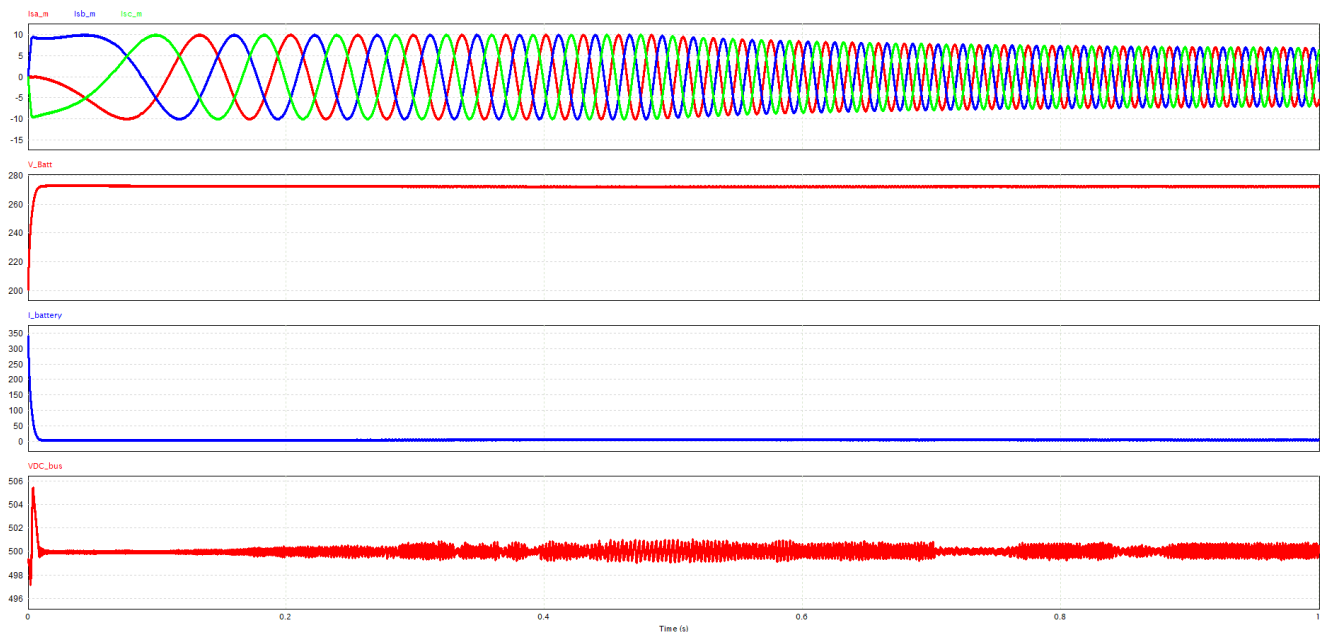
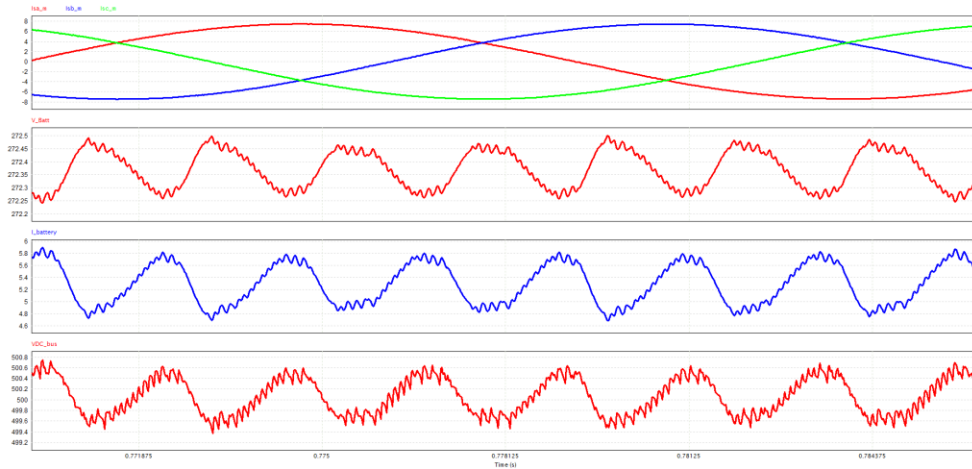


Fig. 4.35: Complete setup for the Hyperloop LSM propulsion system (based on PMSM)

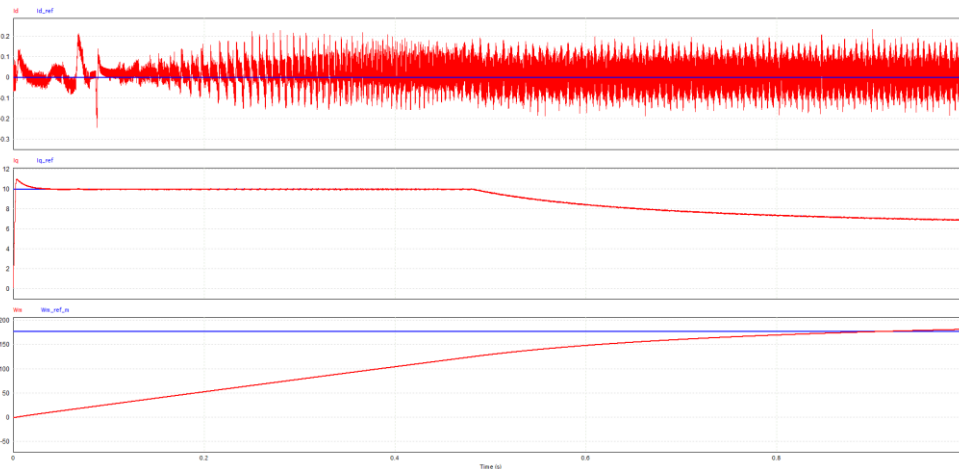
Looking at the initial results shown in Fig. 4.36a, the three phase AC currents, at starting, is 10 amps peak to peak which then settles down to around 7 amps peak to peak. The battery voltage and current are as expected. The average battery voltage at 80% SOC is 272 V and the average battery current drawn is 6.7 A. The boosted DC voltage seem sporadic which may need further investigations. However, the average voltage is as expected of 500 V with a small ripple as shown in Fig. 4.36b. The control signals and their references can be compared and studied in Fig. 4.36c. The  $I_d$  was set to 0, the measured signal oscillates with an average of 22 mA. The  $I_q$  follows the reference well and achieves steady state before  $t = 0.2$  s. Finally, the speed ramps up to the set reference by  $t = 0.9$  s. The simulation triggered the power limiter which means some parametrization may be under specified.



(a)



(b)



(c)

Fig. 4.36: (a) Complete simulation results and (b) Steady state results – three phase currents, battery voltage, battery current, DC bus voltage after boost (c)  $I_d$ ,  $I_q$  and speed command compared to reference

To test the motoring and generating mode of operations, first the motor speed profile is set to run with a constant speed. The waveform in Fig. 4.37 shows that the machine is in motoring mode of operation and through the SOC waveform, the battery can be seen discharging at the expected rate. Then, to show the regenerative braking, the reference speed profile is adjusted to drop in speed at a certain instant and then back to the nominal reference. Fig. 4.38 shows the regenerative braking mode of operation.

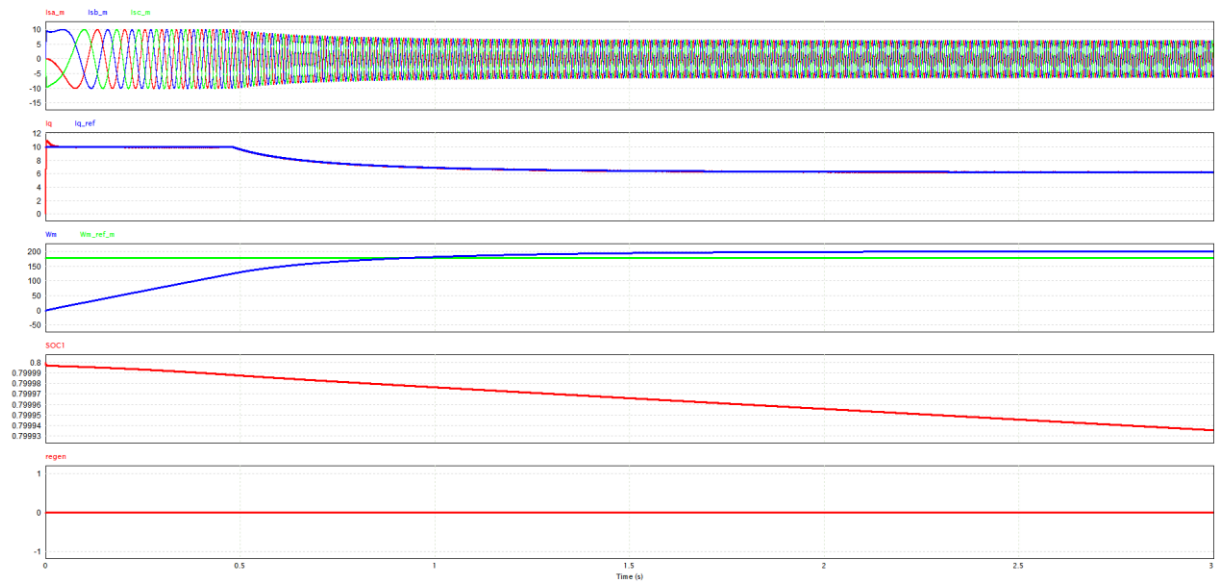


Fig. 4.37: Motoring mode operation results

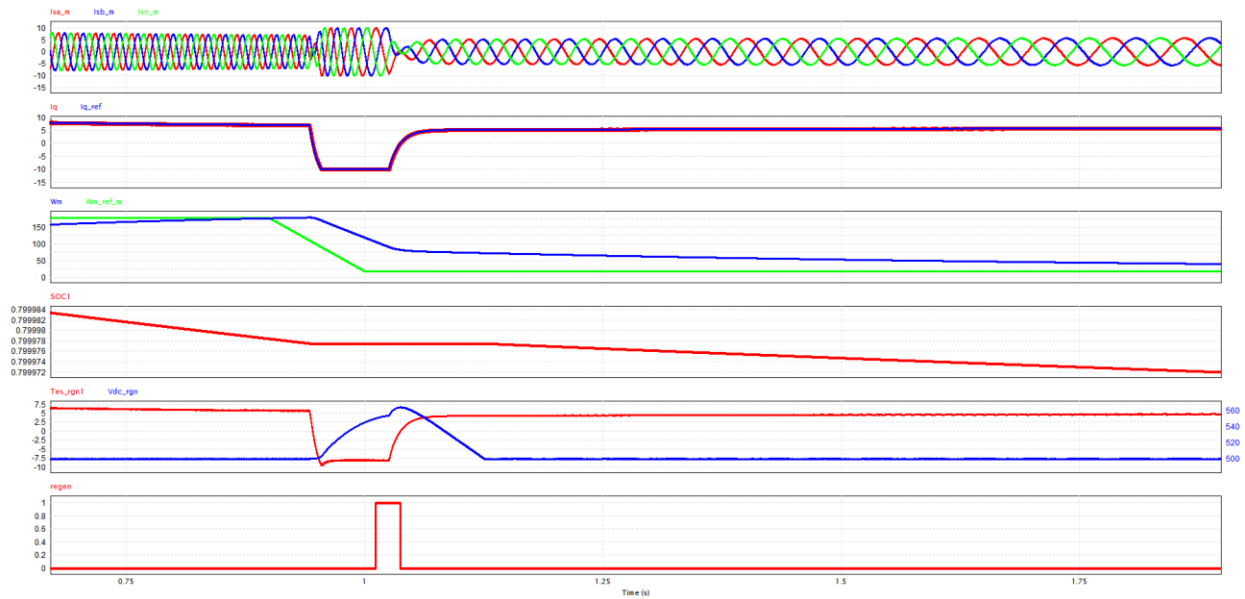


Fig. 4.38: Regenerative braking operation results

## 4.5 Simulations with LSM

The previous simulations were all done with a rotary motor which is good for measuring performance and load capabilities of the overall integrated system. However, for the Hyperloop an important factor is the speed. Thus, Simulink was used to verify the design in this subchapter. The setup for this system is shown in Fig. 4.39 which was provided in the Simulink libraries.

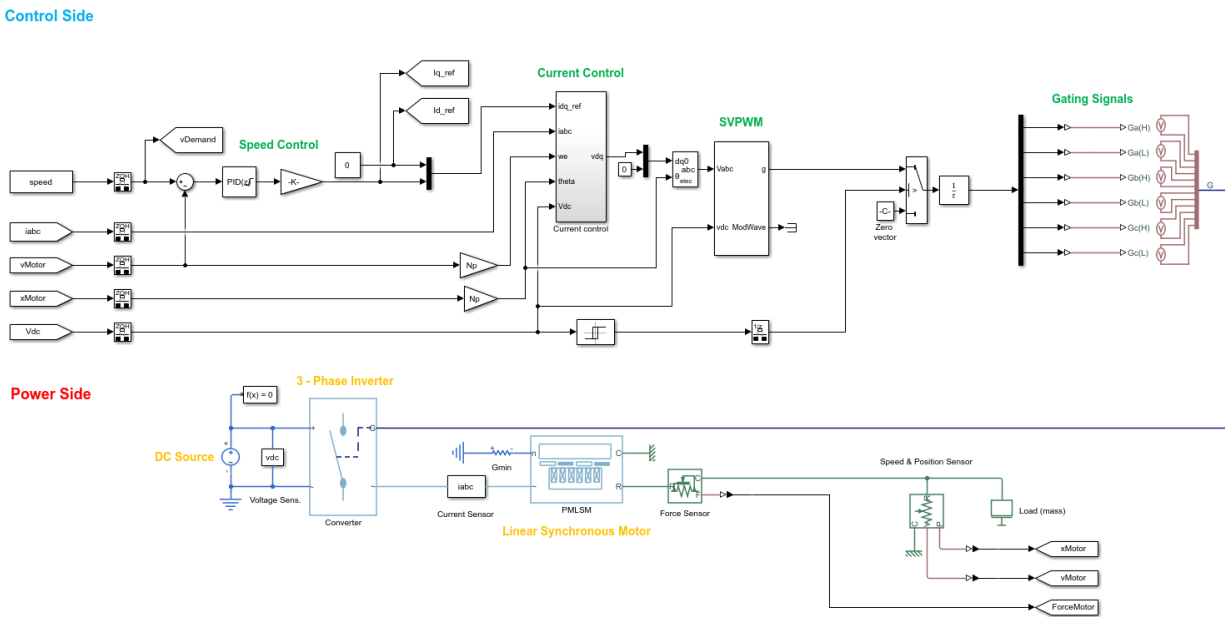


Fig. 4.39: Modelling of the Hyperloop propulsion system in Simulink

The position, speed, three phase currents and thrust curves are provided in Fig. 4.40. To achieve the speed of 280 m/s (1008 km/h) some parameters needed to be adjusted such as the power provided to the motor, the pole pitch, and the permanent flux linkage.

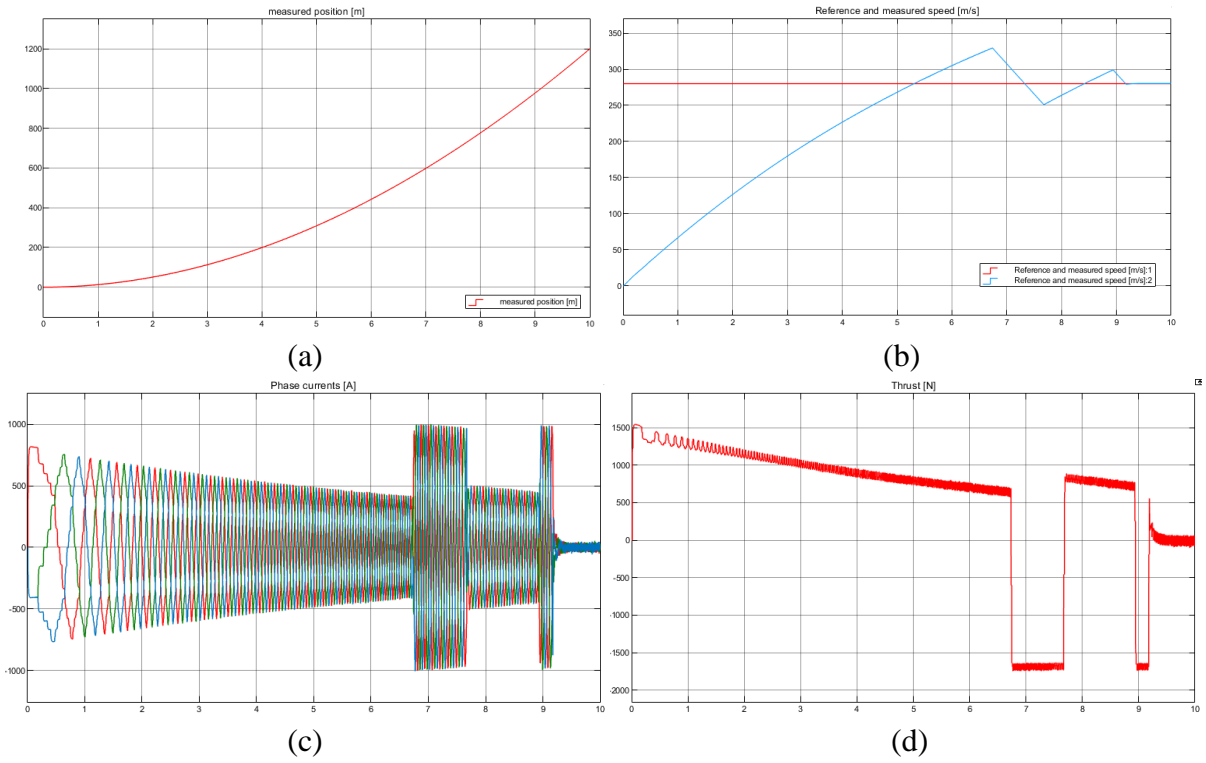


Fig. 4.40: Simulation results from Simulink Model showing (a) measured position over time, (b) speed reference, (c) phase currents, and the resulting (d) thrust curves



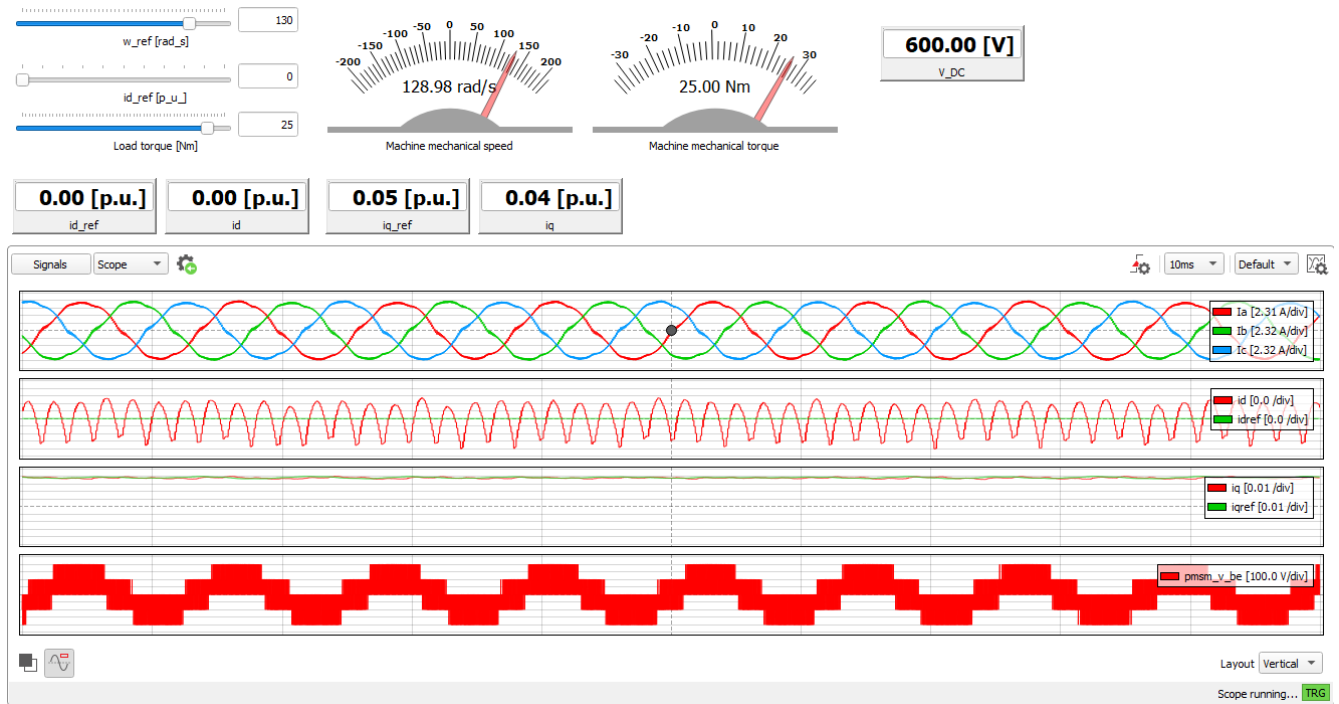


Fig. 5.2: Typhoon HIL offline simulation panel

## 5.2 Online Hardware in the Loop Experimental Setup and Results

The online hardware in the loop setup requires the use of a DSP with the control algorithm (imported from PSIM) and the Typhoon HIL box. Before uploading the controller algorithm from PSIM, the design needs to be slightly adjusted for digital control. Thus, new digital blocks are appropriately used. The delay blocks are used to simulate the update cycles of a real microcontroller/DSP. Moreover, in a real system the sensors would sample it in discrete values, thus the discretization is simulated using zero-order hold blocks. Fig. 5.3 shows the PSIM controller setup for digital control. Fortunately, the impact of the digital delay was minimal and the original PI values were used. This means the phase margin stayed relatively the same.

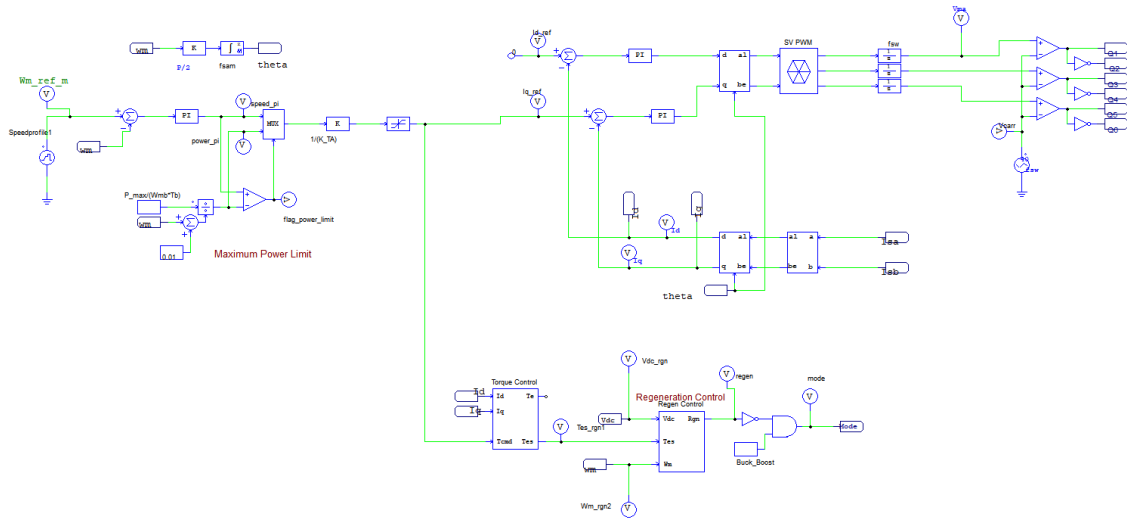


Fig. 5.3: PSIM controller update to account for digital delay

Fig. 5.4 shows the updated schematic to generate the C – code for the Texas Instrument DSP. Some new blocks were introduced to facilitate the integration of the DSP and Typhoon HIL. This includes the TI analog to digital converter block and the 3 – phase DSP PWM generator block.

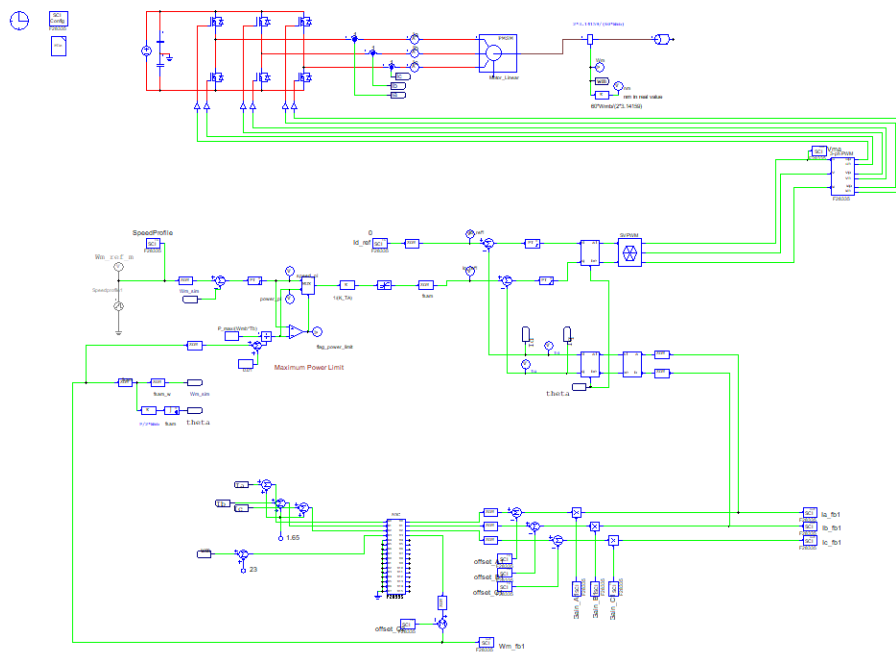
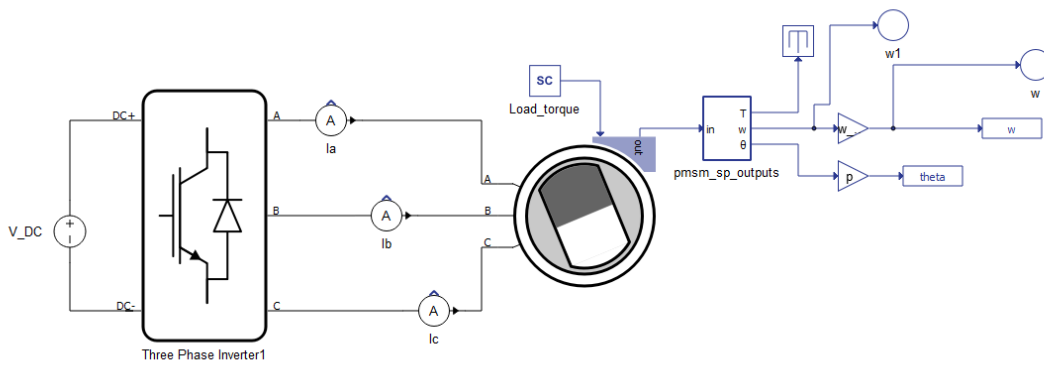


Fig. 5.4: PSIM schematic for TI DSP

After generating the embedded code for the DSP, code composure studio was used to upload it into the TI card. Once the DSP was turned on, the PWM signal generated in no load conditions was seen on the oscilloscope. Next the Typhoon HIL model was loaded, the real time simulation setup is provided in Fig. 5.5. This model in Typhoon does not use any of the input control elements and only contains the power and signal outputs from the motor. The modulation was mapped internally to the appropriate pins from the DSP.



(a)



(b)

Fig. 5.5: Typhoon HIL – real time simulation (a) schematic and (b) SCADA setup

The real time setup for hardware testing of the DSP is provided in Fig. 5.6. The setup includes the PC debugging the CCS and Typhoon HIL code, Typhoon 402 HIL box, TI F28335 DSP. The scope on the left shows the PWM signals from the DSP, and the scope on the right shows the three – phase currents.

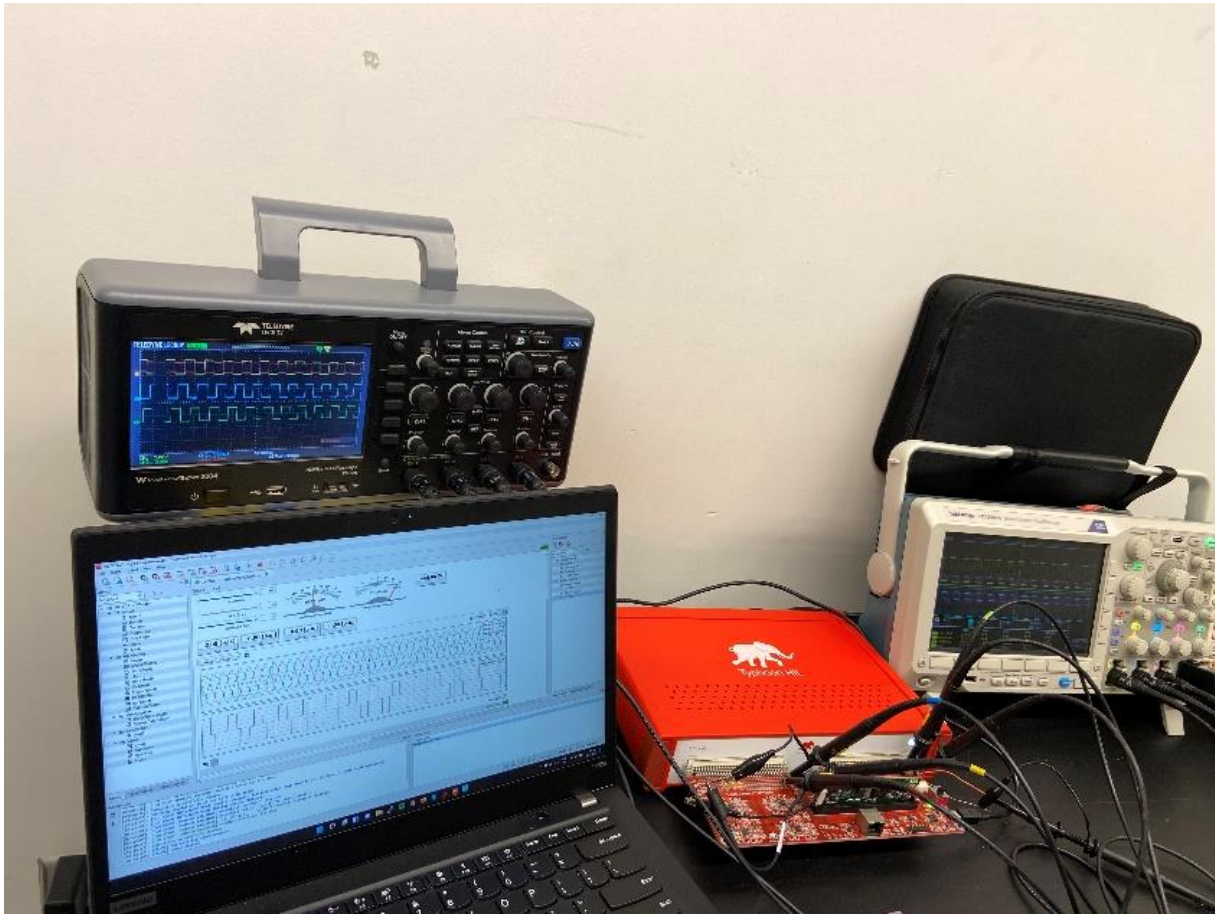


Fig. 5.6: Hardware in the loop setup

The following figures show the resulting oscilloscope waveforms from HIL simulations. Figure 5.7 illustrates pulse width modulating signals generated by the TI DSP control card. The dark blue, red and pink waveforms are the PWM waves for each leg of the inverter. Additionally, one out the three inverting PWM signal is shown in light blue. As expected, the wave is inverted to the first PWM signal with the pre-set duty cycle of 0.5us.

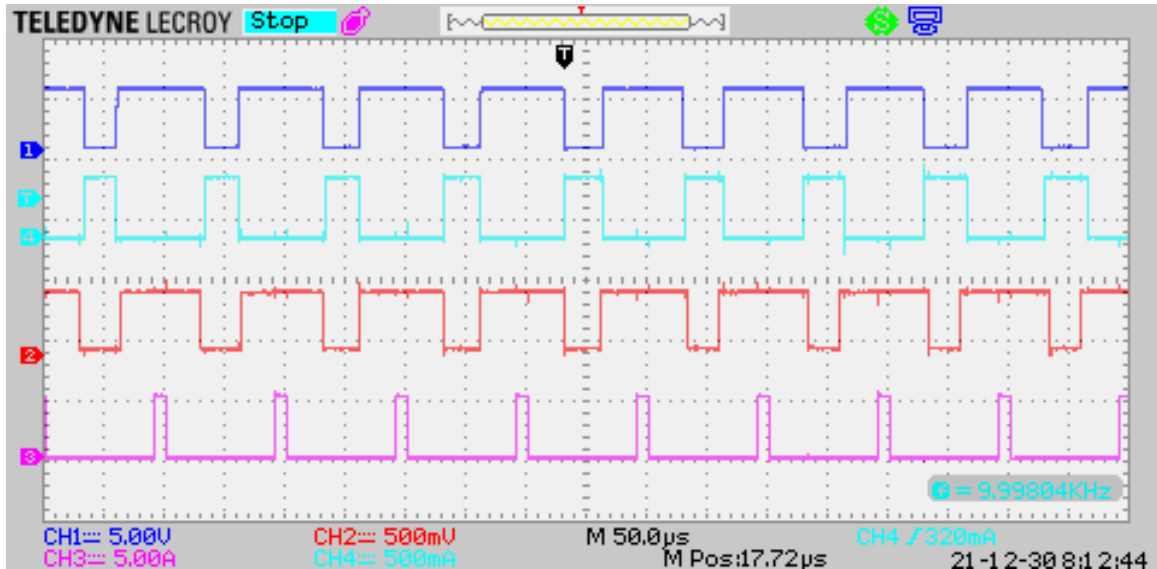


Fig. 5.7: Four pulse width modulation signals generated by TI DSP

The three-phase line to neutral voltage waveforms are provided in Fig. 5.8. This is the analog signal outputted by the HIL 402 box from Typhoon HIL software. The values are scaled down from the digital to analog converter. The three phase currents are shown in Fig. 5.9 and finally another line to neutral voltage for phase a and b is shown in Fig. 5.10.

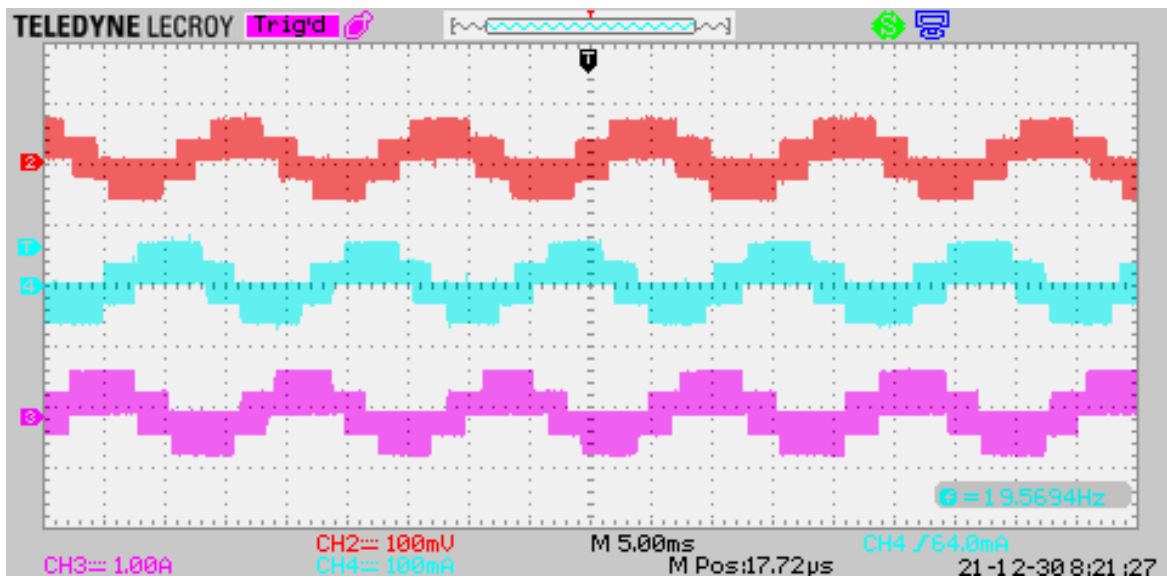


Fig. 5.8: 3-Phase line to neutral voltage waveforms

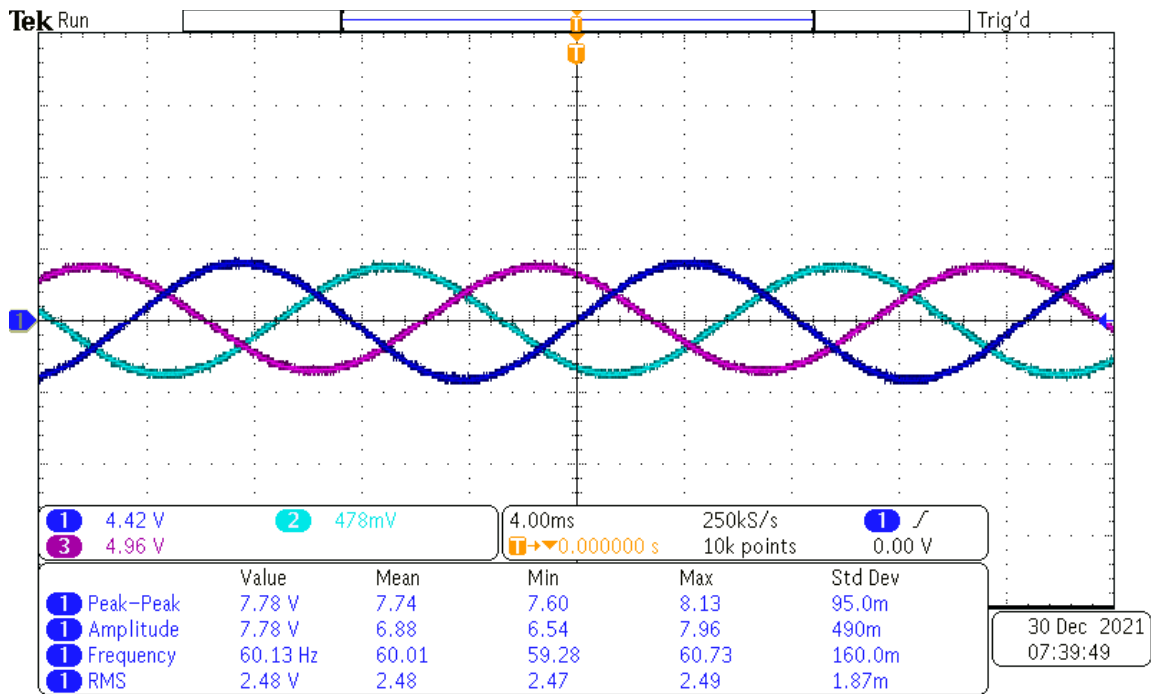


Fig. 5.9: 3 - phase motor currents

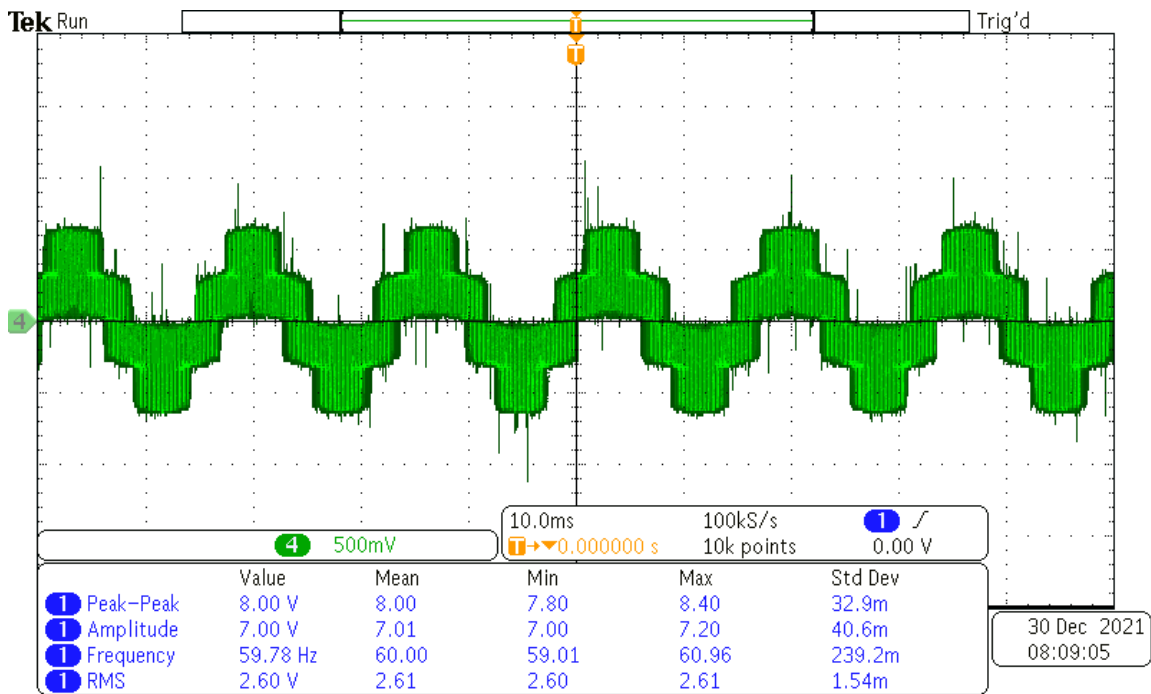


Fig. 5.10: Line to neutral voltage waveform of a single phase

## Chapter 6. Conclusions

Prior to this work there has never been a design study of the Hyperloop. There also has never been a methodology on how to design the system. In the transportation revolution we are living in now, we must have a mathematical background with a sound model that replicates the future perspective. The methodology used in this thesis is similar to designing electric vehicles. Previously, labs would use similar design techniques for cars and simulate it in a real - time hardware in the loop environment. This provided a cost efficient, time conscience design process before taking the big step in building a full prototype of the hardware for the vehicle. Such systems when built will cost billions of dollars. Let alone the cost for building a small-scale lab prototype which requires a large investment costing hundreds of thousands of dollars. Before making any investments and for the interest of time spent on development, it is wise to model, simulate and emulate the system in real time like Typhoon HIL, before considering building a real hardware.

This thesis provides, for the first time, a good step towards the development of such a revolutionary system and provides a cost effective and less time-consuming methodology of judging any futuristic Hyperloop design. In addition, all previous systems reported so far are still in development or never deployed in the market; all of them are Linear Induction Motors (LIM). The thesis provides design based on Linear Synchronous Motor (LSM) which is fast and reliable at high speeds. No one before this thesis provided mathematically a system for a Hyperloop and provided simulation results. Not only does this provide a sound modelling system for the propulsion but goes the extra mile by testing it in another environment. The simulation results from PSIM and Typhoon HIL are in good agreement. This benchmark process was to verify that the effort put into the modelling and design of such system is correct.

In the future, this work can be used for a PhD student or research groups to build a laboratory prototype of the hardware. The study not only provides a sound modelling and design methodology but also provides an accurate real time operation of the system as the HIL platform provides higher resolution for the operation. It was the first time such a system was built in closed loop form, designed in PSIM and verified in Typhoon HIL. A Simulink model was also included to complete the analysis for a high-speed linear motor vehicle.

All in all, this is the first time a design methodology, simulation, and modeling for a Hyperloop propulsion system using linear synchronous motors was demonstrated. Evidence of successful implementation of this design in both PSIM and Typhoon HIL is shown. With the use of the various tools (PSIM & SmartCtrl, Simulink, and Typhoon HIL), a successful steppingstone for a Hyperloop propulsion system was realized. Thus, promoting further development of such a novel transportation system. Lastly, there are several publications all in prestigious IEEE venues like APEC, OJVT, ECCE, IEEE ACCESS, that touches the topic of this thesis. Additionally, a large portion of this work has been published in an invited journal through MDPI. In addition, there are several other IEEE papers & journals regarding this work in review.

## References

- [1] M. A. Bhuiya *et al.*, “Evaluation and Design of a Three-Phase Inverter for a Maglev Application,” *IEEE Conf. Power Electron. Renew. Energy, CPERE 2019*, pp. 418–424, 2019, doi: 10.1109/CPERE45374.2019.8980118.
- [2] L. Alkhaldeh, M. A. Bhuiya, M. Eid, and M. Z. Youssef, “An Enhanced EPP-MPPT Algorithm with Modified Control Technique in Solar-Based Inverter Applications: Analysis and Experimentation,” *IEEE Access*, vol. 9, pp. 8158–8166, 2021, doi: 10.1109/ACCESS.2021.3049517.
- [3] L. Gong, A. Sharma, M. Abdul Bhuiya, H. Awad, and M. Z. Youssef, “An artificial intelligence based fault monitoring of power trains: Design implementation,” *Conf. Proc. - IEEE Appl. Power Electron. Conf. Expo. - APEC*, pp. 2761–2768, 2021, doi: 10.1109/APEC42165.2021.9487452.
- [4] M. Bhuiya, L. Gong, and M. Z. Youssef, “A New Multilevel Inverter Under Distributed Unbalance DC Voltage for Electric Vehicle Applications,” pp. 1521–1526, 2021, doi: 10.1109/ecce47101.2021.9595824.
- [5] A. Sharma, R. Nusrat, M. A. Bhuiya, and M. Z. Youssef, “Hardware-in-the-Loop Validation of Different Power Train Topologies’ Models in Electric Vehicles: A Plug-and-Play Capability,” *IEEE Open J. Veh. Technol.*, vol. 2, pp. 365–376, 2021, doi: 10.1109/ojvt.2021.3110243.
- [6] M. Bhuiya, M. M. Aziz, F. Mursheda, R. Lum, N. Brar, and M. Youssef, “A New Hyperloop Transportation System: Design and Practical Integration,” *Robotics*, vol. 11, no. 1, p. 23, 2022, doi: 10.3390/robotics11010023.
- [7] SpaceX, “Hyperloop Alpha,” 2013. [Online]. Available: [https://www.tesla.com/sites/default/files/blog\\_images/hyperloop-alpha.pdf](https://www.tesla.com/sites/default/files/blog_images/hyperloop-alpha.pdf).
- [8] L. Zhou and Z. Shen, “Progress in high-speed train technology around the world,” *J. Mod. Transp.*, vol. 19, no. 1, pp. 1–6, 2011, doi: 10.1007/bf03325733.
- [9] K. Sato, M. Yoshizawa, and T. Fukushima, “Traction systems using power electronics for Shinkansen High-speed Electric Multiple Units,” *2010 Int. Power Electron. Conf. - ECCE Asia -, IPEC 2010*, pp. 2859–2866, 2010, doi: 10.1109/IPEC.2010.5542320.
- [10] W. Wu, X. Lu, G. Liu, X. Long, Y. Shen, and Y. Liu, “Operation control system of 600 km/h high-speed maglev levitated transport system in China,” *2019 IEEE Veh. Power Propuls. Conf. VPPC 2019 - Proc.*, 2019, doi: 10.1109/VPPC46532.2019.8952570.
- [11] H. W. Lee, K. C. Kim, and J. Lee, “Review of Maglev train technologies,” *IEEE Trans. Magn.*, vol. 42, no. 7, pp. 1917–1925, 2006, doi: 10.1109/TMAG.2006.875842.
- [12] E. Riches, “Will maglev lift off?,” *IEE Rev.*, vol. 34, no. 11, pp. 427–430, 1988, doi: 10.1049/ir:19880177.
- [13] J. Lim, J. H. Jeong, C. H. Kim, C. W. Ha, and D. Y. Park, “Analysis and Experimental Evaluation of Normal Force of Linear Induction Motor for Maglev Vehicle,” *IEEE Trans. Magn.*, vol. 53, no. 11, 2017, doi: 10.1109/TMAG.2017.2699694.

- [14] B. Kowal, R. Ranosz, M. Klodawski, R. Jachimowski, and J. Piechna, "Demand for passenger capsules for Hyperloop High-Speed Transportation System -case study from Poland," *IEEE Trans. Transp. Electrification*, 2021, doi: 10.1109/TTE.2021.3120536.
- [15] A. Tbaileh *et al.*, "Modeling and impact of hyperloop technology on the electricity grid," *IEEE Trans. Power Syst.*, vol. 36, no. 5, pp. 3938–3947, 2021, doi: 10.1109/TPWRS.2021.3056298.
- [16] J. H. Jeong, J. Lim, C. W. Ha, C. H. Kim, and J. Y. Choi, "Thrust and efficiency analysis of linear induction motors for semi-high-speed Maglev trains using 2D finite element models," *IEEE CEFC 2016 - 17th Bienn. Conf. Electromagn. F. Comput.*, 2017, doi: 10.1109/CEFC.2016.7816093.
- [17] S. Jacobs, J. Rens, E. Di Silvestro, and G. Sellitto, "Electromagnetic aspects of the structural integration of linear synchronous machines for a hyperloop technology," pp. 1–6, 2021, doi: 10.1109/Idia49489.2021.9505748.
- [18] C. Y. Lee *et al.*, "Conceptual design of superconducting linear synchronous motor for 600-km/h wheel-type railway," *IEEE Trans. Appl. Supercond.*, vol. 24, no. 3, 2014, doi: 10.1109/TASC.2013.2284662.
- [19] H. Wang, J. Li, R. Qu, J. Lai, H. Huang, and H. Liu, "Study on High Efficiency Permanent Magnet Linear Synchronous Motor for Maglev," *IEEE Trans. Appl. Supercond.*, vol. 28, no. 3, 2018, doi: 10.1109/TASC.2018.2796560.
- [20] R. J. K. Masada and E. Masada, "Comparison of Linear Synchronous and Induction Motors," 2004, [Online]. Available: <https://www.codot.gov/programs/research/pdfs/2004/inductionmotors.pdf>.
- [21] I. Boldea and L. Tutelea, *Electric Machines. Steady State, Transients and Design with MATLAB*. 2010.
- [22] S. J. Chapman, *Electric Machinery and Power System Fundamentals*. 2001.
- [23] P. Krause, O. Wasynczuk, S. Sudhoff, and S. Pekarek, *Analysis of Electric Machinery and Drive Systems*. 2013.
- [24] B. Wu and N. Mehdi, *High-Power Converters and AC Drives*. 2017.
- [25] A. R. Sadat, H. Shadabi, M. Sabahi, and M. B. B. Sharifian, "Tracking of X-Y direction positions with using permanent magnet linear synchronous motors," *22nd Iran. Conf. Electr. Eng. ICEE 2014*, pp. 527–532, 2014, doi: 10.1109/IranianCEE.2014.6999600.
- [26] K. Wang, Q. Ge, L. Shi, Y. Li, and Z. Zhang, "Development of ironless Halbach permanent magnet linear synchronous motor for traction of a novel maglev vehicle," *LDIA 2017 - 11th Int. Symp. Linear Drives Ind. Appl.*, 2017, doi: 10.23919/LDIA.2017.8097238.
- [27] P. Sun, Q. Ge, B. Zhang, and Z. Gao, "An Improved Sensorless Control Method for Long Stator Linear Synchronous Motor," *2019 22nd Int. Conf. Electr. Mach. Syst. ICEMS 2019*, 2019, doi: 10.1109/ICEMS.2019.8922404.

- [28] J. Jin, H. Zhao, Y. Xin, and Y. Sun, "Simulation and analysis of a PMLSM control system based on SVPWM," *Proc. 29th Chinese Control Conf. CCC'10*, pp. 3316–3320, 2010.
- [29] D. Chen, Y. Huang, S. Chen, and S. Lu, "A simulation model of PMLSM based on physical platform," *Proc. 33rd Chinese Control Conf. CCC 2014*, pp. 6555–6559, 2014, doi: 10.1109/ChiCC.2014.6896074.
- [30] L. Xu, R. Wei, Q. Ge, X. Wang, and Y. Li, "Hardware-in-loop simulation of linear synchronous motor based on three-level converter," *2013 Int. Conf. Electr. Mach. Syst. ICEMS 2013*, pp. 1944–1947, 2013, doi: 10.1109/ICEMS.2013.6713218.
- [31] I. Batarseh and A. Harb, *Power Electronics: Circuit analysis and design*. 2017.
- [32] B. M. Wilamowski and J. D. Irwin, *The Industrial Electronics Handbook: Power Electronics and Motor Drives*. 2011.
- [33] M. Ahmad, "High performance AC drives: Modelling analysis and control," *Power Syst.*, vol. 30, 2010, doi: 10.1007/978-3-642-13150-9.
- [34] N. Muhammad H. Rashid Kumar and A. R. (Ashish R. Kulkarni, "Power electronics : devices, circuits and applications," p. 1022, 2014.
- [35] E. C. Dos Santos and E. R. Cabral da Silva, "Advanced Power Electronics Converters," *Adv. Power Electron. Convert.*, 2014, doi: 10.1002/9781118886953.
- [36] P. Cai, X. Fang, Z. Yang, and F. Lin, "Research on multiple topology and modulation strategy of large capacity traction inverter for high speed maglev train," *2019 22nd Int. Conf. Electr. Mach. Syst. ICEMS 2019*, 2019, doi: 10.1109/ICEMS.2019.8921990.
- [37] Texas Instruments, "Field Orientated Control of 3-Phase AC-Motors."
- [38] Texas Instruments, "Field Orientated Control of 3-Phase," 1998.
- [39] C. You, R. Zhang, X. Wang, Y. Du, and Q. Ge, "Vector control of maglev PMLSM based on minimum loss SVPWM method," *19th Int. Conf. Electr. Mach. Syst. ICEMS 2016*, 2017.
- [40] W. Zhao, S. Jiao, Q. Chen, D. Xu, and J. Ji, "Sensorless control of a linear permanent-magnet motor based on an improved disturbance observer," *IEEE Trans. Ind. Electron.*, vol. 65, no. 12, pp. 9291–9300, 2018, doi: 10.1109/TIE.2018.2823660.
- [41] V. Utkin, J. Guldner, and J. Shi, *Sliding Mode Control in Electro-Mechanical Systems*. 2009.
- [42] I. Boldea, *Linear electric machines, drives, and maglevs handbook*. 2017.
- [43] H. Lu, J. Wu, and M. Li, "A new sliding mode observer for the sensorless control of a PMLSM," *Proc. 29th Chinese Control Decis. Conf. CCDC 2017*, pp. 5364–5369, 2017, doi: 10.1109/CCDC.2017.7979450.
- [44] B. K. Bose, *Modern Power Electronics and AC Drives*. 2002.
- [45] M. Ahmad, *High performance AC drives: Modelling analysis and control*, vol. 30. 2010.

- [46] Y. X. Wang, F. F. Qin, and Y. B. Kim, "Bidirectional DC-DC converter design and implementation for lithium-ion battery application," *Asia-Pacific Power Energy Eng. Conf. APPEEC*, vol. 2015-March, no. March, 2014, doi: 10.1109/APPEEC.2014.7066140.
- [47] J. S. Lai and D. J. Nelson, "Energy management power converters in hybrid electric and fuel cell vehicles," *Proc. IEEE*, vol. 95, no. 4, pp. 766–777, 2007, doi: 10.1109/JPROC.2006.890122.
- [48] D. Tudor and M. Paolone, "Optimal Design of the Propulsion System of a Hyperloop Capsule," *IEEE Trans. Transp. Electrification*, vol. 5, no. 4, pp. 1406–1418, 2019, doi: 10.1109/TTE.2019.2952075.
- [49] K. Algarny, A. S. Abdelrahman, and M. Youssef, "A novel platform for power train model of electric cars with experimental validation using real-time hardware in-the-loop (HIL): A case study of GM Chevrolet Volt 2nd generation," *Conf. Proc. - IEEE Appl. Power Electron. Conf. Expo. - APEC*, vol. 2018-March, pp. 3510–3516, 2018, doi: 10.1109/APEC.2018.8341610.
- [50] J. F. Gieras, Z. J. B. Piech, and Tomczuk, *Linear Synchronous Motors: Transportation and Automation Systems*. Boca Raton: CRC Press, 2011.
- [51] PSIM, "HEV Design Suite," 2016. [https://psim.powersimtech.com/hubfs/PDF/Tutorials/Control Loop Design/Tutorial-HEV-Design-Suite.pdf](https://psim.powersimtech.com/hubfs/PDF/Tutorials/Control%20Loop%20Design/Tutorial-HEV-Design-Suite.pdf).
- [52] V. A. Marcis, A. Kelkar, and S. S. Williamson, "Electrical Circuit Modeling of a 18650 Lithium-Ion Cell for Charging Protocol Testing for Transportation Electrification Applications," pp. 169–174, 2020, doi: 10.1109/itec48692.2020.9161522.
- [53] G. L. Plett, *Battery Management Systems: Battery Modeling*, vol. 1. Massachusetts: Artech House Publishers, 2015.
- [54] PSIM, "Lithium-Ion Battery Model," 2016. [Online]. Available: <https://powersimtech.com/support/resources/tutorials/lithium-ion-battery-tutorial/>.
- [55] PSIM, *How to Implement Field Oriented Control of PMSM with PSIM & SmartCtrl*. 2014.
- [56] IEEE Standards Association, *IEEE Recommended Practice for the Design and Application of Power Electronics in Electrical Power Systems*. 2016.